The Effect of High Voltage Electric Fields on Two Phase Flow Pattern Redistribution & Heat Exchanger Performance

The Effect of High Voltage Electric Fields on Two Phase Flow Pattern Redistribution & Heat Exchanger Performance

By

Sarah Nangle-Smith B.A., B.A.I.

A Thesis

Submitted to the School of Graduate Studies

in Partial Fulfilment of the requirements

for the Degree

Masters of Applied Science

McMaster University

Hamilton, Ontario, Canada

MASTERS OF APPLIED SCIENCE (2012) McMASTER UNIVERSITY
(Mechanical Engineering) Hamilton, Ontario, Canada

TITLE	The Effect of High Voltage Electric Fields on Two Phase Flow Pattern Redistribution & Heat Exchanger Performance
AUTHOR	Sarah Nangle-Smith
SUPERVISOR	Dr. J.S. Cotton
NUMBER OF PAGES	xiv, 138

Abstract

A short, 30cm, test section was used to study the effect of electrohydrodynamic (EHD) forces on flow redistribution in a horizontal, shell and tube heat exchanger subject to both boiling and condensation. The use of a short test section allows for a consistent flow pattern across the test section length which provides further insight into the true effect of EHD.

It was found that the voltage polarity of the applied voltages influences the flow distribution. For the current geometry studied, it was found that positive polarity voltages tend to pull liquid away from heat transfer surface and that negative voltages tended to repel more liquid toward the heat transfer surface. Using this knowledge we were able to show that positive voltages were more effective for convective condensation heat transfer enhancement, whereas negative voltages were more effective for convective boiling heat transfer enhancement. A twofold enhancement of convective boiling heat transfer was achieved for positive voltages and a 4fold enhancement was achieved for negative voltages. Similar pressure drop penalties were seen for both cases, approximately twice that of the no EHD case.

Furthermore, the effect of DC level, peak to peak voltage, frequency and duty cycle waveform parameters on convective boiling enhancement were studied to explore the range of controllability for the current set of flow parameters. It was found that these various waveform parameters can induce different flow patterns and consequently different heat transfer and pressure drop configurations. In general the heat transfer is enhanced by EHD, but different pressure drop penalties can be achieved for a given enhancement ratio using different waveforms. High heat transfer for relatively low pressure drop was achieved using either negative DC signals or 50%duty cycle pulse waveforms. In some cases the enhancement is quite little compared to the pressure drop, for example the zero DC level, varying peak to peak voltage data. It is suggested that in a system where the heat exchanger pressure drop due to EHD is more dominant than the system pressure drop, it may be possible to use EHD as a method of retarding the system rather than enhancing it thereby broadening the scope of controllability.

Finally we showed the proof of concept of using DC EHD as a rapid control mechanism for the load conditions. Using -8kVDC the water side heat flux could be varied by approximately ±3.2 kW/m^2 within 5 seconds. As a comparison, the same experiment was repeated using the refrigerant flow rate to control the load. Response times were similar for both experiments and although the power required for the flow rate control was less, the minimal variability in flow parameters for the EHD control make it a more attractive method of load control.

Acknowledgement

First I would like to express my sincerest gratitude to Dr. Jim Cotton for his exceptional guidance, support and expertise throughout this thesis. It was a pleasure to work with you and I hope the next four years will be as successful as these past two. In addition I would like to thank Dr. Ching for his guidance and daily motivation and Dr. Hossam Sadek for his expertise and invaluable help throughout my studies.

I would like to extend my thanks to the mechanical engineering technicians; Ron Lodewyks, Joe Verhaeghe, J.P. Talon, Mark MacKenzie, Jim McLaren and Michael Lee and to the mechanical engineering staff; Vania Loyzer, Lily Sazz-Fayter and Florence Rosato for their help. I would also like to thank McMaster University and NSERC for funding this thesis and providing financial support.

I would like to give a special thank you to Dr. Tony Robinson and Dónal without whom I probably wouldn't have had the opportunity to undertake this project. I would also like to thank Kevin Ng for his help in getting started on this project and the rest of the members of TMRL for their friendship, support, guidance and sometimes well needed distraction.

Finally I would like to thank my family and friends for their continued encouragement and support throughout this thesis, to Barry for linking me up to the Irish 6 Nations games and especially to my gran for her determination to learn how to use Skype and her endless supply of tea.

Table of Contents

List of Figures

List of Tables

Nomenclature

Symbol			
A	Flow Area [m^2]	$\dot{m}$	Mass flow rate
Cp	Specific Heat [kJ/kg.K]	Md	Masuda number
D	Diameter [m]	Nu	Nusselt Number
E	Electric Field Strength [V/m]	P	Pressure [Pa]
E_{hd}	EHD number	Pr	Prandtl number
f	Friction factor	q"	Heat Flux [W/m^2K]
f_{eB}	Electric Body Force	r	Radius [m]
Fr	Froude Number	Re	Reynolds number
G	Mass Flux [kg/m^2s]	t	Time [s]
g	Acceleration due to gravity, $9.81m/s^2$	T	Temperature [K]
h	Heat transfer coefficient [W/m^2K]	U	Velocity [m/s]
I	Electric Current	V	Voltage [kV]
j	Current density [A/m^2]	We	Weber Number
j_D	Displacement current density [A/m^2]	x	Flow quality
k	Thermal conductivity [W/m.K]	X	Lockhart-Martinelli Parameter
L	Length	z	Axial distance [m]

Greek Symbol			
α	Void Fraction	ϕ	Two phase multiplier
δ	Uncertainty	ρ	Density [kg/m^3]
ε	Dielectric permittivity [N/V^2]	ρ_c	Space charge density [C/m^3]
ε_o	Dielectric permittivity in free space, $8.85x10^{-12}$ [N/V^2]	θ	Non-dimensional temperature
ε_r	Dielectric constant $\varepsilon/\varepsilon_o$	σ	Surface tension [N/m]
μ	Dynamic viscosity [Pas	Σ_e	Electric conductivity [S/m]
μ_e	Ion mobility [m^2/Vs	τ	Non dimentional time
ν	Kinematic viscosity [m^2s]	T_c	Charge relaxation time [s]

Subscripts			
eff	effective	ref	refrigerant
elec	Electrical preheater	T	temperature
fr	frictional	tp	Two phase
h	Hydraulic	v	vapour
In	Inlet	vo	Vapour only
l	Liquid	water	water
lo	Liquid only	s	Surface
o	reference	sat	Saturated
Out	Outlet	sub	subcooled
pp	Peak to peak		

Chapter 1: Introduction

The enhancement of heat exchangers is an important research that can significantly improve the thermal efficiency of the system which yields an obvious economic benefit. For a specified loading, a heat exchanger can be made more compact if enhancement techniques are used. This is useful for applications where there are space limitations and it also reduces the cost of the system as less material is used. Enhancement techniques are also useful in improving the performance of older heat exchangers that may have a reduced capacity due to fouling and therefore increase the lifecycle of heat exchanger units.

This thesis deals with the use of high voltage electric fields coupled with dielectric fluid heat exchangers, a phenomenon that promotes bulk mixing within the heat exchanger, enhancing the performance in a controlled way with minimal power requirements. EHD enhancement is particularly useful in two phase dielectric fluid, where there can be an order of magnitude difference in the electric permittivity between the liquid and vapour phase. The EHD induced interfacial force can be large enough to cause significant phase migration and new flow patterns. By knowing which flow patterns are suitable for the mechanism of heat transfer in a specific application, it is possible to use EHD to enhance this mode of heat transfer through phase migration. Typically two phase heat exchangers include boilers, evaporators and condensers and therefore EHD could be potentially used to great effect in organic Rankine cycles

1.1 Heat Exchanger Technology and Convective Boiling Enhancement Techniques

Many different techniques have been developed for the purpose of heat transfer enhancement in heat exchangers. They improve the system thermal efficiency by either reducing the required pumping power or reducing the temperature difference required between the working fluids. The effects of enhancement techniques are varied and as such, they should be compared using Performance Evaluation Criteria, PEC, which considers the thermal-hydraulic performance improvements, economic issues, and manufacturability, reliability and safety issues. (Kakac, et al., 1988)

There are three main types of enhancement techniques: active techniques which require power, passive techniques which do not require any external power source and compound techniques which are a combination of two or more active and passive techniques.

Table 1.1 outlines a number of these active and passive techniques along with a brief explanation of how they work. Equation 1.1 shows an energy balance for a heat exchanger. The total heat transfer is a function of the overall heat transfer coefficient, U, the heat transfer area, A and the log mean temperature difference, ΔT_{lm}, which is an overall temperature difference for the heat exchanger taking account of the difference in temperature of both fluids and how these temperatures vary across the heat exchanger length. See equation 1.3. If the temperature difference between the two fluids is increased, then Q will increase and similarly if the heat exchanger is made very large, i.e. A is increased then Q will also increase. These changes have associated cost, size and efficiency issues. In general, enhancement techniques work by either changing the overall heat transfer coefficient by modifying the flow characteristics or by increasing the heat transfer surface area using modified surfaces rather than larger heat exchangers.

$$Q = UA\Delta T_{lm} \quad \textbf{Eqn. 1.1}$$

$$UA = \frac{1}{R_t} = \frac{1}{\frac{1}{h_i A_i} + \frac{L}{kA} + \frac{1}{h_o A_o}} \quad \textbf{Eqn. 1.2}$$

$$\Delta T_{lm} = \frac{\Delta T_1 - \Delta T_2}{ln(\Delta T_1 / \Delta T_2)} \quad \textbf{Eqn. 1.3}$$

Depending on the mode of heat transfer in a system, different enhancement techniques will have various degrees of success. For example, the most commonly utilised methods for convective boiling and condensation are treated surfaces, extended or rough surfaces, swirl flow devices and electrostatic fields. The design of these enhancement techniques will vary depending on whether they are used to enhance evaporation or condensation.

Table 1.1: Heat Transfer Enhancement Techniques, adapted from (Bergles, 2011)

Active Techniques	Passive Techniques
Mechanical Aids *Mechanical Stirrers and Surface Scraping improves mixing and prevents surface fouling. High associated pressure drop.*	Treated Surfaces *Alteration of the surface finish/coating. Create re-entrant cavities to improve nucleate boiling or superhydrophilic coatings to promote dropwise condensation. Foul-resistant coating. Coatings may decay with time.*
Surface Vibration *Various frequencies applied to heat transfer surface to promote mixing. The best performance is close to the resonant frequency but the amplitude can cause damage to the heat exchanger over time.*	Rough Surfaces *Roughness is small, promotes turbulence rather than increasing surface area. Generally disturbs the viscous sublayer and improves heat transfer.*
Fluid Vibration *Various Frequencies (including ultrasonic) applied to the liquid to enhance bulk mixing. Large mass of fluid generally dampens the vibrations and prevents damaging the system.*	Extended Surfaces *Modified surfaces such as fins to increase the heat transfer area and also modify the flow. Generally used on the side of highest thermal resistance.*
Electrostatic Fields *DC or AC electric fields applied to electrodes in dielectric fluids induces bulk mixing of fluid in the vicinity of the heat transfer surface.*	Displaced Enhancement Devices *Vortex generators, porous metal inserts or orifices are inserted into the flow to promote turbulence.*
Injection *For single phase flows, gas injection causes higher heat transfer rates associated with two phase flow due to increased interfacial effects and mixing. Disturbs boundary layers.*	Swirl Flow Devices *Coiled tubes, inlet vortex generators, twisted tape inserts and axial core inserts with screw type winding cause secondary flows and enhance mixing.*
Suction *Suction can include vapour removal through a porous heated surface to improve boiling characteristics. Disturbs the boundary layer, can promote turbulence.*	Additives for liquids/for gases *Solid, liquid or gas particles/bubbles are introduced to the system and promote turbulence/mixing. Changes the fluid properties and temperatures can be reduced to minimise losses and improve efficiency.*
Jet Impingement *Heated or cooled jets arranged perpendicular or obliquely to the heat transfer surface have been found to produce high heat transfer rates*.	Surface Tension Devices *This includes grooved surfaces and wicking which induce capillary action and can be used to redistribute the flow to different regions to improve heat transfer.*

Structured surfaces have been found to enhance nucleation such that boiling can take place at lower required superheat temperatures. The effect can be seen in Figure 1.1 for different structured surfaces. Looking at the heat flux of approximately 40kW/m^2 we see that all of the structured surfaces lower the required superheat temperature for nucleation to occur by an order of magnitude. Out of the three structured surfaces tested, the 'Union Gorbide High Flux' surface provides the best enhancement. This surface, seen in the middle, has re-entrant type cavities and vapour residue from nucleation bubbles remains trapped in these cavities promoting further nucleation at the site. It can also be seen from the figure that the enhancement achievable using structured surfaces is much more pronounced at lower heat fluxes, i.e. below 200 kW/m^2.

Withers & Habdas, 1974, investigated the effect of helical rib tubes on convective in-tube boiling of R12 and found that the local heat transfer coefficients increased by up to 100%. In addition to this, the dryout heat flux was increased by 200% due to the wetting characteristics caused by the rough surface. This rewetting phenomenon was also responsible for the increase in dryout heat flux in the Swenson et al., 1962, study of widely spaced helical ribbed pipe enhancement in convective boiling. It should be noted that the performance of enhanced surfaces tends to degrade over time as they are subject to fouling build up.

The effect of internal microfin tubes (extended surfaces) on refrigerant convective boiling and condensation has been studied by many researchers (Khanpara & Bergles, 1986), (Kakac, et al., 1988). Microfins are generally two orders of magnitude smaller than the pipe diameters they are used in and the performance increase seen is due to the increase in heat transfer surface area, increased boundary layer turbulence, changes in flow pattern and an increase in the dryout heat flux (Kakac, et al., 1988). The fin profile can be varied and the effect of various fin profiles on R113 convective boiling heat transfer and pressure drop was investigated by Khanpara & Bergles, 1986. These fins and the key results are shown in Figure 1.2. It was found that higher fins with flat valleys and flat peaks are better. Tube 10 had the highest overall heat transfer performance but also the largest pressure drop penalty.

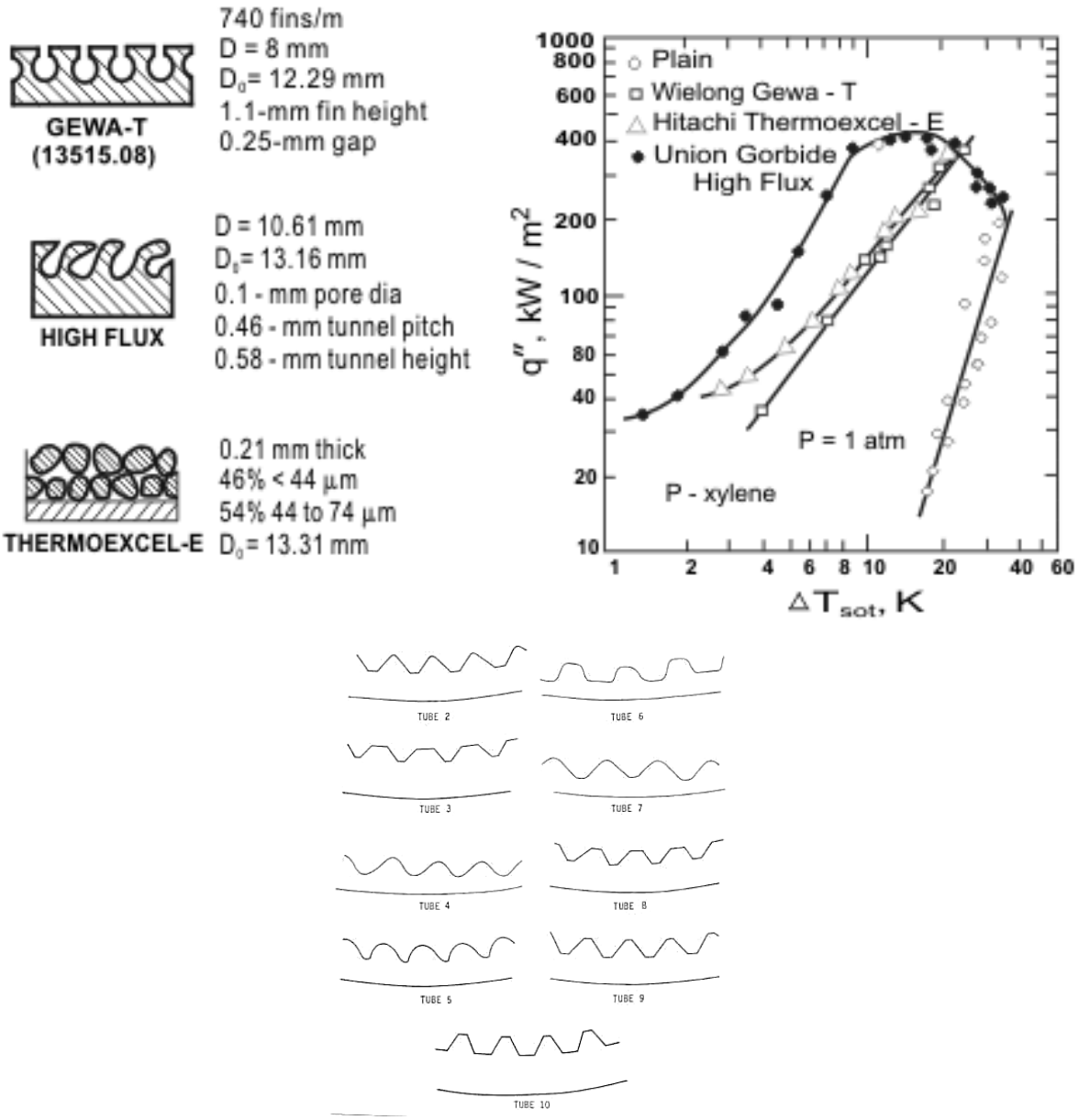

Figure 1.1 : The Effect of Different Structured Surfaces on Convective Boiling (Yilmaz, et al., 1980)

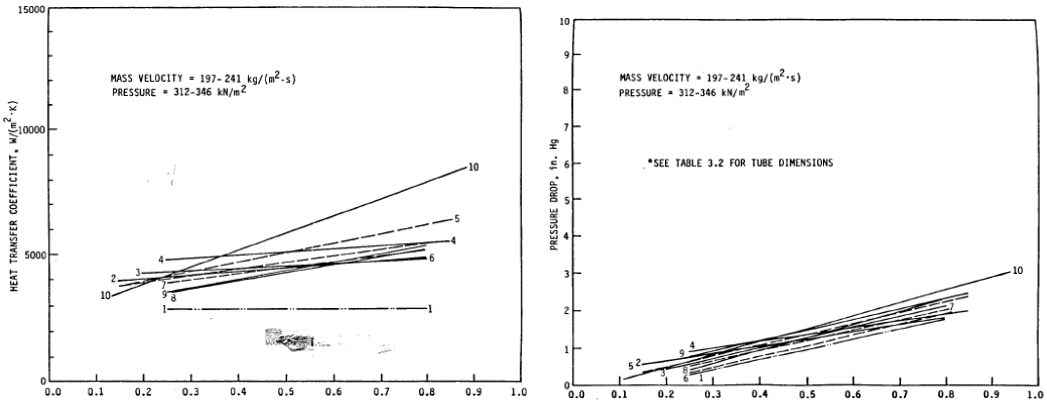

Figure 1.2 : The Effect of Different Microfins on Convective Boiling Heat Transfer Coefficient and Pressure Drop (Khanpara, et al., 1986)

The pressure drop is quite system dependent and lower pressure drop ratios have been quoted for microfin tubes (Kakac, et al., 1988). Khanpara et al., 1986, conducted a convective condensation study with similar microfins as their convective boiling study and found that the enhancement increased by 45%-283% and that the pressure drop increase was less than 100% generally. Thors & Bogart, 1994, (as cited by (Van, 2004)) investigated the effect of plain, microfin and corrugated tubes on the heat transfer and pressure drop of R22 flow boiling. The results are shown in Figure 1.3 and indicate enhancement ratios of up to 200%. Microfin tubes generally induced better heat transfer enhancement than corrugated tubes but they perform similarly at high mass flowrates, however the pressure drop penalty associated with corrugated tubes can be in the range of twice that for microfinned tubes, Figure 1.3.

Heat exchanger performance enhancement using electrostatic fields is the subject of this research and is discussed further in Chapter 3. For EHD convective boiling, the heat transfer enhancement quoted is generally in the 2-3 fold range, with larger enhancement seen locally. Compound enhancement techniques such as EHD and microfins have been found to give even higher enhancement ratios. For example, Allen & Cooper, 1987, reported enhancement of up to 10 fold for EHD enhanced pool boiling of R114 over a horizontal microfin tube and Laohalertdecha et al., 2010, reported that there was a slight increase in enhancement for microfin tubes with EHD compared to smooth tubes with EHD. This study only tested up to 2.5kV DC voltages so it is likely that further increases in enhancement would be found at higher voltages, as long as increasing the voltage doesn't induce breakdown . The reason for the improved enhancement, higher than either EHD or microfinned tubes alone, is most likely due to the increased non-uniformity of the electric field near the heat transfer surface due to the presence of the microfins. A more non uniform electric field will induce more mixing as the liquid phase migrates to the regions of high electric field strength and therefore improve the heat transfer (Cooper, 1992)

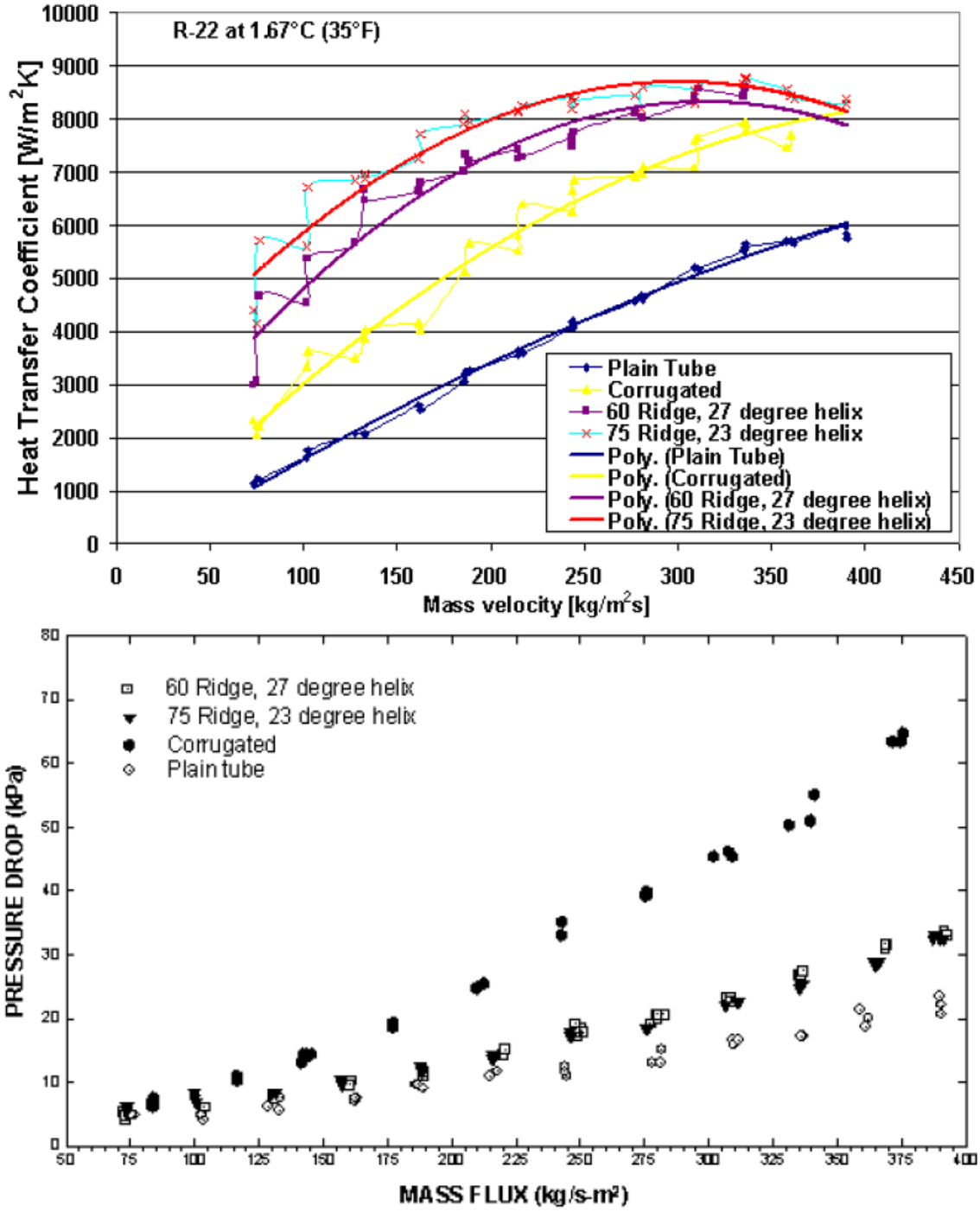

Figure 1.3 : The Effect of Different Microfin and Corrugated Tubes on Convective Boiling Heat Transfer Coefficient (top) and Pressure Drop (Bottom) (Thors et al. 1994)

.

1.2 Control Techniques

The simplest way to control the system performance to meet the load conditions is by varying the flow parameters. Usually the flow rate can be changed via bypass loops or enhancement devices such as throttles, suction and the use of additional or variable speed pumps or compressors. Additionally the inlet or average temperatures of the system can be varied. Both of these techniques change the system performance and can impact the efficiency of the system as most heat exchange systems are designed to operate at an optimum set of parameters. This can be quite important at points such as the inlets to turbine components where the wetness of the steam must be minimal to prevent wear of the blades. Varying the temperature is a slow responding control mechanism which limits its application to slow varying loads.

For rapidly varying dynamic loads and for applications where it is not convenient to modify the flow parameters, it is preferable to attempt to control the heat transfer coefficient inside the heat exchanger. As outlined in the previous section, this can be done using various passive techniques such as additives, roughness or twisted coils but this will just enhance the heat transfer instead of the ability to control it. Active enhancement techniques have the potential to be used to control the heat transfer performance usually by varying the power input e.g. applied voltage in the case of electrostatics fields. EHD is a promising active technique for control purposes for many reasons. The power requirements for EHD are usually less than 1 W as the current required is so low. The range of voltage waveforms that can be applied is only limited by the breakdown voltage which is a function of how the electrodes are designed. Different waveform parameters can be used which have the potential to induce a number of different heat transfer and pressure drop characteristics when coupled with various flow parameters. This means the range of controllability is potentially very large. Further, the application of EHD is instantaneous which offers the possibility of rapid control that can respond to highly varying dynamic load conditions.

Figure 1.4 shows the range of controllability achieved for different applied voltage waveforms on a single pass, horizontal, shell and tube heat exchanger subject to R134a convective condensation and EHD (Sadek, 2009). We see the effect of EHD at low mass flow rates is such that high enhancement is achievable compared to the pressure drop penalty. This drops as the mass flow rate increases for two reasons, a) the pressure drop increases

with increasing flow rate and b) the effect of EHD is best at lower Reynolds numbers as the electric body force has less fluid inertia to overcome. (Cotton, et al., 2005)

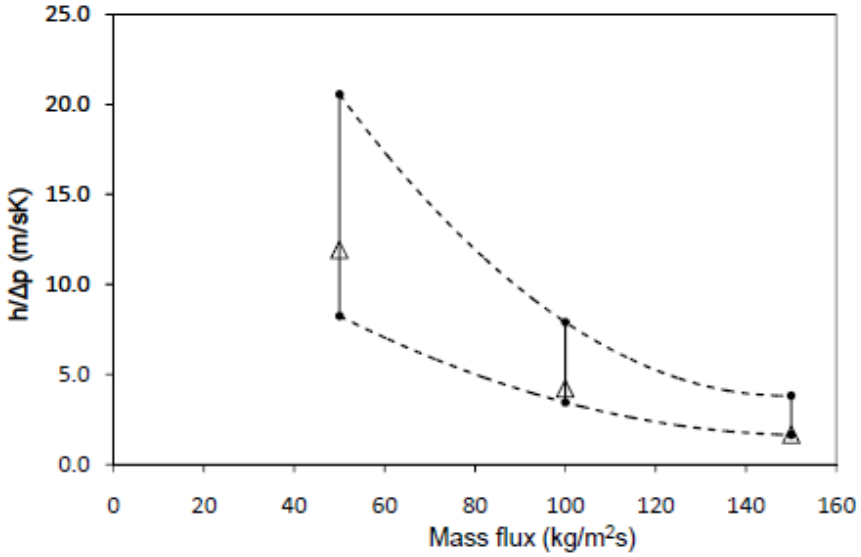

Figure 1.4 : The Effect of Mass Flux on Convective Condensation Heat Transfer to Pressure Drop Ratio at xav = 45% for 8kV DC Applied Voltage Δ and 8kV Pulse Wave Applied Voltage • with Different Pulse Repetition Rates and Duty Cycles. (Sadek, 2009)

1.3 Research Objective

The key objective of this thesis is the use of a relatively short, 30 cm, horizontal annular test section for the purpose of studying the effect of high voltages on flow redistribution and therefore on the heat transfer and pressure drop characteristics in convective R134a flow. The use of the short test section for convective boiling with EHD is novel as it allows for a consistent flow pattern along the axial length of the test section. It is known the two phase heat transfer and pressure drop is dependent on the flow pattern and these parameters are generally used by researchers to analyse the enhancement due to EHD. Despite this, most previous convective boiling EHD studies have not focused on maintaining a consistent flow pattern across the test section (Cooper, 1990), (Norris, et al., 1999) (Cotton, 2000). However some recent convective condensation studies have used short 30cm tubes, (Sadek, 2009) & (Ng, 2010) which provide further insight into the true effects of EHD on heat transfer and pressure drop. For more details on previous EHD studies see Table 2.2.

The effect of voltage polarity on the mechanism of EHD flow pattern redistribution is investigated along with the corresponding effect on both convective condensation and convective boiling heat transfer and pressure drop. Most researchers have not seen any difference between positive and negative two phase flow cases. However, Ng, 2010, saw slight differences in the heat transfer coefficient and the EHD flow patterns induced for the case of convective condensation in a short, 30 cm, test section. This thesis aims to investigate the same effect on convective boiling and to compare both the condensation and boiling cases as this will help us understand the effect of flow pattern redistribution due to EHD better.

Furthermore this study will look into broadening the range controllability by conducting a parametric study of the effect of AC waveform parameters on the flow redistribution in convective boiling. In addition, a proof of concept of the use of EHD load control will be investigated and compared to the same control using varying refrigerant flow rate.

Chapter 2: Electrohydrodynamics and Heat Transfer

In this chapter the relevant aspects electrohydrodynamics as it applied to two phase flow heat transfer are discussed. Basic reviews of two phase heat transfer can be found in (Collier, 1973), (Carey, 1992), and (Faghri & Zhang, 2006).

2.1 Introduction to EHD

Electrohydrodynamics (EHD) is the study of coupled electric and flow fields. EHD arises as an additional body force in the fluid momentum equations and an additional energy source term in the fluid energy equations i.e. it induces fluid motions that can enhance heat transfer processes, the mechanism by which will be explained further in this chapter.

2.1.1 Fundamental Equations

The fluid mechanics equations, assuming a Newtonian fluid, incompressible flow and the Boussinesq assumption, with the additional effects from EHD ($\bar{f}_{eB}$ and q'''_{eB}) are shown below.

Mass conservation

$$\frac{\partial \rho}{\partial t} + \rho \nabla \cdot \bar{u} = 0$$

Momentum conservation

$$\rho \frac{\partial \bar{u}}{\partial t} + \rho(\bar{u} \cdot \nabla)\bar{u} = -\rho F_G - \rho \bar{g}\beta(T - T_0) - \nabla P + \bar{f}_{eB} + \mu \nabla^2 \bar{u}$$

Energy Conservation

$$\rho C_p \frac{\partial T}{\partial t} + \rho C_p \bar{u} \cdot \nabla \mathrm{T} = k \nabla^2 T + q'''_{eB}$$

The magneto-electrohydrodynamic (MEHD) equations were derived by (Chu, 1959).He determined the additional body force terms per unit volume, $\bar{f}_{eB}$ and q'''_{eB}, to be:

$$\overline{\mathrm{f}_{eB}} = \rho_{ei}\overline{\mathrm{E}} + \mathrm{J}_x\overline{\mathrm{B}} - \frac{1}{2}\mathrm{E}^2\nabla\varepsilon - \frac{1}{2}\mathrm{H}^2\nabla\mu + \nabla\left[\frac{1}{2}\rho\mathrm{E}^2\left(\frac{\partial\varepsilon}{\partial\rho}\right)_T + \frac{1}{2}\rho\mathrm{H}^2\left(\frac{\partial\mu}{\partial\rho}\right)_T\right]$$

The terms on the right hand side of equation are, from left to right (Chang & Watson, 1994): the Coulombic/electrophoretic force, the magnetic force due to the charged particle motion, the dielectrophoretic force, the force due to the fluid permeability changes, the electrostriction force and the magnetostriction force.

$$q'''_{eB} = (\bar{J} - \rho_{ei}\bar{u})(\overline{\mathrm{E}} + \bar{u} \times \overline{\mathrm{B}}) + \nabla \cdot [(\overline{\mathrm{E}} + \bar{u} \times \overline{\mathrm{B}}) \times (\overline{\mathrm{H}} - \bar{u} \times \overline{\mathrm{D}})] + \left[\overline{\mathrm{E}}\frac{d}{dt}\left(\frac{\overline{D}}{\rho}\right) + \overline{\mathrm{H}}\frac{d}{dt}\left(\frac{\overline{B}}{\rho}\right)\right]\rho$$

The terms on the right hand side of equations are, from left to right (Chang & Watson, 1994): the heat generation due to flow of charged particles, the energy due to the polarization forces and finally the energy due to the displacement current and time varying magnetic fields.

As there is an electric field in the system, Maxwell's equations also apply to the system.

Maxwell's Equations for time varying fields

Gauss' Law

$$\nabla \cdot \overline{\mathrm{D}} = \rho_{ei}$$

Gauss' Law for Magnetism

$$\nabla \cdot \overline{\mathrm{B}} = 0$$

Maxwell - Faraday Equation

$$\nabla \times \overline{\mathrm{E}} = -\frac{\partial \overline{\mathrm{B}}}{\partial t}$$

Maxwell – Ampere Equation

$$\nabla \times \overline{\mathrm{H}} = \bar{J} + \frac{\partial \overline{\mathrm{D}}}{\partial t}$$

Where

$$\overline{\mathrm{D}} = \varepsilon \overline{\mathrm{E}}$$
$$\overline{\mathrm{B}} = \mu \overline{\mathrm{H}}$$

Finally, the following three equations can aid analysis

Electric Potential

$$\bar{E} = -\nabla V$$

Charge Conservation

$$\nabla \cdot \bar{J} + \frac{\partial \rho_{ei}}{\partial t} = 0$$

Charge Transport Equation

$$\bar{J} = \rho_{ei}\bar{u} - \overline{\mathrm{D}}\overline{\nabla}\rho_{ei} \pm \mu\rho_{ei}\bar{E}$$

Depending on the application i.e. single phase or two phase flow and the electrical and magnetic properties of the fluid(s) and/or phases in the system, some of these equations can be simplified greatly. According to Castellanos, 1998, the terms associated with the magnetic field can be neglected if the ratio of electric energy to magnetic energy is greater than unity. (Sadek, 2009) proved that it could be neglected for the same test rig, EHD parameters and dielectric fluid as used in this research.

Chang & Watson, 1994, also showed the magnetic terms could be neglected for dielectric fluid flow. In addition to this it was suggested that the q'''_{eB} term can be neglected. The largest component of this term is the Ohmic heat generation, $\sigma_e E^2$, and this amounts to 1-2W for our application which is negligible in comparison to the other energy terms in the system.

Taking all of the above into account, the governing equations for a two-phase flow of R-134a in the research is summarized in the Table 2.1.

Table 2.1: Governing Equations

Equation Name	Equation	Eqn. #
Mass Conservation	$\frac{\partial \rho}{\partial t} + \rho \nabla \cdot \bar{u} = 0$	**Eqn. 2. 1**
Momentum Conservation	$\rho \frac{\partial \bar{u}}{\partial t} + \rho(\bar{u} \cdot \nabla)\bar{u} = -\rho F_G - \rho \bar{g} \beta (T - T_0) - \nabla P + \mu \nabla^2 \bar{u} + \left[\rho_{ei} \bar{\mathrm{E}} - \frac{1}{2} \mathrm{E}^2 \nabla \varepsilon + \frac{1}{2} \nabla \rho \mathrm{E}^2 \left(\frac{\partial \varepsilon}{\partial \rho} \right)_T \right]$	**Eqn. 2. 2**
Energy Conservation	$\rho C_p \frac{\partial T}{\partial t} + \rho C_p \bar{u} \cdot \nabla \mathrm{T} = k \nabla^2 T$	**Eqn. 2. 3**
Gauss' Law	$\nabla \cdot \bar{\mathrm{D}} = \rho_{ei}$	**Eqn. 2. 4**
Electric Flux Density Definition	$\bar{\mathrm{D}} = \varepsilon \bar{\mathrm{E}}$	**Eqn. 2. 5**
Maxwell - Faraday Equation	$\nabla \times \bar{\mathrm{E}} = 0$	**Eqn. 2. 6**
Electric Potential Definition	$\bar{E} = -\nabla V$	**Eqn. 2. 7**
Maxwell – Ampere Equation	$0 = \bar{J} + \frac{\partial \bar{\mathrm{D}}}{\partial t}$	**Eqn. 2. 8**
Charge Conservation	$\nabla \cdot \bar{J} + \frac{\partial \rho_{ei}}{\partial t} = 0$	**Eqn. 2. 9**
Charge Transport	$\bar{J} = \rho_{ei} \bar{u} - \bar{\mathrm{D}} \bar{\nabla} \rho_{ei} \pm \mu \rho_{ei} \bar{E}$	**Eqn. 2. 10**

2.1.2 Electric Body Force Term

The electric body force, Equation 2.2, for dielectric two phase flows is composed of three terms.

$$\overline{f_{eB}} = \rho_{ei}\overline{E} - \frac{1}{2}E^2\nabla\varepsilon + \frac{1}{2}\nabla\rho E^2\left(\frac{\partial\varepsilon}{\partial\rho}\right)_T \qquad \textbf{Eqn. 2. 11}$$

The first term is known as the electrophoretic or Coulomb force. This force acts on free ions or charges within the fluid and causes them to migrate along electric field lines. This motion results in a phenomenon known as electroconvection. As a note, electroconvection in gases is also known as corona wind. The Coulomb force is dominant in single phase applications, where there is little change in the permittivity, ε, of the fluid. In two phase applications there will be electroconvection currents in both the liquid and vapour phases due to this force. It can be seen that this force is proportional to the electric field, whereas the other two forces are proportional to the electric field squared. Therefore the effect of polarity manifests in this force and plays a dominant role in single phase applications as a result. In addition, this force is proportional to the volume charge density in the fluid. Equation 2.9 and 2.10 can be used to determine what the charge density in the system is. The system charge density is related to the charge injection from the electrodes, which is discussed in detail in section 2.1.3.

The second and third terms are known collectively as the polarization forces, as they cause polarisation or stretching of the molecules in the dielectric. These forces are dominant in two-phase applications due to the differences in permittivity of the two phase mixture. For liquid-vapor flows, the interfacial force, Equation 2.12, (Stratton, 1941), at the liquid-vapor interface generates a phenomenon known as liquid extraction where the liquid is pulled towards regions of high electric field. The second term is the dielectrophoretic force and the third term is known as the electrostrictive force. The dielectrophoretic force arises due to the spatial change in permittivity. The permittivity can be spatially inhomogeneous due to non-uniform electric fields, changes in phase and temperature gradients in the flow. The electrostrictive term arises due to the change in permittivity with density which can be due to local concentrations (i.e. fluid additives, suspended droplets, boundary layers etc) or temperature gradients in the flow.

Interfacial force (subscripts 1, 2 denote different phases, subscripts n, t denote normal and tangential directions)

$$\mathrm{F}_i^{"} = \frac{\varepsilon_0}{6}\left(\frac{1}{\varepsilon_2^2}[4\varepsilon_1^2\varepsilon_2 - 2\varepsilon_1^2 - 4\varepsilon_1\varepsilon_2^2 + 2\varepsilon_2^2]E_{n,1}^2 + [\varepsilon_2(\varepsilon_2 - 2) - \varepsilon_1(\varepsilon_1 - 2)]E_{t,1}^2\right) \quad \textbf{Eqn. 2. 12}$$

The relative importance of EHD, in comparison with other terms in the momentum equation such as inertial forces and viscous forces can be determined by doing a dimensional analysis of the fluid momentum equation as was completed by Chang & Watson, 1994 and Cotton, 2000. The results are summarised here but the full analysis can be seen in Appendix D. Two important dimensionless EHD numbers result from the dimensionless analysis. These are the EHD number, which is a dimensional form of the Coulomb force, and the Masuda number, which is used in the dimensional form of the polarisation forces (Chang & Watson, 1994).

$$\mathrm{E}_{hd} = \frac{I_o L^3}{\rho_o \nu^2 \mu_e A} \quad \textbf{Eqn. 2. 13}$$

$$\mathrm{M}_d = \frac{E^2 \varepsilon_0 L^2 T_0 (\partial \varepsilon_s / \partial T)}{2\rho_o \nu^2} \quad \textbf{Eqn. 2. 14}$$

The dimensional form of the momentum equation is as follows (Cotton, 2000).

$$\frac{\partial \tilde{u}}{\partial \tau} + \tilde{u} \cdot \nabla \tilde{u} = \frac{Gr}{Re^2}(\theta - 1) - \tilde{\nabla} P + \frac{1}{Re}\tilde{\nabla}^2 \tilde{u} + \frac{\mathrm{E}_{hd}\tilde{\eta} - \mathrm{M}_d \tilde{\eta}^2 \tilde{\nabla}\theta + \mathrm{M}_d \tilde{\nabla}(\theta \tilde{\eta}^2)}{Re^2} \quad \textbf{Eqn. 2. 15}$$

Looking at this equation, using an analogy to free convective flows, it can be said that EHD forces are important if the EHD and Masuda numbers are of the same order of magnitude as the square of the Reynolds number i.e. If $\frac{\mathrm{E}_{hd}}{Re^2} \ll 1$ & $\frac{\mathrm{M}_d}{Re^2} \ll 1$ then EHD effect can be neglected as the inertial effects in the flow are far more dominant. (Cotton, et al., 2005) The key concept that should be taken from this analysis is that EHD is most effective at low mass flux e.g. below 100 kg/m^{2}s.

2.1.3 Charge Injection

Electroconvection in fluids cannot occur unless there are charges present in the fluid. There are two generally accepted models for the source of these charges in dielectrics: the conductivity model and the mobility model. (Martin & Richardson, 1984). The conductivity models assume that the charge distribution arises from the variation of electrical conductivity in the model due to thermal gradients and the mobility model is based on the concept of charge or electron injection from the electrodes. Turnbull, 1968, showed that the

conductivity model worked for a weakly conducting fluid and Fujino & Mori, 1987, showed that the mobility model worked in their studies of refrigerant R113. It is likely then that the refrigerant used in this study, R143a, is likely to conform to the mobility model as it is a dielectric and therefore the conductivity component is minimal. It is likely that it conforms to the Schottky charge injection model as the electric field strengths typical for dielectric applications are below 10^8V/m. This is where injection occurs from the cathode due to a lowering of the potential barrier to charges by high electric fields, (Coelho, 1979), (Kuffel, et al., 2000), (Ng, 2010). More recently Ng, 2010, experimentally investigated the effect of voltage and polarity on the charge injection into R134a flowing in a concentric shell and tube heat exchanger. The heat transfer surface was grounded and there was a concentric electrode to which the high voltage waveforms were applied. His results show that the mobility component of charge injection is dominant and that the mechanism of the charge injection is always negative electrons from the negative electrode.

2.1.4 Breakdown Voltage

The dielectric (refrigerant) behaves as a capacitor; a voltage is applied across the electrodes, the mobility component of the current increases and charges are injected into the fluid. Once a critical charge concentration, known as the dielectric strength, is reached, the dielectric will conduct current and this phenomenon is known as breakdown. Typically to test for this limit, the voltage is increased until arcing occurs and this voltage is then known as the 'breakdown voltage'. However it is worth noting that breakdown is actually dependent on conduction current and therefore, temperature, in addition to phase, void fraction and flow pattern (Fukuma, et al., 2000) so the quoted breakdown voltage may not be the upper limit. The breakdown voltage for R134a is 10 kV/3.9mm, (Cotton, 2000).

2.1.5 Mechanisms of EHD Flow Redistribution

EHD arises in the form of a body force in the momentum equation resulting in fluid motion and therefore flow redistribution. New flow patterns, for example twisted liquid cones, can be generated with the application of high voltage electric fields and therefore new flow pattern maps need to be developed as a predictive design tool.

The type of flow redistribution caused by EHD can be categorised into 5 different types, See Figure 2.1, all of which result in increased mixing in the flow (Chang & Watson, 1994).

Increased mixing of the flow generally results in improved heat transfer but also contributes to additional pressure drop. The key mechanisms of flow pattern transition are:

1. *Bulk convection within each phase*

The Coulomb force induces electroconvection of fluid molecules along electric field lines. This occurs in both the liquid and vapour bulk regions. Small differences in permittivity due to temperature gradients within each phase will also induce some movement due to the electrostrictive component of the EHD body force, (Chang & Watson, 1994).

2. *Liquid Extraction and Interfacial instability*

The polarisation forces induced by the presence of an electric field are strongest at the liquid vapour interface due to the large difference in permittivity in this region and the liquid will be extracted toward the region of high electric field. See Equation 2.12. This increases in the interfacial area and redistributes the flow. (Chang & Watson, 1994)

3. *Formation of liquid jets/columns and droplet entrainment/impingement*

Liquid jet and liquid column structures have been observed in dielectric fluid flow systems subjected to high voltage electric fields (Cotton, et al., 2001), (Sadek, 2009), (Ng, 2010). These flow structures are highly turbulent and unique to EHD. This additional mixing often entrains droplets from the flow into the core region and can also cause droplet impingement on heat transfer surfaces.

4. *Enhanced nucleation effects in evaporation applications*

The polarisation forces induce the liquid to move to regions of high electric field squeezing the vapour bubbles toward regions of low electric field or grounded surfaces. They also cause the bubbles to stretch in the direction of the electric field lines and the vapour bubble base can spread along on the heat transfer surface, increasing the film area and activating new nucleation sites, (Ogata & Yabe, 1993), (Di Bari & Robinson, 2009). In addition, the mixing breaks up the larger slugs into smaller, well mixed bubbles, particularly in the case of AC applied signals which induce oscillation of the vapour bubbles, (McGranaghan, et al., 2012).

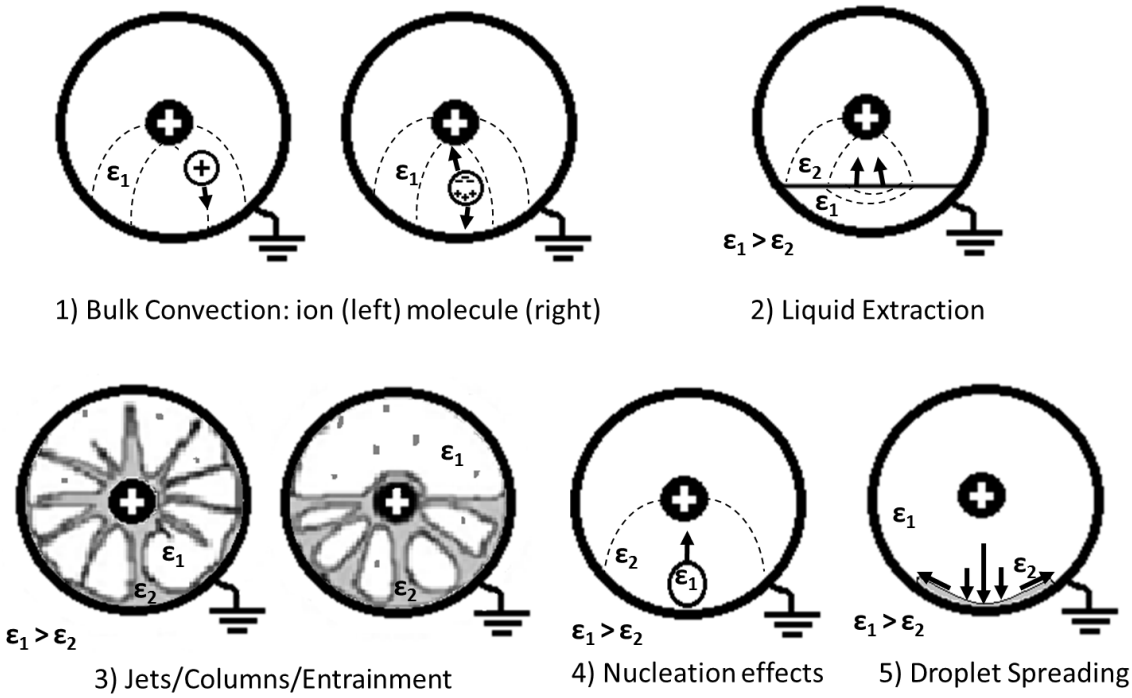

Figure 2.1: Mechanisms of EHD Flow Redistribution for Annular Geometries

5. Liquid Spreading

A liquid spreading phenomenon can occur due to the Coulombic electrical pressure acting on interface of a charged thin liquid film. This effect on silicone oil was analysed by Mahmoudi, 2012 as the classical Stefan's squeeze film flow problem. Their system was in the corona discharge region, i.e. the liquid is charged and the dielectrophoretic term of the electric pressure was neglected. The electric pressure changes the contact angle of the liquid film causing the film to spread and thin. This phenomenon could aid surface rewetting and possibly reactivate nucleation sites, therefore offering the possibility to greatly enhance evaporative heat transfer.

2.2 Two Phase Flow Patterns in Horizontal Channels

The Flow pattern is the distribution of liquid and vapour flow in a system. Flow pattern identification is required for the analysis of two phase flow systems. Each flow pattern has different heat transfer and pressure drop characteristics associated with it and therefore, the prediction of flow pattern is a critical aspect of the design process. The main influences on flow pattern in a system are the system geometry (including objects that disturb the flow), orientation (gravitational effects), temperature dependent fluid properties,

surface tension in particular, the flow rates and the flow quality. In convective boiling applications single phase liquid is pumped to the boiler/evaporator where it is then heated. As the quality increases, different flow regimes will be established and these have different heat transfer mechanisms associated with them.

As shown in Figure 2.2, the first flow regime encountered is bubbly flow. Nucleation begins on the heat transfer surface when the liquid begins to boil and bubbles are formed. Buoyancy forces cause these bubbles to gather on the top surface of the tube. If the applied heat is high enough, it is possible to get subcooled boiling. This mechanism of heat transfer involves nucleation within a bulk fluid that is below the saturation temperature of the liquid. Subcooled boiling is not encountered in this research but details on this subject can be found in reviews (Collier, 1973), (Katto, 1986). After subcooled boiling, saturated boiling is achieved where the bulk fluid is at the saturation temperature and bubbles formed are sustained in the fluid flow. Heat transfer in this region is enhanced due to vigorous mixing caused by bubble movement and consequently many heat transfer appliances are designed to produce the required superheat for this mechanism of heat transfer.

As the flow quality increases, these bubbles start to coalesce into vapour plugs. When the plugs grow large enough to cause partial stratification of the flow, the flow regime is known as slug flow. In this region the flow is mainly stratified with intermittent ‘slugs’ reaching the top surface of the tube. Further along the tube, the quality increases such that the slugs cannot reach the top surface and a stratified-wavy flow pattern can be seen. In general there will be some intermittent wetting of the top surface and so the heat transfer mechanism is forced convective heat transfer through a liquid film on the bottom surface and film conduction evaporation phenomenon through the thinner liquid film on the top surface. If the vapour velocity is relatively high in this region, there can be significant droplet entrainment into the vapour region and if the mass flow rate is high enough an annular type flow regime can be seen, where the liquid level sweeps around the circumference of the tube. If the flow rate is low enough, a stratified flow pattern can be seen where there is minimal waviness on the liquid vapour interface.

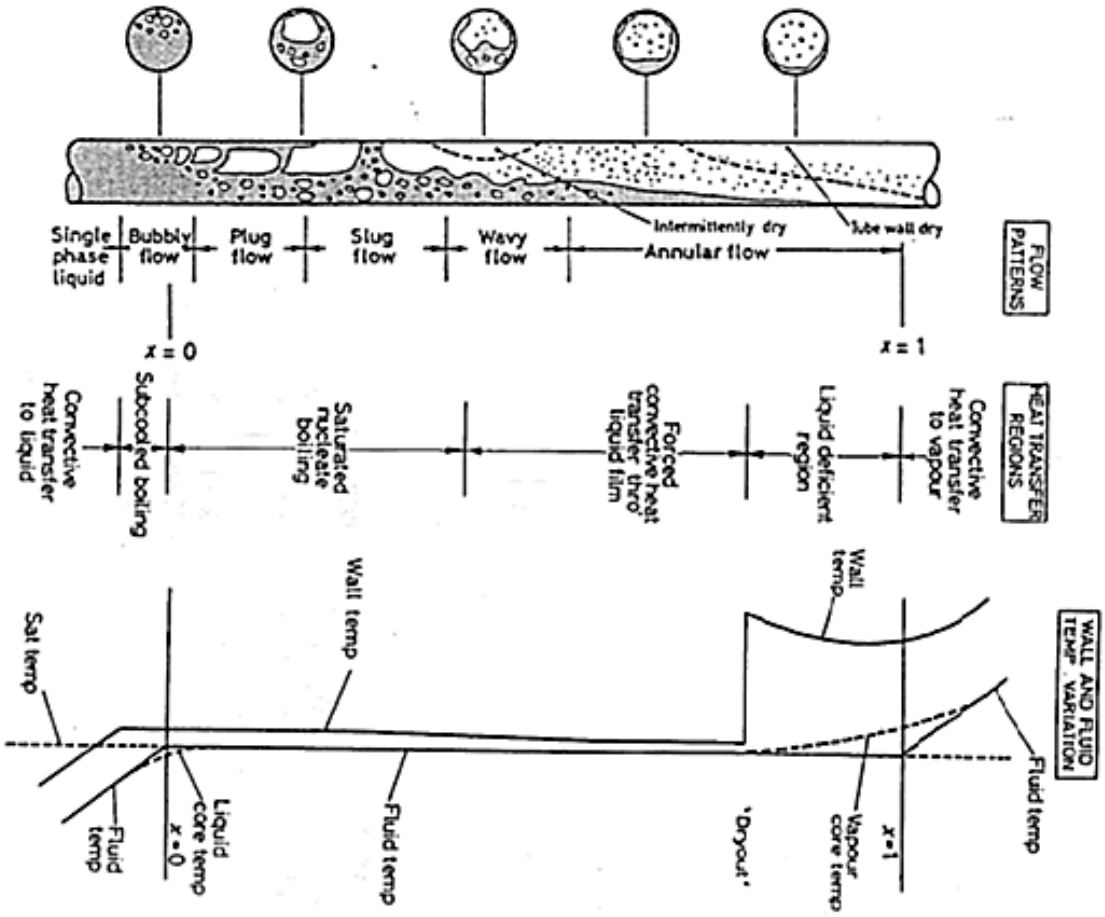

Figure 2.2: Horizontal Convective Boiling Flow Patterns, Associated Heat Transfer Regions and Wall & Fluid Temperature Variations [Adapted from (Collier, 1973)]

At very high qualities, typically near the outlet of the evaporator, a liquid deficient region is seen. Sometimes droplets may still be present in the flow and this type of flow pattern is known as a mist region. Dryout occurs when the tube walls are no longer being wetted and so a change from latent heating to sensible heating occurs resulting in an increase in the temperature of the heat transfer surface. After this, the flow quality reaches unity and there is just vapour flowing in the tube and the heat transfer mechanism is single phase forced convection of a gas.

2.2.1 Flow Pattern Maps

Flow pattern maps have been developed from empirical data such, e.g. the Baker (1954) horizontal map for air-water flows in small diameter tubes. Although corrections for other two phase mixtures are given, empirical maps tend to give erroneous results for many systems, particularly when extrapolated outside of the conditions for which they were developed, and therefore should only be used as a first guess at the flow pattern. Taitel & Dukler, 1976, developed a non-dimensional, phenomenological flow pattern map, Figure 2.3, by considering the mechanisms required for flow pattern transition to occur as shown in Figure 2.4. The expression for transition from stratified to annular or intermittent flow was found by considering the forces on a liquid protrusion in the flow.

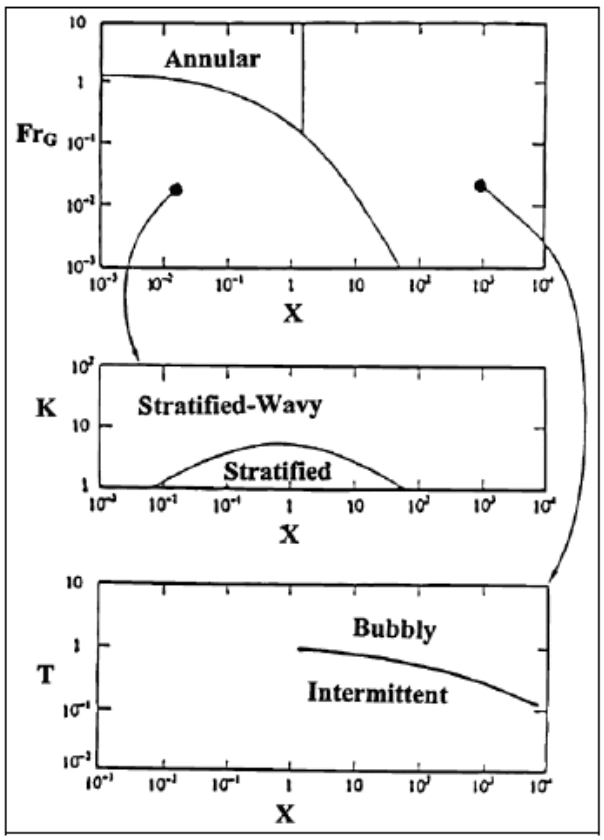

$$X = \left[\frac{(dp/dz)_L}{(dp/dz)_G}\right]^{1/2}$$

$$Fr_G = \frac{\dot{m}_G}{\left[\rho_G(\rho_L - \rho_G)d_i g\right]^{1/2}}$$

$$T = \left[\frac{\left|(dp/dz)_L\right|}{g(\rho_L - \rho_G)}\right]^{1/2}$$

$$K = Fr_G \, \mathrm{Re}_L^{1/2}$$

Figure 2.3: Taitel & Dukler Analytical Flow Pattern Map, 1976

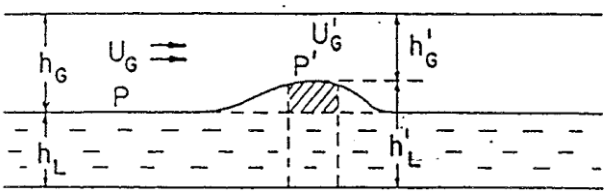

Figure 2.4: Transition Criterion Momentum Balance Methodology (Taitel & Dukler, 1976)

This protrusion causes the vapour flow to accelerate, inducing a local suction pressure on the protrusion itself. The transition occurs when this suction is large enough to cause the waves to reach the top surface i.e. intermittent or annular flow regime. For lower flow rates and lower qualities (higher liquid level), the flow regime is more likely to be intermittent, whereas higher flow rates and higher qualities can induce an annular flow pattern.

Steiner, 1993, adapted the Taitel & Dukler map by adding in the ratio of the Froude and Weber numbers which accounts for surface tension effects. Consequently higher inertial forces are required for flow pattern transitions on the map. Kattan et al., 1998, compared the flow regimes of convective boiling of 5 different refrigerants (702 data points) to the Steiner map and found that less than 50% of the data points were correctly predicted. They subsequently developed their own modified Steiner map, Figure 2.5. The axes of their map were changed to flow quality and mass flow rate. Although this makes it easier to use, it does mean that the transition boundaries change with temperature of the fluid. They added 50 kg/m^{2}s to the stratified to intermittent transition to suit their refrigerant data and they changed the annular to mist boundary to better reflect dryout conditions.

Cotton, 2000, modified both the Taitel & Dukler map and the Steiner map, without the additional 50 kg/m^{2}s modification to apply to flow through an annulus. The modified stratified-wavy to annular boundaries for an annulus are shown in Figure 2.6. This geometry of this annulus is the same as the one used in this thesis and this flow pattern map is what has been used for reference throughout this thesis.

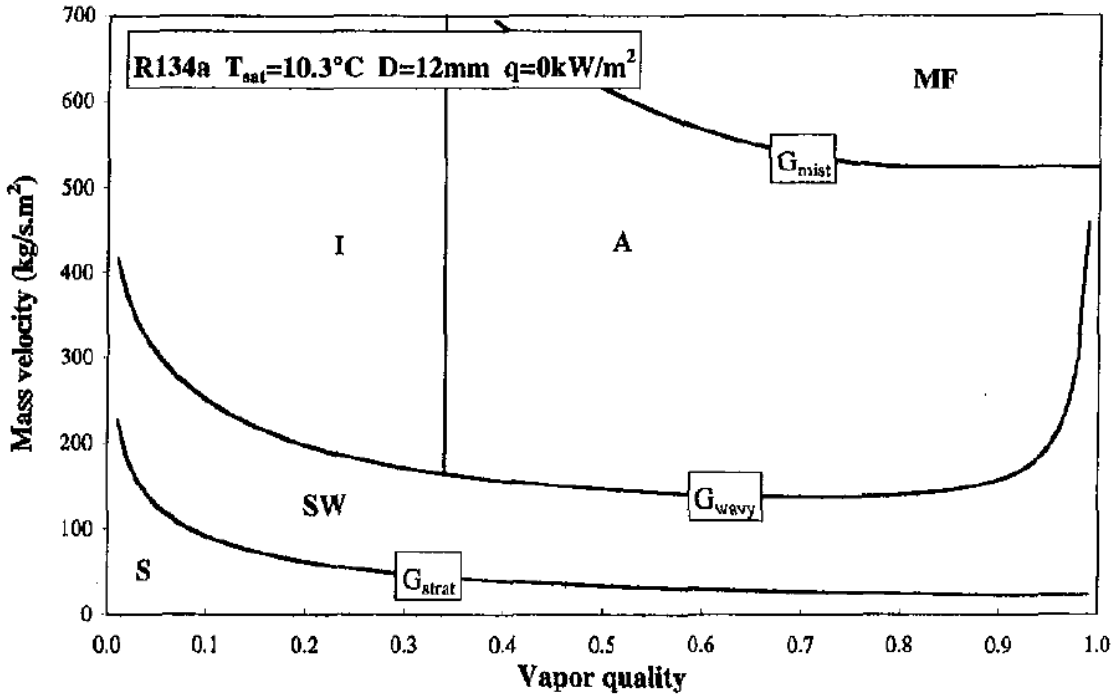

$$G_{\text{strat}} = \left\{ \frac{(226.3)^2 A_{Ld} A_{vd}^2 \rho_v (\rho_L - \rho_v) \mu_L g \cos\varphi}{x^2 (1-x) \pi^3} \right\}^{1/3} \qquad G_{\text{bubbly}} = \left\{ \frac{256 A_{vd} A_{Ld}^2 D^{1.25} \rho_L (\rho_L - \rho_v) g \cos\varphi}{0.3164 (1-x)^{1.75} \pi^2 P_{id} \mu_L^{0.25}} \right\}^{1/1.75}$$

$$G_{\text{wavy}} = \left\{ \frac{16 A_{vd}^3 g D \rho_L \rho_v}{x^2 \pi^2 (1-(2h_{Ld}-1)^2)^{0.5}} \left[\frac{\pi^2}{25 h_{Ld}^2} (1-x)^{F_1(} \right. \right. \qquad G_{\text{mist}} = \left\{ \frac{7680 A_{vd}^2 g D \rho_L \rho_v}{x^2 \pi^2 \xi_{Ph}} \left(\frac{\text{Fr}}{\text{We}} \right)_L \right\}^{0.5} \quad \text{at} \quad x < x_{\min}$$

$$\left. \left. \times \left(\frac{\text{We}}{\text{Fr}} \right)_L^{F_2(q)} + \frac{1}{\cos\varphi} \right] \right\}^{0.5} + 5 \qquad G_{\text{mist}} = G_{\min} \quad \text{at} \quad x > x_{\min}$$

Figure 2.5: Adiabatic R134a Flow Pattern Map (Kattan, et al., 1998)

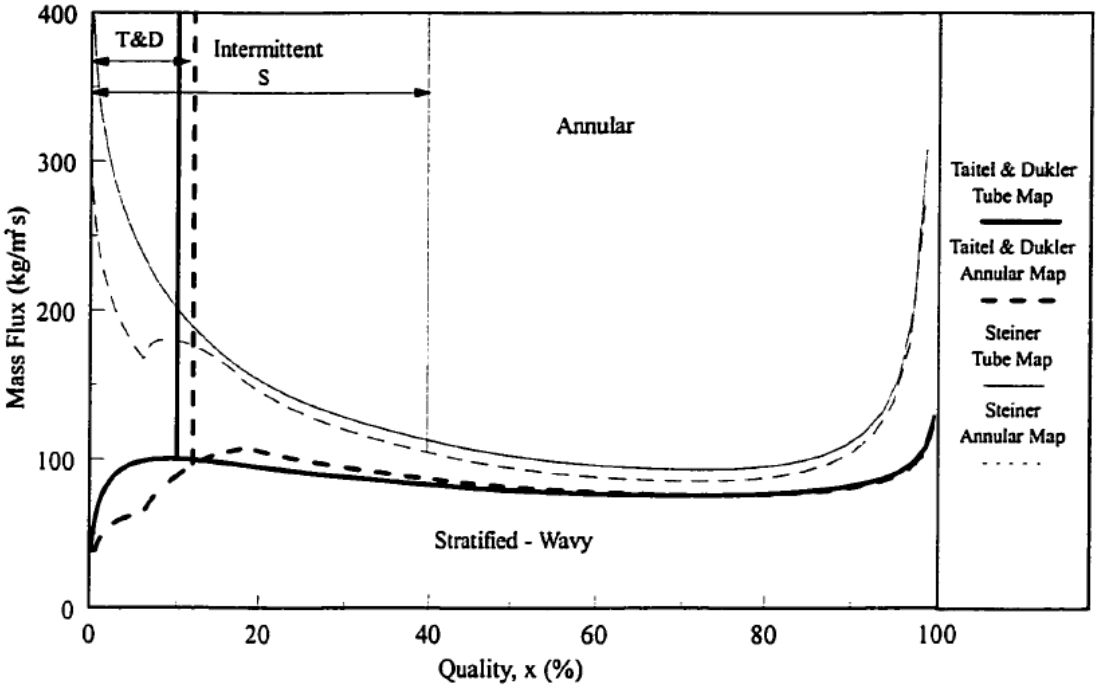

Taitel & Dukler

$$G = \left[\frac{(1 - \bar{h}_L)^2 \, \bar{A}_V^3 \, \rho_V \, (\rho_L - \rho_V) \, D_o \, g}{\bar{A}^2 \cdot d\bar{A}_L / d\bar{h}_L} \right]^{1/2} \cdot \frac{1}{x}$$

Steiner

$$G = \left(\frac{\bar{A}_V^3 \, \rho_V \, (\rho_L - \rho_V) \, D_o \, g}{\bar{A}^2 \cdot d\bar{A}_L / d\bar{h}_L} \left[\frac{\pi^2}{25 \, \bar{h}_L^2} \left(\frac{Fr}{We} \right)_L + 1 \right] \right)^{1/2} \cdot \frac{1}{x}$$

Figure 2.6: R134a Annulus Flow Pattern Map for Convective Boiling (Cotton, 2000), Tsat = 25 °C, D = 10mm

Since convective condensation is also covered briefly in this thesis, the differences in the flow pattern maps between condensation and evaporation will be mentioned. The main difference is that in condensation there will always be a liquid film on the top surface of the tube and therefore it is not possible to have a fully stratified flow. El Hajal et al., 2003, developed a flow pattern map for convective condensation of refrigerants in a similar manner to Kattan et al., 1998. This is shown in Figure 2.7 and includes the difference between condensation and evaporation.

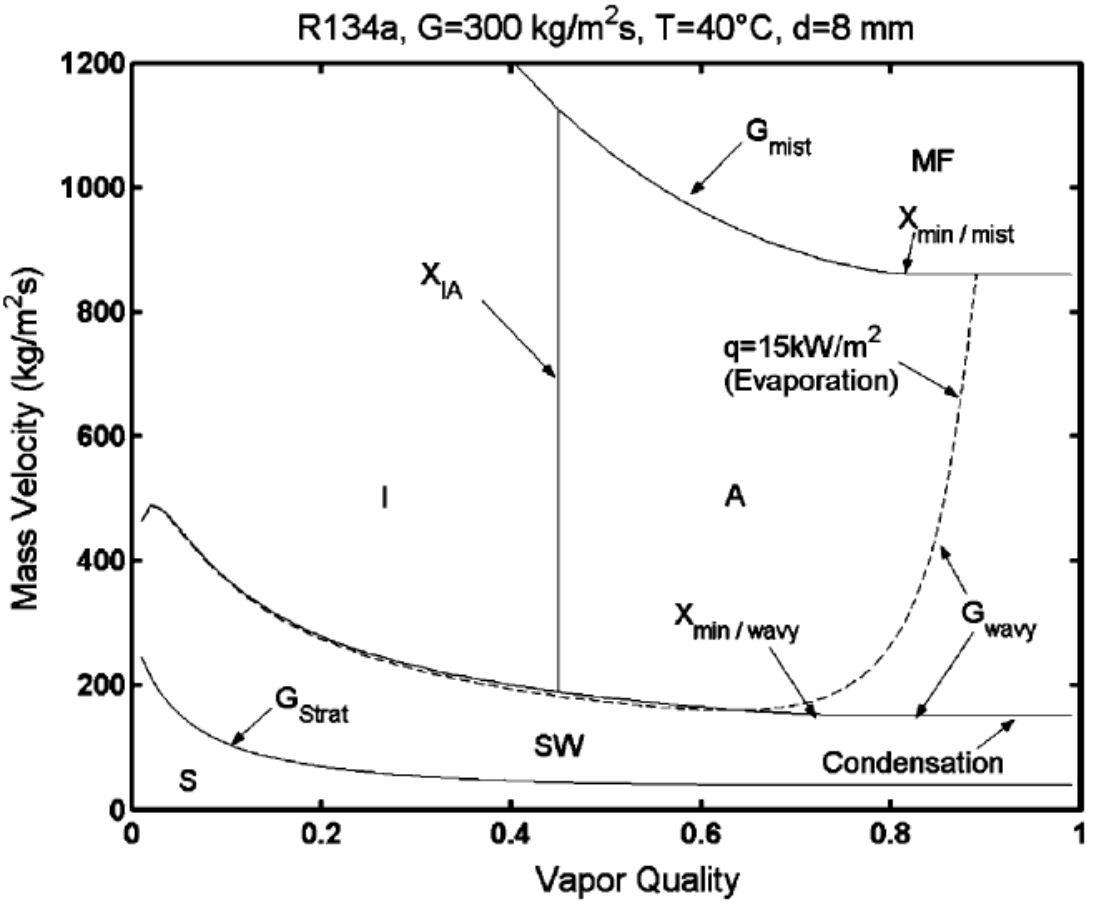

$$G_{\text{strat}} = \left\{ \frac{(226.3)^2 A_{\text{Ld}} A_{\text{Vd}}^2 \rho_{\text{V}} (\rho_{\text{L}} - \rho_{\text{V}}) \mu_{\text{L}} g}{x^2 (1-x) \pi^3} \right\}^{1/3} + 20x \qquad G_{\text{bubbly}} = \left\{ \frac{256 A_{\text{Vd}} A_{\text{Ld}}^2 d^{1.25} \rho_{\text{L}} (\rho_{\text{L}} - \rho_{\text{V}}) g}{0.3164 (1-x)^{1.75} \pi^2 P_{\text{id}} \mu_{\text{L}}^{0.25}} \right\}^{1/1.75}$$

$$G_{\text{wavy}} = \left\{ \frac{16 A_{\text{Vd}}^3 g d \rho_{\text{L}} \rho_{\text{V}}}{x^2 \pi^2 (1 - (2h_{\text{Ld}} - 1)^2)^{0.5}} \left[\frac{\pi^2}{25 h_{\text{Ld}}^2} \times \left(\frac{We}{Fr} \right)_{\text{L}}^{-1.023} + 1 \right] \right\}^{0.5} + 50 - 75 e^{-(x^2 - 0.97)^2 / x(1-x)}$$

$$G_{\text{mist}} = \left\{ \frac{7680 A_{\text{Vd}}^2 g d \rho_{\text{L}} \rho_{\text{V}}}{x^2 \pi^2 \xi} \left(\frac{Fr}{We} \right)_{\text{L}} \right\}^{0.5}$$

Figure 2.7: Flow Pattern Map for Convective Condensation (El Hajal, et al., 2003)

2.2.2 EHD Flow Pattern Maps

Cotton et al., 2005, developed a theoretical flow pattern map which included the effect of EHD on in-tube convective boiling. The transition criteria are the same as that for annular channels, Figure 2.6, except for a modified wavy to annular transition, shown in Figure 2.8. The additional shear forces due to the inner tube and the interfacial force (Melcher, 1976) due to EHD was incorporated into this transition criterion. The effect of the interfacial force was to reduce the inertia required for transition the stratified and intermittent/annular regimes. EHD was also found to have minimal effect on the intermittent to annular flow regime. This flow pattern map was used in this study as a guideline for choosing flow parameters which would show a significant effect of EHD e.g. the stratified to annular flow transition is quite pronounced.

Twisted liquid cones, twisted liquid columns and entrained droplet regimes are not dealt with specifically on this map. Depending on the liquid level and the rewetting characteristics, it is possible to have these unique EHD flow structures grouped under the terms ‘stratified wavy’, ‘intermittent’ and ‘annular’ flow regimes. Therefore, although this map is useful it should be used with caution to identify the heat transfer mechanisms associated with each flow regimes. The behaviour of the EHD flow patterns may give rise to very different heat transfer characteristics than typical non EHD flow patterns due to the effect of the new flow structures.

In addition, there is no distinction between annular flow where both the top and bottom surfaces of the tube are convective and the case where the bottom is convective and the top is a thin film flow. The heat transfer characteristics in both cases are very different and therefore caution should be used when using this for design purposes. Sadek, 2009, acknowledged that this is particularly important for the case of convective condensation where there will always be a thin liquid film on the heat transfer surface and this must be treated as a falling film condensation mechanism.

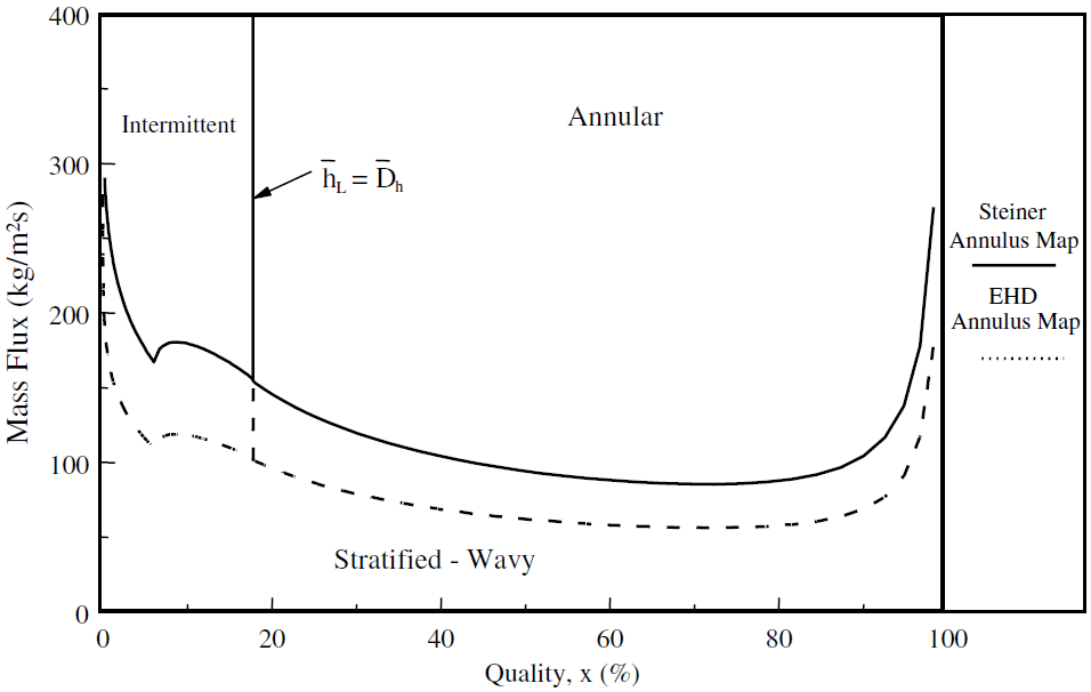

$$G \geqslant \left(\frac{\bar{A}_V^3 [(\rho_L - \rho_V) D_o g - f_e''] \left[\frac{\pi^2}{25 \bar{h}_L^2} \left(\frac{Fr}{We} \right)_L \right] + 1}{\bar{A}^2 \cdot d\bar{A}_L / d\bar{h}_L} \right)^{\frac{1}{2}} \cdot \frac{1}{x}$$

where

$$f_e'' = \frac{\varepsilon_L (\varepsilon_L - \varepsilon_V)^2}{\varepsilon_V (\varepsilon_L + \varepsilon_V)} \varepsilon_o E_L^2 = \frac{\varepsilon_V (\varepsilon_L - \varepsilon_V)^2}{\varepsilon_L (\varepsilon_L + \varepsilon_V)} \varepsilon_o E_V^2$$

Figure 2.8: R134a Convective Boiling Flow Pattern Map under the Effect of 8kVDC Applied Voltage (Cotton, et al., 2005), Tsat = 25°C, D = 10mm

2.3 Review of EHD in Single Phase Heat Transfer

As mentioned previously, the dominant force in single phase EHD heat transfer is the electrophoretic force. Researchers have moved away from single phase EHD studies in favour of two phase EHD studies, mainly because there is a greater potential for enhancement. The importance of single phase EHD research for this project is for understanding the concepts of charge injection and electroconvection so a brief review of some important studies are reviewed.

Fernandez & Poulter, 1987, investigated the effect of electroconvection in a stagnant fluid for various fluids and found that a specific 'leaf-type pattern' of fluid circulation resulted when high voltages were applied to a concentric electrode in the tube inducing a

radial electric field. This pattern is shown in Figure 2.9. Radial flow was induced and this electroconvection effect increased with increasing current and increasing temperatures. They also found that electroconvection effects were higher for negative applied voltages.

Fujino et al., 1989, studied the effect of electroconvection on single phase flow of R113 for parallel plate geometry and the effect of voltage polarity on the flow. They found, using a laser shadowgraph technique that longitudinal rolls were induced on the positive electrode side and suspected that this was due to the motion of the electrons emanating from the negative electrode via charge injection. This is shown in Figure 2.10. This ability to predict which surface is more agitated than the other can be beneficial in the design of heat transfer systems i.e. electrode placement with respect to heat transfer surface.

More recently, Ng, 2010, studied the effect of applied voltage and polarity on charge injection and electroconvection of R134a in shell and tube heat exchangers. These results agreed with those of (Fujino, et al., 1989) i.e. increasing the voltage increases the electroconvection, enhancement plateaus after 4kV and that negative polarities induce higher heat transfer as more charge was injected in this situation. The negative polarities had higher associated current and therefore had higher charge injection and calculation of the E_{hd} number showed very little change above 4kV which explains the plateau. See Figure 2.11. This figure also shows the current voltage characteristics associated with DC applied voltages. We see that the required current is very low, in the microAmp range and that negative voltages require more current, most likely due to the higher charge injection associated with this polarity.

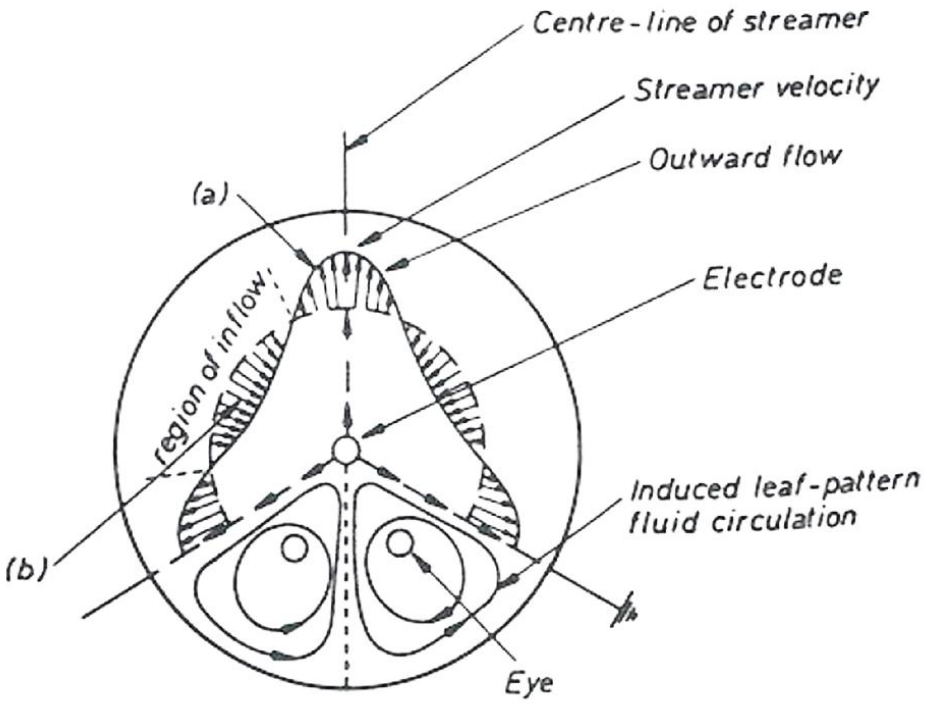

Figure 2.9: Single Phase Electroconvection: Leaf Pattern in a stationary Stationary Fluid (Fernandez & Poulter, 1987)

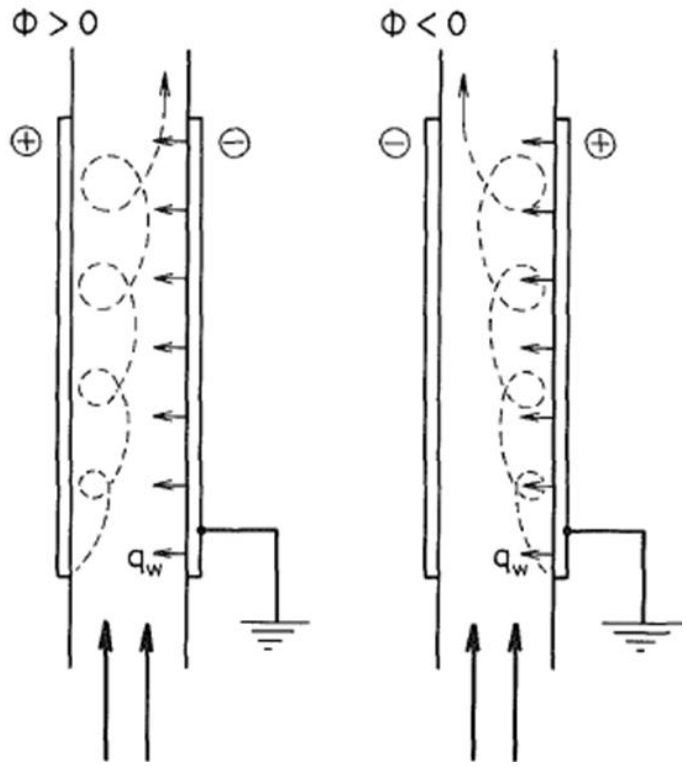

Figure 2.10: Single Phase Electroconvection in R113 Upflow (Fujino, et al., 1989)

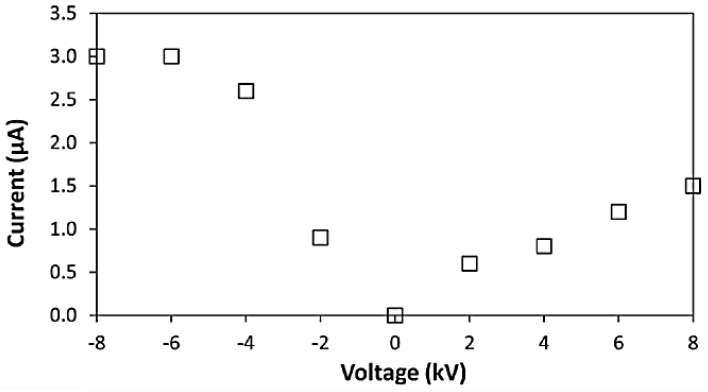

Voltage-Current characteristics for a single-phase flow ($Re_l \approx 1740$) for applied positive and negative polarity DC voltages.

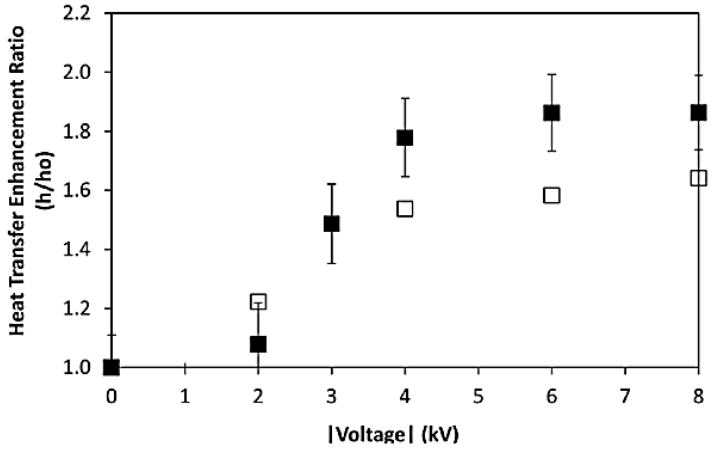

Effect of applied voltage on the heat transfer enhancement ratio in a single-phase flow ($Re \approx 1760$) for a □ positive and ■ negative applied voltage.

Figure 2.11: The Effect of Electroconvection and Polarity on Single Phase R134a Flow, Re_l = 1740 (Ng, 2010)

2.4 Review of EHD in Two Phase Heat Transfer

In two phase EHD applications the effect of the polarisation forces are dominant particularly due to the singularity $\nabla\varepsilon$ at the liquid vapour interface. This thesis primarily concerns the effect of EHD in convective boiling heat transfer applications and that is where the main literature review is focused. However some recent studies in EHD convective condensation will be discussed as these were used to validate our test rig and improvements in condensation test conditions, e.g. shortened test sections, have been incorporated into this study to gain a better understanding into the effects of EHD flow pattern effects on convective boiling.

2.4.1 EHD Convective Boiling Heat Transfer

In the early 1990's, much research was conducted into the effect of EHD enhancement on in-tube convective boiling of refrigerants such as R114, R12, R123 and

mixtures of these (Yabe, et al., 1992), (Singh, et al., 1994) (Salehi, et al., 1996). These parametric studies primarily involved positive DC voltages 0-10kV, often input via spark ignition plugs, and a range of flow qualities, mass fluxes and heat fluxes were tested. Table 2.2 gives a comprehensive list of these studies. Some general trends were found for all refrigerants; increasing the voltage induces more mixing and increasing the voltage improves the heat transfer and, in most cases, also increases the pressure drop penalty. For convective evaporation, heat transfer has been reported to increase by twofold, (Yabe, et al., 1992), (Norris, et al., 1999), (Cotton, 2000), up to tenfold, (Salehi, et al., 1997), depending on the system geometry and test conditions. Localised enhancement can get much higher or much lower if premature dryout is induced and often when long test sections are used, there are conflicting mechanisms in the flow redistribution which mask the true enhancement effects. The effect of EHD is higher at lower mass fluxes, (Cotton, et al., 2005), however, it was found that for flows with low mass flux and high quality, EHD can aid partial dryout and therefore suppress heat transfer. (Norris, et al., 1999). Since the dielectrics used are low conducting fluids, the power consumption associated with these results are in the range of <1 W or 1-2 W at most.

After the Montreal Protocol in 2006, ozone depleting refrigerants began to be phased out and researchers turned from fluids such as R22 and R12 to R134a and engineered refrigerants such as the HFE and HFO series. Parametric studies on the effect of EHD on convective boiling of R134a were carried out by numerous researchers, (Singh, et al., 1995), (Salehi, et al., 1997), (Cotton, et al., 1998). Cotton, 2000, briefly touched on the effect of polarity, an appreciable difference in the enhancement within the experimental error was not seen between positive and negative applied voltages. It should be noted that the test section used in this study was 1.5 m in length and that conflicting phase migration mechanisms along the axial length may have masked the effect of polarity.

The combination of EHD techniques and passive techniques for convective boiling was also studied. Salehi et al., 1996 investigated the effect of EHD combined with microfin tubes which resulted in an almost 4 fold increase that the heat transfer coefficient. The following year, data for EHD combined with corrugated tubes was published, (Salehi, et al., 1997), stating that 10 fold enhancement could be achieved. More recently, Posew, 2009, and Laohalertdecha, 2011, investigated the combined use of microfin tubes and EHD. However they only tested voltages up to 2.5kV, possibly due to voltage breakdown concerns. The heat

transfer coefficient in some cases doubled which is comparable to the enhancement seen in smooth tubes at voltages in the range of 6-8kV.

From heat transfer theory, it is generally accepted that an increase in heat transfer is accompanied by an increase in the pressure drop, the magnitude of which is dependent on the system geometry, fittings and components. Some papers claim that EHD has a negligible effect on the pressure drop of a system (Yabe, et al., 1992), (Posew, et al., 2009) and others claim it has a significant effect (Singh, et al., 1995), (Feng & Seyed-Yagoobi, 2003) and (Bryan & Seyed-Yagoobi, 2000). EHD does in fact have a significant impact on the pressure drop due to the additional flow redistribution and bulk mixing it induces and it is suspected that the reason why (Posew, et al., 2009) didn't see that is because they only tested voltage amplitudes up to 2.5kV DC. Cotton, 2000, indicated that low voltages like this have very little impact on the flow and pressure drops of up to twofold were seen in their test facility where the electrode assembly was designed to minimise flow interference. In the study conducted by Yabe et al., 1992, a perforated electrode was used to induce the electric fields. This electrode will have a very high pressure drop associated with the hydrodynamic boundary layer surrounding it and there are two hydrodynamic boundary layers in a concentric electrode system with only one thermal boundary layer. In these tests, the pressure drop associated with the electrode is the dominant reason for the system pressure drop and therefore increases in pressure drop associated with increases in heat transfer coefficient can be masked by this large value. Pressure drop penalties as high as 15 times the no EHD pressure drop have been reported by (Bryan & Seyed-Yagoobi, 2000), (Bryan & Seyed-Yagoobi, 2001).

As is evident from Table 2.2, the majority of previous EHD studies of convective boiling have only considered positive DC applied voltages. Cotton, 2000, conducted some limited research into the effect of positive AC signals (60 Hz and 6 kHz) on flow regime, heat transfer and pressure drop. More recently McGranaghan, 2012, has also investigated the effect AC waveforms. In addition to this, most convective boiling studies use long test sections, 1-3 m in length. Although these lengths are typically those found for evaporators in industry, it is impossible to maintain a constant flow pattern when the quality varies so greatly across the length. Ultimately EHD is known to change the flow pattern distribution and two-phase heat transfer and pressure drop are highly dependent on specific flow regimes so shorter test sections used in research provide greater insight into the true effects

of EHD. This becomes particularly apparent when there are conflicting mechanisms occurring in the system e.g. enhancement of nucleate boiling (low quality) near the inlet and suppression of heat transfer due to EHD induced dryout (high quality) near the outlet. In these cases, heat transfer enhancement ratios are not indicative of the true system enhancement. Some researchers that have used short test sections for EHD convective boiling (Salehi, et al., 1996), (Salehi, et al., 1997) and (Bryan & Seyed-Yagoobi, 2001) but they have only looked at the effect of positive DC voltages. Therefore, there is a gap in the literature regarding a full AC waveform parametric study into convective boiling enhancement while maintaining a consistent flow pattern along the axial length of the test section.

EHD has been described as an active enhancement technique. The main advantage of active enhancement techniques is that they offer the ability to change the voltage input i.e. an ability to control the system heat transfer instead of just enhancing it as passive methods do. There is a gap in the literature between the scientific effects of EHD enhancement of heat transfer and the actual use of EHD as a control application.

2.4.2 A Note on EHD Convective Condensation Heat Transfer

Similar to EHD convective boiling enhancement, there has been considerable research into EHD convective condensation enhancement for the potential to improve heat exchanger/condenser designs, (Gidwani, et al., 2002), (Cotton, 2009), (Sadek, 2009) and (Ng, 2010). Parametric studies have been conducted by these researchers where the effect of DC electric field on the heat transfer and pressure drop characteristics of convective condensation of various refrigerants (various fluid and electrical parameters) were recorded. Parameters such as heat flux, quality, mass flux, electrode design as well as smooth versus enhanced tubing were investigated. A general trend of increased EHD increasing the heat transfer and pressure drop was reported and the mechanisms of enhancement are generally similar to those in the case of evaporation except the aim is to remove the liquid film from the heat transfer surface instead of rewetting the heat transfer surface.

For the purpose of this study, the work of (Sadek, 2009) and (Ng, 2010) is most important. In both of these cases, a short, 30 cm test section was used. This meant that the flow regime could be maintained approximately constant across the test section and since heat transfer enhancement is a function of the flow regime, this modification can provide invaluable

insight into the mechanisms of EHD enhancement. For example, Sadek, 2009, noticed that there were differences in the transient EHD flow patterns compared to the steady state flow patterns. 'Twisted liquid cone' flow structures were reported during the transient period and this led to an investigation into the effect of AC waveform parameters, such as frequency and duty cycle on the flow pattern and therefore heat transfer and pressure drop characteristics. This investigation was continued in some detail by Ng, 2010, whereby an effort was made to sustain the transient flow structures to obtain different heat transfer and pressure drop characteristics to enlarge the window of EHD controllability of heat transfer. Other flow patterns were observed by doing this such as the 'Twisted liquid column regime' and the 'entrained droplet flow'. However it was found that sustaining the transient waveforms did not offer higher enhancement. In addition, the effect of polarity was seen more clearly with the short test section and Ng, 2010 found that positive polarity voltages enhanced convective condensation more than negative voltages due to uptake of liquid into the core region thereby reducing the thermal resistance of the condensate film on the heat transfer surface. Table 2.3 shows the positive and negative polarity hypotheses as discussed in Ng, 2010. Steps 1 and 2 are the same for both polarities whereby the liquid is extracted toward the electrode and surrounds the electrode surface. Step 3 is where the differences start to occur. The negative charges that are injected by the cathode are in differing locations in the tube for varying polarity. For positive polarities, they are on the outer tube, they oppose the repulsion due to the electrophoretic force and twisted liquid cones form as a result whereas for negative voltages, the negative charges are on the electrode, they assist the repulsion due to the electrophoretic force and twisted liquid columns form.

Table 2.2: Literature Review: Horizontal Convective In-Tube Boiling

Year	Researcher	Fluid	Tube	Inner Tube Diameter [mm]	Test Section Length [m]	Electrode	Electrode Diameter [mm]	Tsat	Mass Flux [kg/m2s]	Quality Range	Heat Flux [kW/m2]	EHD Waveforms	Heat Transfer Enhancement	Pressure Drop Penalty	Power Consumption	Effect of Polarity	Control	Flow Regime constant	Heat Transfer Correlation
1992	yabe	R123, R134a	smooth	10	3.75	perforated coaxial cylinder	5	30	33 & 66	0-0.9	4	DC	2fold	negligible		no	no	no	no
1994	singh	r123	smooth	9.4	1.22	ss cylindrical	3	27.5	50-400	0-0.5	5-20.	DC	4.75	7	<1W	no	no	no	no
1995	singh	r134a	smooth	9.4	1.22	ss cylindrical	3	20	50-400	0-0.5	5-20.0	DC	3fold	7	<1W	no	no	no	no
1996	salehi	r404a	microfin	12.7	0.3	helical	9.9	25	50 &100	0-0.6	10	DC	3.7fold		negligible	no	no	yes	no
1997	salehi	r134a	smooth + corrugated	9.5	0.3	cylindrical	9.8	25	50-200	0-0.8	25	DC	10fold			no	no	yes	no
1998	cotton	r134a	smooth	10.9	1.5	ss cylindrical,eccentric	3.18	25	100-500	0.0.2	10-20.	DC	2-3fold	1.8-2.6	1-2W	no	limited	no	no
1999	norris	r134a	smooth	10.9	1.5	cylindrical	3.18	25	100-250	0.2-0.5	10-40.0	DC	1.5			no	limited	no	no
2000	Bryan	r134a	smooth	14.1	0.3	cylindrical brass	1.6	5	100-300	0-0.89	5-150	DC	2-5.	2-15.		no	no	no	no
2000	cotton thesis	r134a	smooth	10.9	1.5	ss cylindrical,eccentric	3.18	25	50-550	0-0.6	10-25.0	DC, AC (limited)	2-3fold	1.8-2.6	1-2W	limited	limited	no	no
2001	Bryan and seyed yagoobi	r134a	smooth	14.1	0.3	cylindrical, brass	1.6	5	100-300	0-0.6	5-150	DC	6.5	2-15.		no	limited	yes	no
2003	feng	r134a	smooth	14.1	0.3	cylindrical, brass	1.6	5	100-300	0-0.6	5-150	DC	6.5	2-15.		no	no	annular	yes
2005	cotton	r134a	smooth	10.9	1.5	ss cylindrical,eccentric	3.18	20	50-550	0-0.6	10-25.0	DC, AC (limited)	2-3fold	1.8-2.6	1-2W	no	limited	no	no
2009	posew	r134a	smooth + micrfoin	9.52	2.5	ss cylindrical	1.47	25	400	0-0.6	10-20.	DC low level	1-2fold	negligible	negligible	no	no	no	yes
2011	laohalertdecha	r134a	smooth + microfin	8.5	2.5	ss cylindrical	1.47	20	200-600		7	DC low level	1-2fold	negligible	negligible	no	no	no	yes
2012	Present Study Nangle-Smith	r134a	smooth	10.9	0.3	ss cylindrical	3.18	25	60	0.35-0.45	08-10.	DC, AC	2-5fold	2-5fold	1-2W	yes	EHD control of load conditions	yes	future work

*Sections adapted from Cotton, 2000

Table 2.3: Polarity Hypotheses for Transient Behaviour upon Application of High Voltage Waveforms to a stratified wavy R134a flow in an annulus, D = 10mm, Tsat = 25°C (Ng, 2010)

Positive Polarity Hypothesis:

Step 1: Liquid Extraction
- Liquid extraction to electrode due to higher electric field
- Negative charge injection into liquid bulk from outer tube

Step 2: Liquid Reaches Electrode
- Electrode surrounded by fluid
- Negative charges accumulate on electrode surface

Step 3: Liquid Repulsion
- Liquid repulsed from electrode towards outer tube due to higher electric field in vapour region, negative charges opposes repulsion due to electrophoretic force
- Twisted liquid cone flow structures that bridge gap between electrode and tube

Step 4: Steady State
- Balance between dielectrophoretic and electrophoretic forces is achieved. Lower liquid layer decreased and electrode is surrounded by a layer of liquid
- Twisted liquid cones are no longer present
- Occasional bridging of liquid from bottom stratum to electrode due to charge accumulation in the lower stratum

Negative Polarity Hypothesis:

Step 1: Liquid Extraction
- Liquid extraction to electrode due to higher electric field

Step 2: Liquid Reaches Electrode
- Electrode surrounded by fluid
- Negative charge injection into liquid surrounding electrode

Step 3: Liquid Repulsion
- Liquid repulsed from electrode towards outer tube due to higher electric field in vapour region, negative charges assist repulsion due to electrophoretic force
- Twisted liquid column flow structures that bridge gap between electrode and tube later observed

Step 4: Steady State
- Balance between dielectrophoretic and electrophoretic forces is achieved. Lower liquid layer decreased and electrode is surrounded by a layer of liquid
- Twisted liquid columns are no longer present
- Occasional bridging of liquid from bottom stratum to electrode due to charge accumulation in liquid surrounding electrode

2.5 Heat Transfer and Pressure Drop Models and Correlations

For two phase flows the heat transfer and pressure drop characteristics are dependent on the flow pattern. Since EHD redistributes the flow, creating new flow patterns, it can have a significant effect on the system heat transfer and pressure drop. Correlations to calculate the heat transfer and pressure drop characteristics for a system based on flow pattern and are outlined here.

2.5.1 Convective Boiling Correlations

Figure 2.2 shows the heat transfer mechanisms associated with the various flow patterns encountered with internal convective boiling. For the single phase liquid and vapour regions at the extreme ends of the tube, the Dittus-Boelter, 1930, single phase heat transfer correlation can be used with an accuracy of ±15%.

$$\mathrm{Nu} = 0.023\ \mathrm{Re}^{0.8}\mathrm{Pr}^{n} \qquad \textbf{Eqn. 2. 13}$$

Where n = 0.4 for boiling and 0.33 for condensation.

The two-phase region is more interesting and more difficult to analyse. The complexity of two phase flow analysis can be simplified using various assumptions to eliminate terms in the momentum equations. Two important models are used here: the homogenous model and the separated model. The homogenous model is the simplest, it assumes that both phases have equal velocities, the system is in thermodynamic and mechanical equilibrium and homogenous properties, Equation 2.14, i.e. a mixture of the two phases, so that only one momentum equation needs to be solved. This model is only useful for flow regimes that behave in a homogenous manner i.e. well mixed, high flow rate, bubbly or mist flows. The separated model is slightly more complex. It assumes that the system is in thermodynamic and mechanical equilibrium and that the velocities of both phases are constant but not equal. Although this simplifies the equations, empirical correlations are still required to solve the problem.

$$\frac{1}{\boldsymbol{\rho_H}} = \frac{x}{\rho_v} + \frac{1-x}{\rho_l} \qquad \frac{1}{\boldsymbol{\mu_H}} = \frac{x}{\mu_v} + \frac{1-x}{\mu_l} \qquad \textbf{Eqn 2.14}$$

2.5.1.1 Convective Boiling Heat Transfer Coefficient

Convective boiling has aspects of nucleate boiling and forced convective heat transfer. Hence the heat transfer coefficient/energy balance is given as a combination of these two factors.

$$\dot{q}_{total} = \dot{q}_{nuc} + \dot{q}_{conv} \qquad \textbf{Eqn 2.15}$$

The nucleation term is dominant for low quality flows i.e. in the bubbly regime and the forced convective term is more dominant at higher flow qualities. Many semi-empirical correlations have been published regarding this equation and Darabi et al., 1995, provides a good summary. In this review a number of the correlations are compared for various refrigerant data and the correlation recommended for use in horizontal refrigerant flow,

including annular tubes, is that by (Liu & Winterton, 1991). This correlation, Equation 2.16, was found to have a mean deviation of for all data points tested 20.5%.

$$\mathrm{h}_{total} = \left[\left(S\mathrm{h}_{pool}\right)^2 + (E\mathrm{h}_l)^2\right]^{1/2} \qquad \textbf{Eqn 2.16}$$

Here h_{pool} is the heat transfer for pool boiling defined by Cooper, 1984, and h_l is the forced convective heat transfer coefficient found using the Dittus-Boelter, 1930, relation. S and E are the pool boiling suppression factor and the forced convection enhancement factor, respectively. They are functions of the liquid Reynolds number, the liquid Prandtl number and the flow quality and determine the importance of each mechanism for the specified conditions to give an accurate representation of the two phase heat transfer coefficient.

$$\mathrm{h}_l = 0.023(k_l/d)Re_l^{0.8}Pr_l^{0.4} \;:\; \mathrm{h}_{pool} = 55P_r^{0.12}q^{2/3}(-\log_{10}P_r)^{-0.55}M^{-0.5} \qquad \textbf{Eqn 2.17}$$

Kattan et al., 1998 developed a new methodology, outlined in Figure 2.12, to establish the two phase flow pattern and the two phase heat transfer coefficient from the given system parameters. This methodology was compared to published refrigerant data and was found to have a standard deviation of 16.8% for 1141 datapoints. Figure 2.13 shows the heat transfer coefficient for varying mass fluxes and how it relates to the flow pattern.

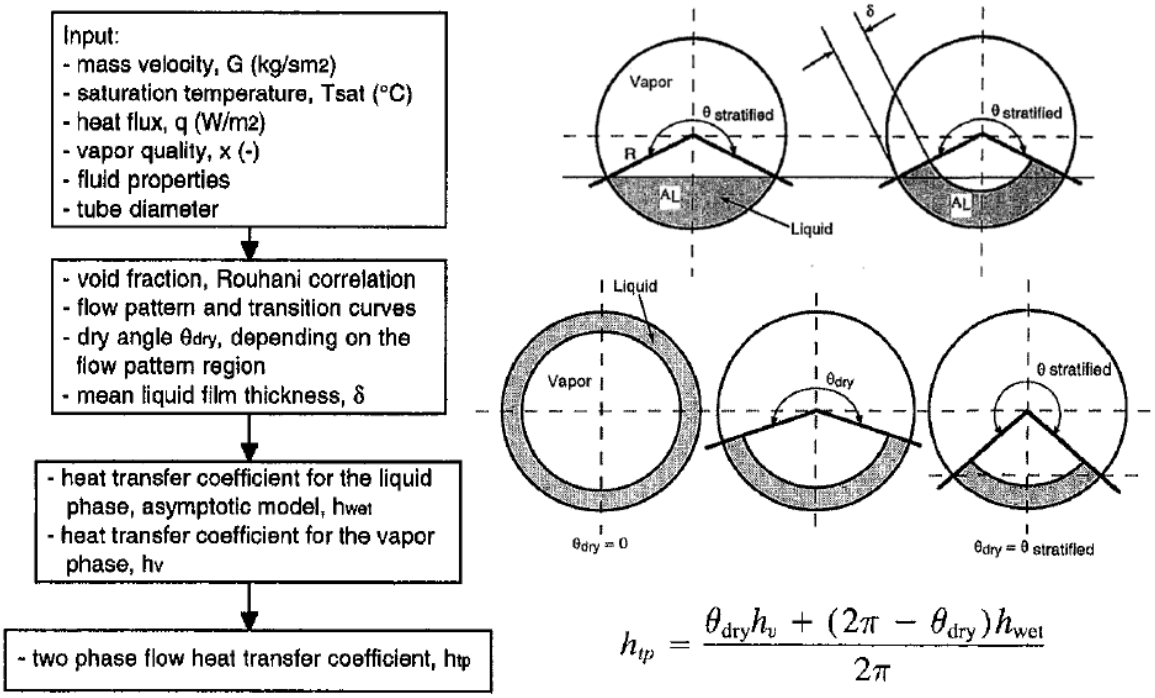

Figure 2.12: Two phase Heat Transfer Coefficient Correlation Methodology for Refrigerants (Kattan, et al., 1998)

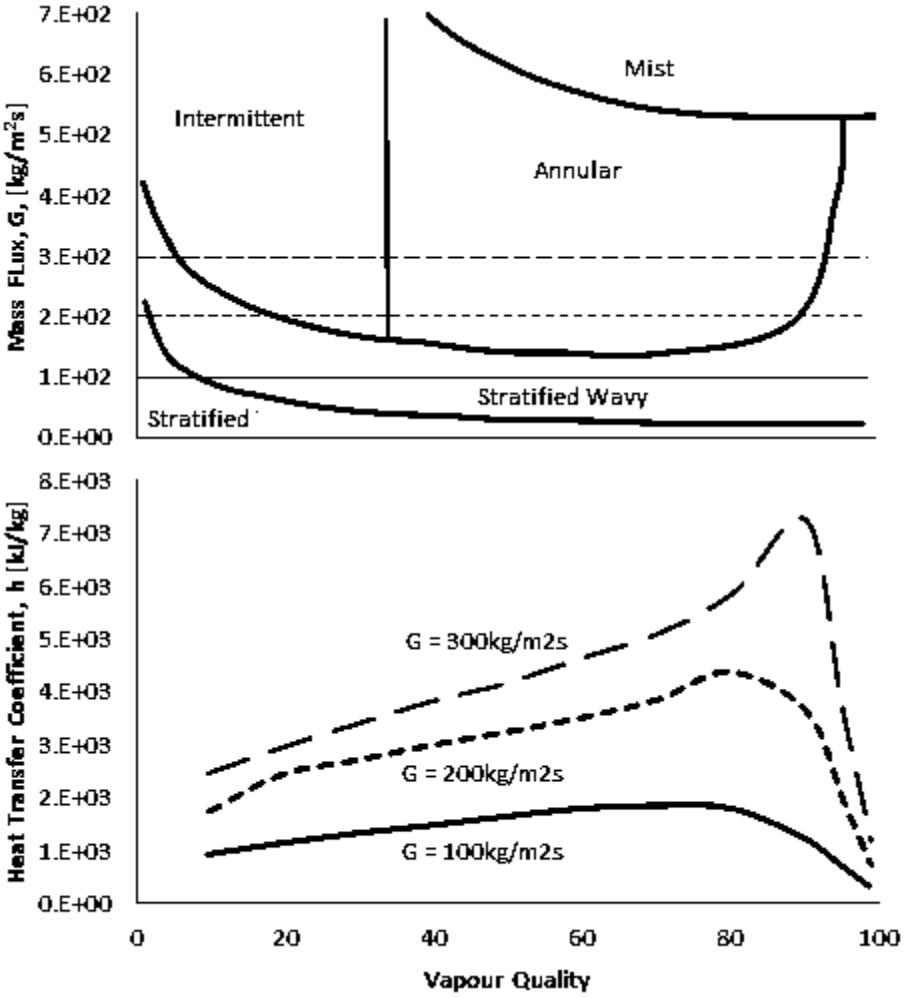

Figure 2.13: Heat Transfer Coefficients for Various Mass Fluxes and Vapour Qualities and the Correlation to Flow Pattern (Kattan, et al., 1998)

It should also be noted that an equivalent heat transfer correlation to the Kattan model for convective boiling is the El Hajal et al., 2003, model for convective condensation as this was developed in a similar manner to the Kattan et al., 1998, methodology.

Although the Kattan model accounts for dryout, the correlation for the liquid region always assumes a convective heat transfer mode. In convective evaporation, surface wetting can cause thin films on the upper tube surfaces which exhibit a different mechanism of heat transfer. Additionally, the mist flow region and EHD flow patterns need to be treated separately. For liquid film boiling, few experimental investigations of have been conducted due to the flow rates and high temperatures required to produce a thin liquid film flow. In general, the vapour will flow at a much higher velocity and consequently the liquid vapour interface for this flow pattern is subject to wavy perturbations which increase interfacial area and enhance heat transfer. Jayanti & Hewitt, 1997, conducted a numerical analysis into the

hydrodynamics and heat transfer of thin liquid film flows and showed that the overall heat transfer coefficient is influenced mainly by conduction through the film, rather than by recirculation for three common wave shapes, Figure 2.14, associated with falling film flow. The heat transfer coefficients were plotted for each wave shape so to get a value, one much know the film thickness and estimate the wave shape. The wave velocity field in this study was obtained such that a balance between the wall shear stress and the gravitational forces were achieved. If the effect of EHD on liquid film conduction were to be analysed, the EHD body force would need to be included in this balance.

The heat transfer modes in the mist flow region include; convection from the from wall to the vapour, convection from the vapour to the entrained droplets, evaporation of

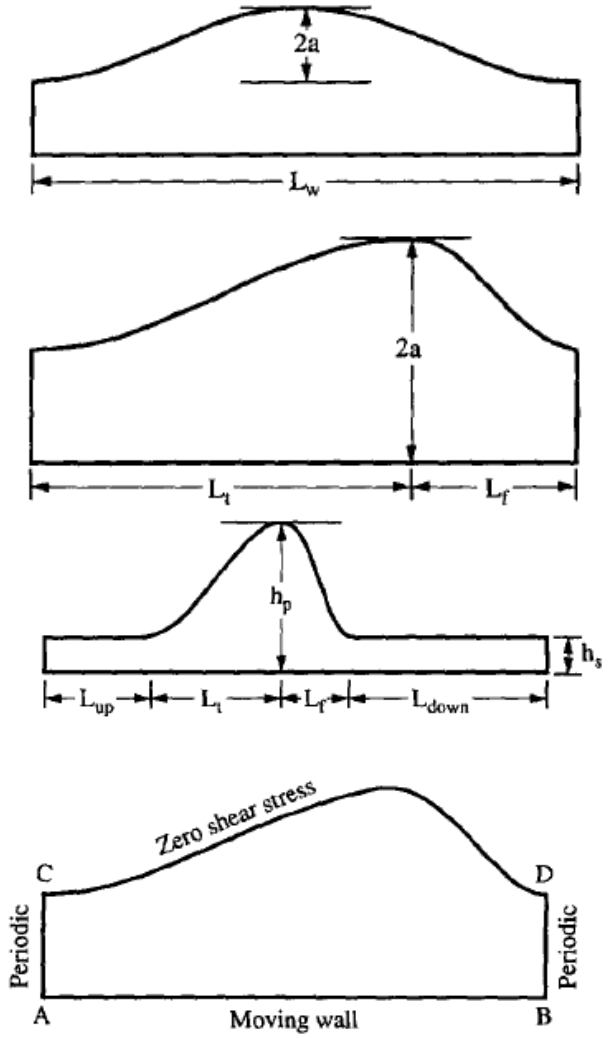

Figure 2.14: Liquid-Vapour Interface Wave Shapes of the Falling Film (i) sinusoidal (ii) distorted sinusoidal (iii) solitary roll (iv) boundary conditions on the flow domain (Jayanti & Hewitt, 1997)

droplets in the core region and when they wet the wall and radiation to the droplets and the vapour. (Carey, 1992) A theoretical model which takes into account all of these factors has not been achieved to date and it is mostly empirical correlations that are used to predict the heat transfer. The US Nuclear commission recommends either the Groeneveld, Equation 2.18, or Dougall-Rosenhow correlation. (Groeneveld, 1973)

$$\mathrm{Nu} = \frac{hD}{k_v} = a\left[\left(\frac{GD}{\mu_v}\right)\left(x + \frac{\rho_v}{\rho_l}\,(1-x)\right)\right]^b \cdot Pr_{v,w}^{c} Y^d \qquad \textbf{Eqn 2.18}$$

where

$$Y = 1 - 0.1\left(\frac{\rho_v}{\rho_l} - 1\right)^{0.4}(1-x)^{0.4} \qquad \textbf{Eqn 2.19}$$

The Prandtl number is evaluated at the wall temperature and the other properties are evaluated at the saturation temperature. Table 2.4 shows the coefficients to be used based on the tube geometry.

Table 2.4: Groeneveld Correlation Coefficients for Various Geometries

Geometry	a	b	c	d
Tubes	0.00109	0.989	1.41	-1.15
Annuli	0.0520	0.688	1.26	-1.06
Tubes and annuli	0.00327	0.901	1.32	-1.5

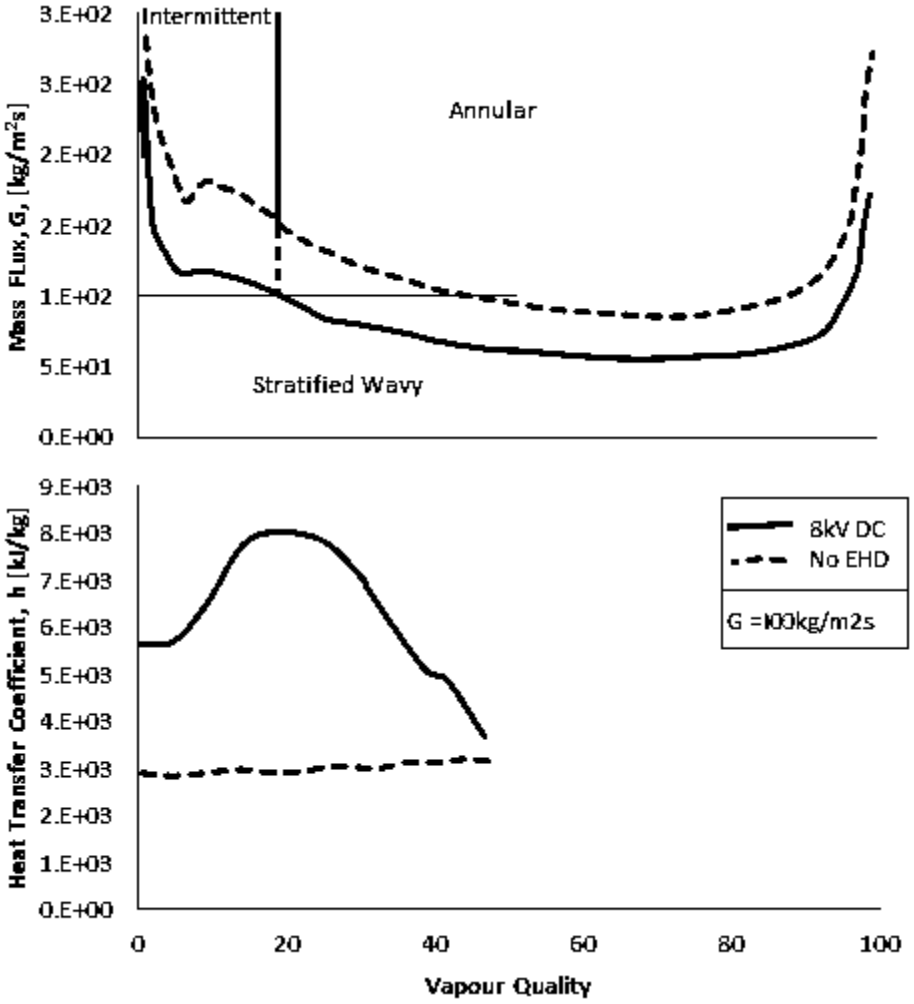

Figure 2.15: The effect of +8kV DC on Heat Transfer Coefficient for R134a Convective Boiling at G = 100kg/m^{2}s and the Correlation to Flow Pattern (Cotton, 2000)

The heat transfer associated with EHD flow regimes such as twisted liquid columns, cones and jets has not been explicitly modelled either. Currently the enhancement ratio is used based on flow condition without application of high voltage to determine an equivalent increase in heat transfer for specific geometries and system parameters. Some correlations have been proposed regarding the effect of EHD on heat transfer and pressure drop. Cotton, 2000, numerically simulated the electric field for various flow distributions and used these to explain the heat transfer and pressure drop results obtained. A two-phase flow pattern map was subsequently developed (Cotton, et al., 2005) so for design applications, the effect of EHD can be correlated to a specific flow regime and then current flow pattern-dependent correlations for heat transfer and pressure drop can be used. A selection of heat transfer results based on both flow pattern and EHD parameters from Cotton, 2000, are shown in Figure 2.15 to show how heat transfer can be related to the EHD flow pattern. It should be

emphasised that no general method for predicting the EHD heat transfer coefficient exist, and the above methods are specific to the test section geometry and fluid data that they were generated from.

2.5.1.2 Two Phase Pressure Drop Correlations

The pressure drop in a two phase flow consists of three components: the frictional component, the gravitational component and the acceleration component. The frictional component is generally the largest component and is always present. The gravitational component can generally be neglected for horizontal flows and the acceleration component can be neglected if there is no change in momentum in the fluid. For flows where there is a large change in density, for vertical flows or when there is heating, the acceleration component should be considered.

The total pressure drop for the homogenous model given by Equation 2.20.

$$\frac{\partial \mathrm{P}}{\partial \mathrm{z}} = \left(\frac{\partial \mathrm{P}}{\partial \mathrm{z}}\right)_f + \left(\frac{\partial \mathrm{P}}{\partial \mathrm{z}}\right)_a = -\frac{f}{D}\frac{G^2}{2\rho_H} + \frac{\partial(\dot{\mathrm{m}}/\rho_H)}{\partial \mathrm{z}} \qquad \textbf{Eqn 2.20}$$

where f is the friction factor and can be found using the Colebrook relation or the Moody diagram.

The pressure drop for the separated model is more complicated. For the friction component only, Lockhart & Martinell, 1947, proposed that the two phase frictional pressure drop could be calculated by scaling the single phase frictional pressure drop by a two phase multiplier.

$$\left(\frac{\partial \mathrm{P}}{\partial \mathrm{z}}\right)_f = \Phi_l^2 \left(\frac{\partial \mathrm{P}}{\partial \mathrm{z}}\right)_l \quad or \quad \left(\frac{\partial \mathrm{P}}{\partial \mathrm{z}}\right)_f = \Phi_v^2 \left(\frac{\partial \mathrm{P}}{\partial \mathrm{z}}\right)_v \qquad \textbf{Eqn 2.21}$$

where

$$\left(\frac{\partial \mathrm{P}}{\partial \mathrm{z}}\right)_l = -\frac{f_l}{D}\frac{G^2(1-x)^2}{2\rho_l} \;\&\; \left(\frac{\partial \mathrm{P}}{\partial \mathrm{z}}\right)_v = -\frac{f_v}{D}\frac{G^2(x)^2}{2\rho_v} \qquad \textbf{Eqn 2.22}$$

Lockhart&Martinelli, 1947 proposed the following as the two phase flow multipliers

$$\Phi_l^2 = 1 + \frac{C}{X} + \frac{1}{X^2} \qquad \Phi_v^2 = 1 + CX + X^2 \qquad \textbf{Eqn 2.23}$$

where C is between 5-20 for turbulent flow and X is the Martinelli Parameter used previously in the flow pattern maps.

$$X = \left(\frac{\mu_l}{\mu_v}\right)^{n/2} \left(\frac{1-x}{x}\right)^{(2-n)/2} \left(\frac{\rho_l}{\rho_v}\right)^{1/2} \quad \textbf{Eqn 2.24}$$

where n is 0.2 or 0.25 for smooth pipes.

Chisholm, 1973 developed a correlation for C based on fluid parameters and the slip velocity.

$$\frac{1}{S}\left(\frac{\rho_l}{\rho_v}\right)^{1/2} + S\left(\frac{\rho_v}{\rho_l}\right)^{1/2} \quad \textbf{Eqn 2.25}$$

Martinelli & Nelson, 1948 developed a new relationship between the two phase multiplier and the Martinelli number for evaporating water flow over a wide pressure range and they redefined the multiplier as Φ_{lo}^2 instead of Φ_l^2.

$$\Phi_{lo}^2 = \frac{(\partial \mathrm{P}/\partial \mathrm{z})_l}{(\partial \mathrm{P}/\partial \mathrm{z})_{lo}} \quad \textbf{Eqn 2.26}$$

The denominator of Equation 2.26 is the frictional pressure drop if it were only fluid flowing in the tube. Several other researchers developed relationships for the two phase modifier, some of the most notable include: Baroczy, 1966, Chisholm, 1973, and Friedel, 1979. Souza et al., 1993, developed a two phase pressure drop correlation for refrigerants flowing in smooth, horizontal 10.9 mm diameter tubes and is dependent on the liquid Froude number.

$$\Phi_{lo}^2 = (1.376 + c_1 X^{-c_2})(1-x)^{1.75} \quad \textbf{Eqn 2.27}$$

For $0 < Fr \leq 0.7$	For $Fr > 0.7$
$c_1 = 4.172 + 5.48Fr - 1.564Fr^2$	$c_1 = 7.242$
$c_2 = 1.773 - 0.169Fr$	$c_2 = 1.655$

The acceleration term was also proposed (Souza, et al., 1993) for the separated model.

$$(\Delta \mathrm{P})_a = G^2 \left(\left[\frac{x_{out}^2}{\rho_v a_{out}} + \frac{(1-x_{out})^2}{\rho_l (1-a_{out})}\right] - \left[\frac{x_{in}^2}{\rho_v a_{in}} + \frac{(1-x_{in})^2}{\rho_l (1-a_{in})}\right]\right) \quad \textbf{Eqn 2.28}$$

Several flow pattern based pressure drop correlations have been published such as Bandel, 1973, Beattie & Whalley, 1982, and the ARD model developed by Hart, Hamersma & Fortuin, 1989. Further details on these relations can be found in Carey, 1992. Figure 2.16 shows an example of a flow pattern based, two phase pressure drop graphical correlation for R410A, small diameter tubes, mass flux of 300 kg/m^{2}s and heat flux of 7.5 kW/m^2. We see that the

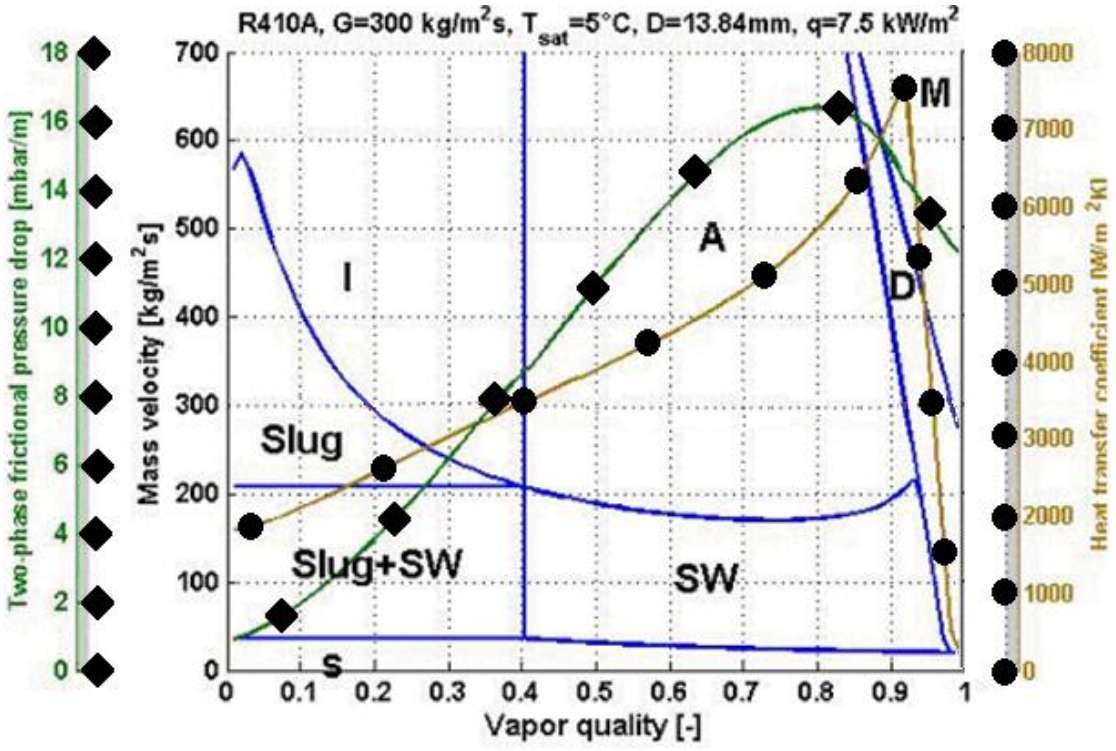

Figure 2.16: Wojtan et al., 2005 Flow Pattern Map, Moreno-Quiben & Thome, 2006 Two Phase Frictional Pressure Drop Model and Wojtan et al. 2005 Flow Boiling Model Overlaid (wlv databook III, Chapter 13)

pressure drop increases steadily as the flow pattern varies from stratified through to intermittent and annular flow. When the vapour quality is high enough that a mist flow pattern exists, the pressure drop starts to decrease.

Pressure drop EHD correlations have not been explicitly modelled. As the electrode geometry is often different for different EHD studies, it is difficult to separate out the pressure drop due to system geometry, flow parameters and EHD effects. Therefore, in most studies the pressure drop penalty ratio is used, similar to the heat transfer enhancement ratio discussed in the section 2.5.1.1. Feng & Seyed-Yagoobi, 2003, completed a turbulence spectral analysis of EHD in annular flow patterns and used this to establish that the pressure drop ratio is a function of the friction pressure drop (calculated using the Friedel correlation) and the momentum exchange cause by the phase change. A regression analysis on experimental test data was used to tune the coefficients specific to boiling and condensation. The test data of Bryan & Seyed-Yagoobi, 2000, and Feng & Seyed-Yagoobi, 2003 was used to establish the boiling coefficients and the data of Singh, 1994, and Singh, 1995, was used to establish the condensation coefficients. See Equations 2.29a-c. The model was only developed for annular flow conditions and shows very good agreement for annular

flow with high mass fluxes. The obvious limitation of this model is that it is only applicable for annular flow but it is also possible that it may not be very easy to adapt to other flow regimes such as stratified wavy with low mass flux because the effect of EHD will be a lot greater and the some of the assumptions may not be very applicable. For example, the Interfacial electric force not taken into account, it is assumed that the presence of electrode doesn't significantly influence the pressure gradient or the Reynolds stress distribution and the molecular viscosity is ignored since it is small compared with the turbulent viscosity. Neglecting the molecular viscosity may pose problems when trying to model flow patterns at low mass fluxes and although an annular flow pattern has a low electrode pressure gradiant associated with it due to vapour being in contact with it, it is unlikely that this would be the case for most of the EHD induced flow patterns where there is significant turbulent fluid flow in the vicinity of the electrode.

$$\frac{\Delta P_{EHD}}{\Delta P_0} = function\left(\frac{\int_0^L P_{EHD} dz/L}{\Delta P_{fr}|_{no\ EHD}}\right) \qquad \textbf{Eqn 2.29a}$$

$$\left.\frac{\Delta P_{EHD}}{\Delta P_0}\right|_{Boiling} = 1.01 \cdot \frac{\int_0^L \frac{P_{EHD} dz}{L}}{\Delta P_{fr}|_{no\ EHD}} + 0.87 \qquad \textbf{Eqn 2.29b}$$

$$\left.\frac{\Delta P_{EHD}}{\Delta P_0}\right|_{Condensation} = 0.62 \cdot \frac{\int_0^L \frac{P_{EHD} dz}{L}}{\Delta P_{fr}|_{no\ EHD}} + 2.24 \qquad \textbf{Eqn 2.29c}$$

Similar to Figure 2.15 for heat transfer coefficient, Figure 2.17 shows the graphical correlation of the two phase pressure drop with its associated EHD flow patterns. (Cotton, 2000)

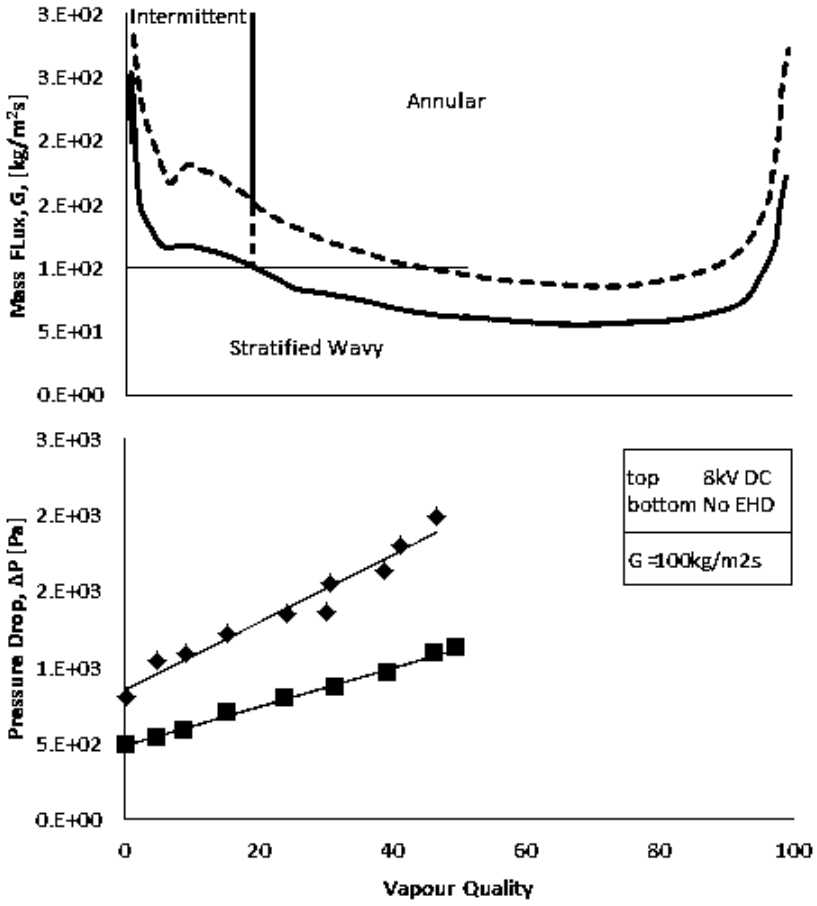

Figure 2.17: The effect of +8kV DC on Pressure Drop for R134a Convective Boiling at G = 100kg/m^{2}s and the Correlation to Flow Pattern (Cotton, 2000)

The fundamentals of electrohydrodynamics, heat transfer and two phase flow patterns have been discussed in this chapter to provide a better understanding into how EHD affects the flow redistribution and ultimately how this impacts the heat transfer and pressure drop characteristics. It has been established that there is a gap in the literature when it comes to convective boiling while maintaining a consistent flow pattern along the test section length, the influence of polarity on flow redistribution and a more in-depth pulse waveform parametric study.

Chapter 3:
Experimental Test Facility

In this chapter, the experimental test facility, experimental procedure, data reduction methods and experimental uncertainties are discussed. The test facility used is the same as that most recently used by Ng, 2010 and previously by Sadek, 2009 for convective condensation experiments. It is capable of testing the effects of electrohydrodynamics (EHD) on single phase refrigerant flows as well as convective boiling and condensation refrigerant flows in a horizontal, annular tube.

3.1 Refrigerant Loop

The experimental test facility contains a closed loop charged with refrigerant, R134a, at a pressure of 550 kPa. This corresponds to a saturation temperature of approximately 25 ^{o}C thereby minimising heat losses to the surroundings. A schematic of the rig is shown in Figure 3.1. The refrigerant is pumped around the loop via a gear pump (Pacific Scientific Model 2217560) controlled by a variable speed electric motor. It then passes through one of two turbine flowmeters where the refrigerant volumetric flow rate is measured. For flow rates in the range: 0.1-1 L/min the refrigerant is directed through an Omega FTB-501 flowmeter and for higher flowrates, it is directed through an Omega FTB-101 (1.3-13 L/min).

The refrigerant is then heated to the desired test section inlet quality. For the purposes of the current experiments only electric heating was used. However there is a hot water, plate heat exchanger (preheater) in the loop when higher inlet qualities are required. The electric heater consists of two 1.8 m long, stainless steel tubes connected in parallel to a Miller C-ST-250 power supply (maximum capacity of 6.4 kW) which has a controlled current output. The stainless steel tubes (Outer Diameter 12.7 mm OD, 0.25 mm wall thickness) are electrically insulated at each end using ceramic Swagelok® Unions. The electric heat added to the refrigerant is calculated by measuring the voltage across the two tubes and the current using a shunt resistor.

$$Q_{ELEC} = I(V_1 + V_2) \qquad \textbf{Eqn. 3.1}$$

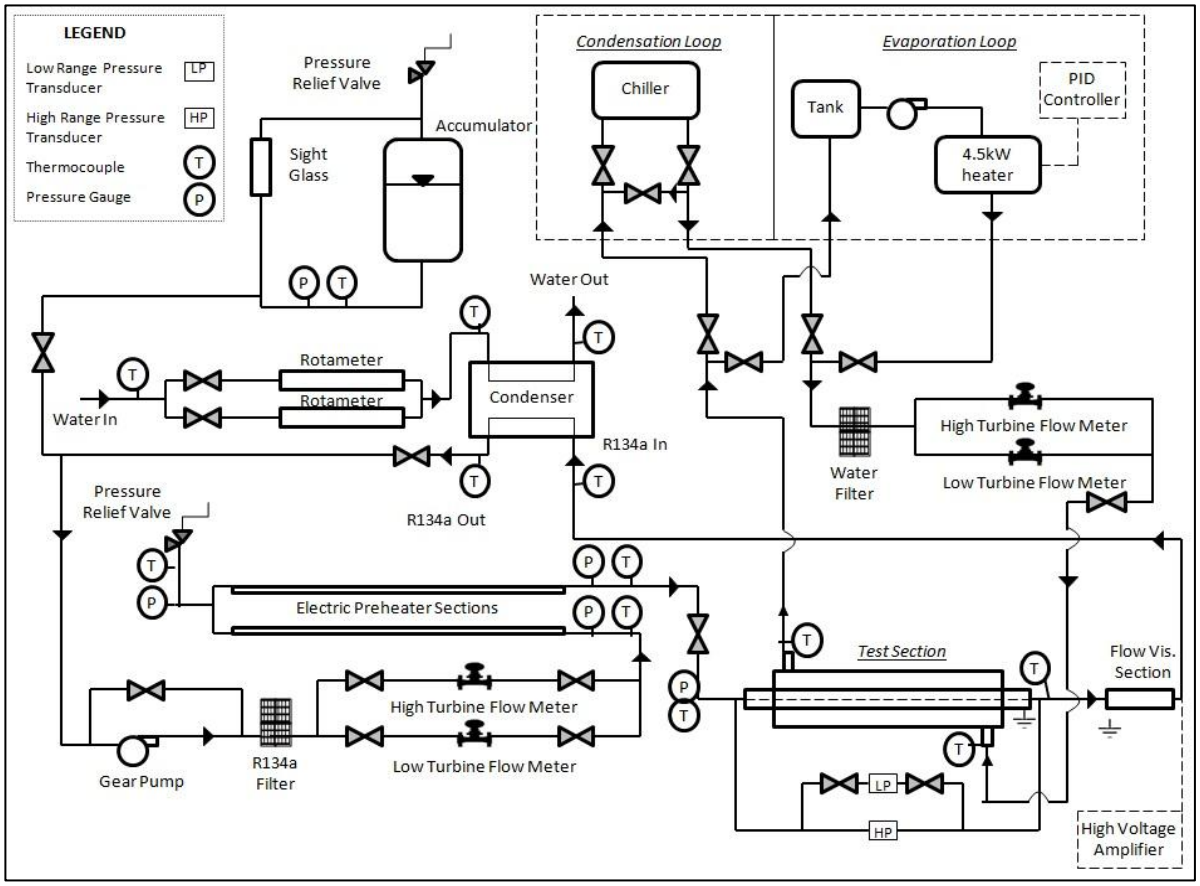

Figure 3.1: Schematic of the Test Facility

The refrigerant passes through 50D of piping to ensure fully developed flow before reaching the test section (heat exchanger) after which it passes through a single-pass, co-axial condenser (Maximum Capacity 30 kW) which returns the refrigerant to the subcooled state required for pumping. The flowrate to the condenser is manually recorded by one of two Fischer & Porter® Series 10A rotameters: 0-3.1 L/min or 0-10.2 L/min. The heat transfer through the condenser is then calculated using Equation 3.2:

$$Q_{cond} = \dot{m}_{water,cond} C_{p,water} (T_{water,cond,out} - T_{water,cond,in}) \qquad \textbf{Eqn. 3.2}$$

There is a pressurizer located between the gear pump and the condenser outlet which can be used to manually control the loop pressure in the range of 0.3 MPa to 0.9 MPa using an immersed electrical heater (1 kW) or coiled water cooler to either increase or decrease the pressure, respectively. The pressuriser is also equipped with safety pressure switch to turn off the heater above a specified pressure and a pressure relief valve to remove refrigerant into a recovery cylinder.

Temperature and pressure locations are shown in Figure 3.1. At these locations the temperature is measured using T-type thermocouple probes, 1.6 mm diameter and the pressure is measured by analog spring-type gauges mainly for condition monitoring purposes. Pipe insulation (Rubatex: R-180 FS) is used to minimise heat loss to the environment and the heat lost/gained between the outlet of the condenser and the inlet to the electric heater is accounted for using Equation 3.3.

$$Q_{loss} = \dot{m}_{ref} C_{p,ref} (T_{ref,sub} - T_{ref,cond,out}) \qquad \textbf{Eqn. 3.3}$$

3.2 Test Section

The test section, as shown in Figure 3.2 is an annular, horizontal, single-pass, counter-current, shell and tube heat exchanger. The refrigerant flows on the tube side (stainless steel, inner diameter 10.2 mm, outer diameter 12.7 mm) and water flows on the shell side (PVC, inner diameter 19.1 mm, wall thickness 3.8 mm). The refrigerant passes through 50D of straight tubing before reaching the test section so it is hydrodynamically fully developed but it is thermally developing once it enters the test section. The heat exchanger length is 30 cm which is short enough to be able to maintain a constant flow pattern across the test section for the current test conditions. The inlet and outlet flow patterns are monitored by means of plastic viewing sections at the inlet and the outlet of the test section.

The inlet and outlet refrigerant temperatures are measured using 1.6 mm, T-type thermocouples and the surface temperatures on the inside of the refrigerant pipe are measured using 0.5 mm T-type thermocouples. Twelve surface thermocouples are embedded in the refrigerant tube: four circumferential measurements at three axial locations as shown in Figure 3.2 and Figure 3.3. In addition to their use in calculating the heat transfer coefficient, analysis of the surface temperature profiles and their standard deviation can be used to give an indication of the flow pattern in the tube.

The pressure drop in the test section is measured using a Validyne DP-15 differential pressure transducer which is connected to a 2-channel Validyne signal conditioner. Depending on the pressure range, one of two diaphragms is used: Low range (0-1.4 kPa) or High range (0-3.5 kPa). These diaphragms can be switched on the fly by means of an equalisation loop between them. The tube connecting the pressure transducer to the test section passes through a water jacket which condenses the vapour to equalise the hydrostatic head on each side of the transducer.

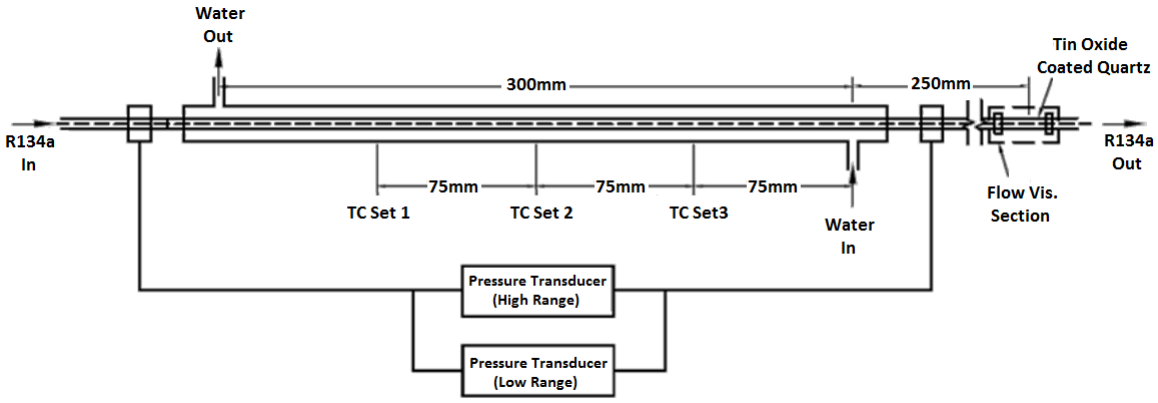

Figure 3.2: Schematic of the Test Section

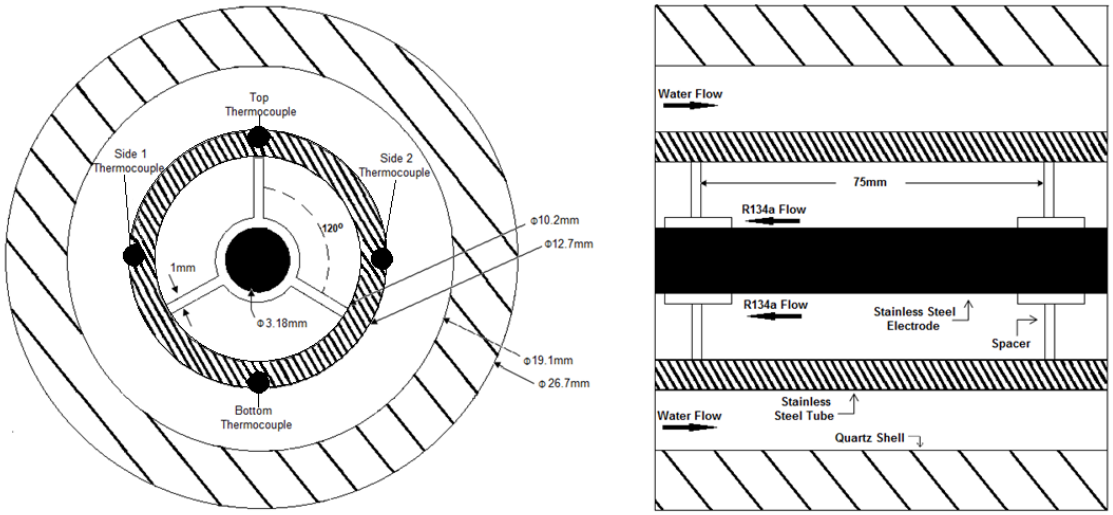

Figure 3.3: Test Section – Cross Section, Thermocouple & Electrode Arrangement (not to scale)

At the outlet, as seen in Figure 3.2, there is a transparent, quartz tube viewing section. This tube is coated with a thin, transparent layer of electrically conducting tin oxide on the outside of the tube that bridges the ground connection between the stainless steel refrigerant tubes. Flow visualisation using a High Speed Imaging 'Fastec Troubleshooter' high speed camera was used to monitor the effect of EHD on flow pattern at this location.

3.3 Water Side Condensation & Evaporation

The water side of the heat exchanger is a closed loop that can provide either heating or cooling to the test section and can be seen in Figure 3.1 - the 'condensation loop' and 'evaporation loop' sections.

For the condensation loop, a Lytron RC045 chiller (maximum cooling capacity 5.9 kW), recirculates chilled water at a specified temperature. The flow rate can be controlled by

means of a bypass loop back into the chiller. In the evaporation loop, a centrifugal pump pumps the water through a 4.5 kW, three-coil, single phase, screwplug type heater. This heater is powered by a 600V AC power supply and the temperature can be controlled using a PID controller. The flow rate can be controlled by means of a bypass loop back into the reservoir.

In both cases, both the temperature and the flow rate of the water can be used to control the heat flux. The test section inlet and outlet water temperatures are measured using 6 mm platinum resistance temperature detectors (RTD's) connected to an Omega DP-251 thermometer reader. For low flow rates, 0.2-2 L/min, a McMillan 104 Flo-sensor micro turbine is used to measure the test section water flow rate and for higher flow rates an Omega FTB-101 turbine flow meter (1.32-13 L/min) is used. The heat flux applied to the refrigerant in the test section is calculated using Equation 3.4:

$$Q_{water} = \dot{m}_{water} C_{p,water} (\Delta T_{RTD}) \qquad \textbf{Eqn. 3.4}$$

3.4 Application of High Voltage Signals

As can be seen in Figure 3.3, a concentric stainless steel electrode (3.18 mm diameter) is the source of the electric field in the test section. Signals are generated using a Tektronix AFG 3021B function generator that is connected to the low voltage side of a TREK 20/20C high voltage amplifier. The current output of this amplifier is limited to 20 mA. The output of the amplifier is connected, via a brass connector, to the electrode through the test section outlet. The current and voltage output of the amplifier is monitored using an Agilent oscilloscope.

The electrode is kept in position using three spacers at 75 mm intervals in the test section. The spacers are fabricated from Delrin which has a dielectric constant of approximately 2.5 and are designed to be small and streamlined to minimise flow interference. The outer stainless steel tube of the test section is grounded and the test section and viewing section is electrically isolated to ensure that the refrigerant is subject to an electric field only in the test section.

The effect of continuous (DC), sine and pulse (AC) waveforms on convective boiling were tested. Parameters such as DC level, peak-peak voltage, frequency and duty cycle were varied. The following figure indicates the most important signal parameters.

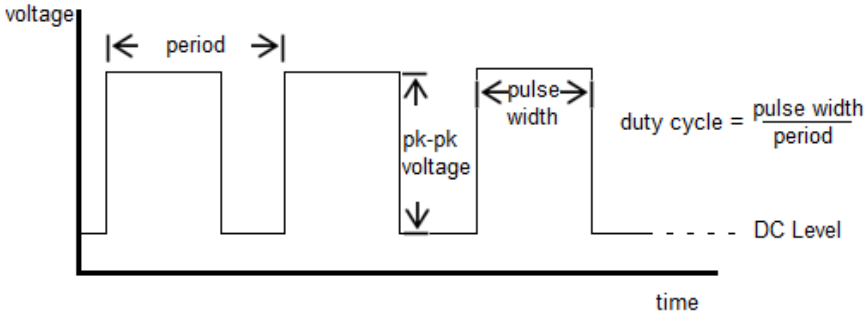

Figure 3.4: Signal Parameters

3.5 Data Acquisition System (DAQ)

A LabVIEW® program is used to monitor the control parameters for the system in real time, to determine when the system has reached steady state and to record the data used to analyse the heat transfer and pressure drop performance. Table 3.2 shows the parameters that are measured using the data acquisition system. These values are the average value of 1000 samples taken over a 10 second period. The data is connected to National Instruments® SCXI card which is connected to a DAQ PCI-6221 board in a computer. The SCXI card has a resolution of 16-bits and the PCI-6221 is a 16 channel analog input board that is capable of sampling at a rate of 250 kSamples/s per channel.

Figure 3.5 shows the full DAQ connection diagram. Thermocouple measurements are passed through a signal conditioner before being sent to the DAQ Board and the surface temperature thermocouples are sent to an electrically insulated signal conditioner to minimise the electrical noise. Since there are twelve surface thermocouples and only eight channels on the SCXI-1125, the thermocouples need to be swapped and a second recording is required. An ice bath at 0 ^{0}C, as specified in (ASTM STP 470, 1970) is used as the cold junction reference for all of the thermocouple measurements.

Table 3.1 Experimentally Calculated Parameters

Symbol	Measured Parameter	Equation
X_{in}	Test Section Inlet Quality	Eqn 3.9
X_{out}	Test Section Outlet Quality	Eqn 3.10
q”	Test Section Heat Flux	Eqn 3.4
Qcond	Heat lost in the Condenser	Eqn 3.2
Qloss	Heat lost/gained to/from the surroundings	Eqn 3.3
Qelec	Heat Added by the Electric Heater	Eqn 3.1
h	Test Section Heat Transfer Coefficient	Eqn 3.7

Table 3.2 Experimentally Measured Parameters

Symbol	Measured Parameter	Measurement Method
$\dot{m}_{water}$	Volumetric water flow rate in test section	DAQ
$\dot{m}_{ref}$	Volumetric refrigerant flowrate	DAQ
$\dot{m}_{cond}$	Volumetric of municipal water through condenser	Manual
V_1, V_2	Electric Heater Voltage	Manual
I	Electric Heater	Manual
ΔP	Test Section Differential Pressure Drop	DAQ
ΔT_{RTD}	Water Temperature difference across test section	DAQ
T_{ref_sub}	Refrigerant inlet temperature (subcooled)	DAQ
T_{ref_in}	Refrigerant test section inlet temperature	DAQ
T_{ref_out}	Refrigerant test section outlet temperature	DAQ
$T_{ref\_cond\_in}$	Refrigerant condenser inlet temperature	DAQ
$T_{ref\_cond\_out}$	Refrigerant condenser outlet temperature	DAQ
$T_{water\_cond\_in}$	Water condenser inlet temperature	DAQ
$T_{water\_cond\_out}$	Water condenser outlet temperature	DAQ
T_{water_in}	Test section water inlet temperature	DAQ
T_{water_out}	Test section water outlet temperature	DAQ
$T1_{s\_bottom}$	Test section surface temperature: Location 1, bottom	DAQ
$T1_{s\_top}$	Test section surface temperature: Location 1, top	DAQ
$T1_{s\_side1}$	Test section surface temperature: Location 1, side 1	DAQ
$T1_{s\_side2}$	Test section surface temperature: Location 1, side 2	DAQ
$T2_{s\_bottom}$	Test section surface temperature: Location 2, bottom	DAQ
$T2_{s\_top}$	Test section surface temperature: Location 2, top	DAQ
$T2_{s\_side1}$	Test section surface temperature: Location 2, side 1	DAQ
$T2_{s\_side2}$	Test section surface temperature: Location 2, side 2	DAQ
$T3_{s\_bottom}$	Test section surface temperature: Location 3, bottom	DAQ
$T3_{s\_top}$	Test section surface temperature: Location 3, top	DAQ
$T3_{s\_side1}$	Test section surface temperature: Location 3, side 1	DAQ
$T3_{s\_side2}$	Test section surface temperature: Location 3, side 2	DAQ
V_{ehd}	Voltage Applied to the Electrode	Manual
I_{ehd}	Current Applied to the Electrode	Manual

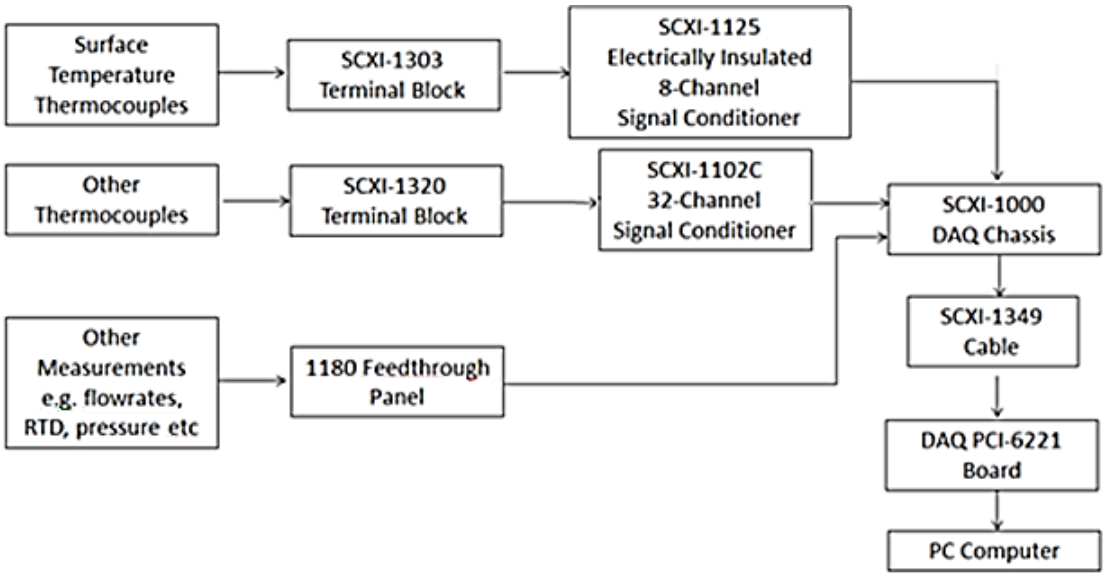

Figure 3.5: Layout of the Data Acquisition System

3.6 Data Reduction

The pressure drop, as mentioned already is measured directly. The heat transfer coefficient is found from a test section energy balance equating the energy lost or gained by the refrigerant to the energy lost or gained by the water depending on whether condensation or evaporation is being studied. The energy lost or gained by the refrigerant can be expressed as:

$$Q_{ref} = h_{avg} A_s (T_{ref,sat} - T_{s,avg}) \qquad \textbf{Eqn. 3.5}$$

where $T_{s,avg}$ is the average surface temperature in the test tube given by:

$$T_{s,avg} = \frac{1}{12} \sum_{i=1}^{12} T_{s,i} \qquad \textbf{Eqn. 3.6}$$

Equating Equations 3.4 and 3.5 we can get an expression for the heat transfer coefficient in terms of measured parameters, geometric parameters and fluid properties.

$$h_{avg} = \frac{\dot{m}_{water} C_{p,water} (\Delta T_{RTD})}{A_s (T_{ref,sat} - T_{s,avg})} \qquad \textbf{Eqn. 3.7}$$

Often heat transfer and pressure drop enhancement ratios are quoted when comparing the performance with and without EHD i.e. h/h_o and $\Delta P/\Delta P_o$.

The inlet quality is calculated by considering that the electric heat input has to be equal to the sensible energy added to heat refrigerant from subcooled to saturated and the latent energy added to get the refrigerant from saturated to the desired inlet quality.

$$Q_{ELEC} = \dot{m}_{ref} C_{p,ref} \left(T_{ref,sat} - T_{ref,sub}\right) + \dot{m}_{ref} h_{fg,ref} x_{in} \quad \textbf{Eqn. 3.8}$$

Rearranging gives:

$$x_{in} = \frac{I(V_1+V_2) - \dot{m}_{ref} C_{p,ref} \left(T_{ref,sat} - T_{ref,sub}\right)}{\dot{m}_{ref} h_{fg,ref}} \quad \textbf{Eqn. 3.9}$$

The outlet quality is calculated similarly to the inlet quality but there is an additional energy term due to the heat added or removed by the water in the test section. This results in the following equation.

$$x_{out} = \frac{I(V_1+V_2) - \dot{m}_{ref} C_{p,ref} \left(T_{ref,sat} - T_{ref,sub}\right) - \dot{m}_{water} C_{p,water} (\Delta T_{RTD})}{\dot{m}_{ref} h_{fg,ref}} \quad \textbf{Eqn. 3.10}$$

Finally the average quality is simply given by:

$$x_{avg} = \frac{x_{in} + x_{out}}{2} \quad \textbf{Eqn. 3.11}$$

In the range of testing conducted in the current study, the quality, x, varied by 10% between the inlet and the outlet i.e. at G = 60 kg/m^{2}s, xin = 35%, xout = 45% which maintains a constant stratified wavy flow pattern along the test section as predicted in the flow pattern map in Figure 2.8.

3.7 Experimental Procedure

1. The refrigerant mass flux is set by adjusting the gear pump to the required value.
2. The condenser flow rate is adjusted to give the required subcooled temperature at the inlet to the electric heater.
3. The electric heater is used to set the inlet quality to the desired value
4. The water temperature and flow rate are set to get the required test section heat flux value
5. Minor adjustments are made to each of these parameters as they are not all independent.
6. Steady state is usually reached after three hours for the first setpoint; defined as when the subcooled temperatures deviate by no more than ±0.1^{0}C for no less than 15 minutes.
7. Data is recorded by the DAQ and data reduction is performed on the results.
8. A flow or EHD parameter is varied. This will generally change the mass flux, heat flux and quality. The system is adjusted to return these parameters to their original value

and steps 6-8 are repeated. Generally steady state for all other setpoints is achieved after approximately one hour.

3.8 Uncertainty Analysis

Table 3.3 summarises the uncertainties associated with the experiments performed for this thesis. The full analysis can be found in Appendix A. Uncertainty was calculated in accordance with (Kline & McClintock, 1953).

The uncertainty of measured parameters e.g. flow rate, is a combination of the 'bias error', which is essentially the instrument error as quoted by the manufacturer and the 'precision error', which is twice the standard deviation of the experimental measurements taken. The precision error for the experiments varies so the worst case scenario was used to calculate the uncertainty.

$$\delta x_i = \sqrt{(B)^2 + (P)^2} \qquad \textbf{Eqn. 3.12}$$

The uncertainty of calculated parameters e.g. heat transfer coefficient, can be calculated from the measurement uncertainties from which it is derived.

$$\delta f = \sqrt{\sum_{i=1}^{n} \left(\frac{\delta f}{\delta x} \delta x_i\right)^2} \qquad \textbf{Eqn. 3.13}$$

Table 3.3 Experimental Uncertainties

Measurement, x_i		**Precision Error**	**Bias Error**	**Total Uncertainty**
RTD ΔT_{water}	^{o}C	±0.08	±0.04	±0.09
Thermocouple Temp.	^{o}C	±0.24	±0.22	±0.33
Refrigerant Flowrate	kg/s	$\pm 1.2 \times 10^{-3}$	$\pm 1.3 \times 10^{-5}$	$\pm 1.2 \times 10^{-3}$
Water Flowrate	kg/s	$\pm 2 \times 10^{-4}$	$\pm 3 \times 10^{-4}$	$\pm 3.6 \times 10^{-4}$
Pressure Drop (Low)	Pa	±10	±11	±15
Pressure Drop (High)	Pa	±18	±13	±23

Parameter, f		**Relative Uncertainty**
Heat Flux, q"	kW/m^2	±12%
Heat Transfer Coefficient, h	W/m^2K	±13%
Inlet Quality, X_{in}	-dim-	±23%
System Energy Balance		Within 10%

Chapter 4:
The Effect of DC Applied Voltage

This chapter outlines the effect of DC applied voltage on the convective boiling of R134a in a horizontal, counter-current heat exchanger. The pre-EHD flow conditions are such that a stratified wavy flow pattern with the liquid interface below and close to the electrode, exists i.e. Mass flux = 60 kg/m^{2}s, Applied heat flux = -9 kW/m^2, Average vapour quality = 40% with a 10% differential between inlet and outlet. This flow pattern was chosen as it was shown induce a high interfacial force by previous researchers (Sadek, 2009), (Ng, 2010) and from a quasi-static electric field analysis using Comsol™. Additionally, a stratified wavy flow pattern before the application of EHD can be used to develop a phenomenological approach to how each of the phases migrate, i.e. the flow redistribution due to EHD, and to subsequently analyse this effect of phase migration on heat transfer and pressure drop.

4.1 The Effect of EHD on Flow Patterns

Many researchers have shown that EHD induces flow pattern redistribution and can result in interesting flow patterns, specific to this phenomenon only i.e. twisted liquid cones and columns. (Yabe, et al., 1992), (Cotton, et al., 2005), (Ng, 2010). The research carried out here utilised a short, 30 cm test section which allowed for a constant flow pattern to be maintained along the axial length of the test section. Few researchers of EHD have been able to do this. (Salehi, et al., 1997), (Bryan & Seyed-Yagoobi, 2001) for evaporation and (Sadek, 2009), (Ng, 2010) for condensation. The heat transfer coefficient and the pressure drop are the parameters that are used to evaluate the performance enhancement due to EHD. As heat transfer and pressure drop are dependent on flow pattern, it is important to maintain a consistent flow pattern along the axial length of the test section to gain true insight into the effect of EHD. Figure 4.1 shows the test data range on the EHD annular flow pattern map developed by Cotton et al., 2005. It shows that without EHD the test data remains within the stratified wavy flow regime and upon application of 8kVDC EHD the test data lies on the stratified wavy – annular flow regime transition line.

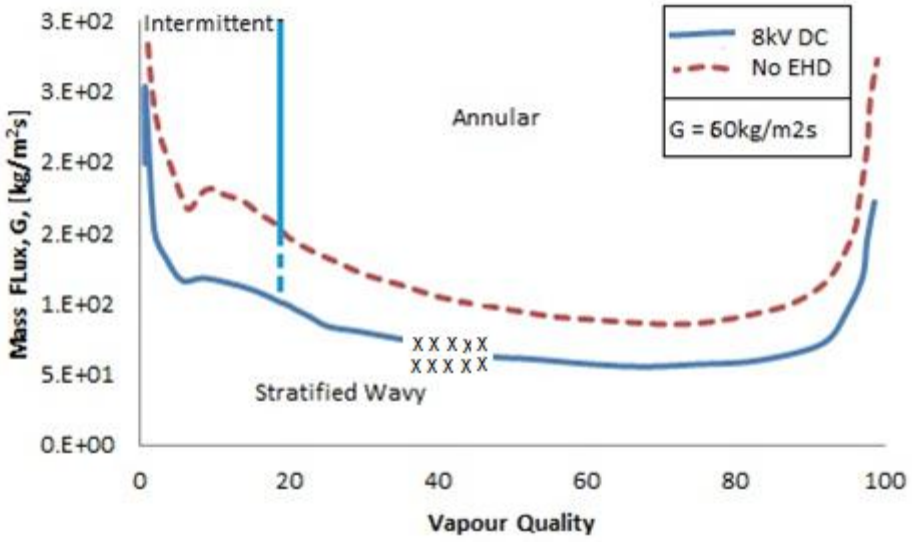

Figure 4.1: Test Data Locations on the Cotton et al., 2005, Annular R134a Convective Boiling Flow Pattern Map

Figures 4.2 and 4.3 show the high speed images taken of the transient behaviour seen upon application of EHD. In addition to flow visualisation, a simplified, quasi-static electric field analysis was completed using Comsol to gain further insight into the phase migration due to EHD. The electric field in Figure 4.2a is calculated for our stratified wavy flow conditions which correspond to a void fraction of $\alpha = 0.164$. Figures 4.2b-d assume each new quasi-steady flow distribution as the liquid is extracted toward the electrode based on that seen using the flow visualisation while maintaining this constant void fraction. The electric field ranges from $8x10^4$ to $3.3x10^6$ V/m with the darker areas indicating areas with higher electric field distribution. From Figure 4.2a we see that the electric field is strongest at the bottom of the electrode and thus, the EHD induced interfacial force is highest at the midpoint of the interface. This causes the liquid to be extracted in the direction of the charged electrode. The flow visualisation in Figure 4.2a supports this.

The EHD induced interfacial force increases with decreasing electrode – liquid gap distance and with increasing applied voltage. As the liquid is extracted toward the electrode, the gap distance decreases thereby increasing the electric field strength in this region and as a result, the interfacial force as seen in Figure 4.2b. This causes the liquid being extracted to accelerate toward the electrode and if the applied voltage is high enough, e.g. 4kV DC for our flow parameters, the liquid will touch the electrode surface as seen in the flow visualisation in Figure 4.2c.

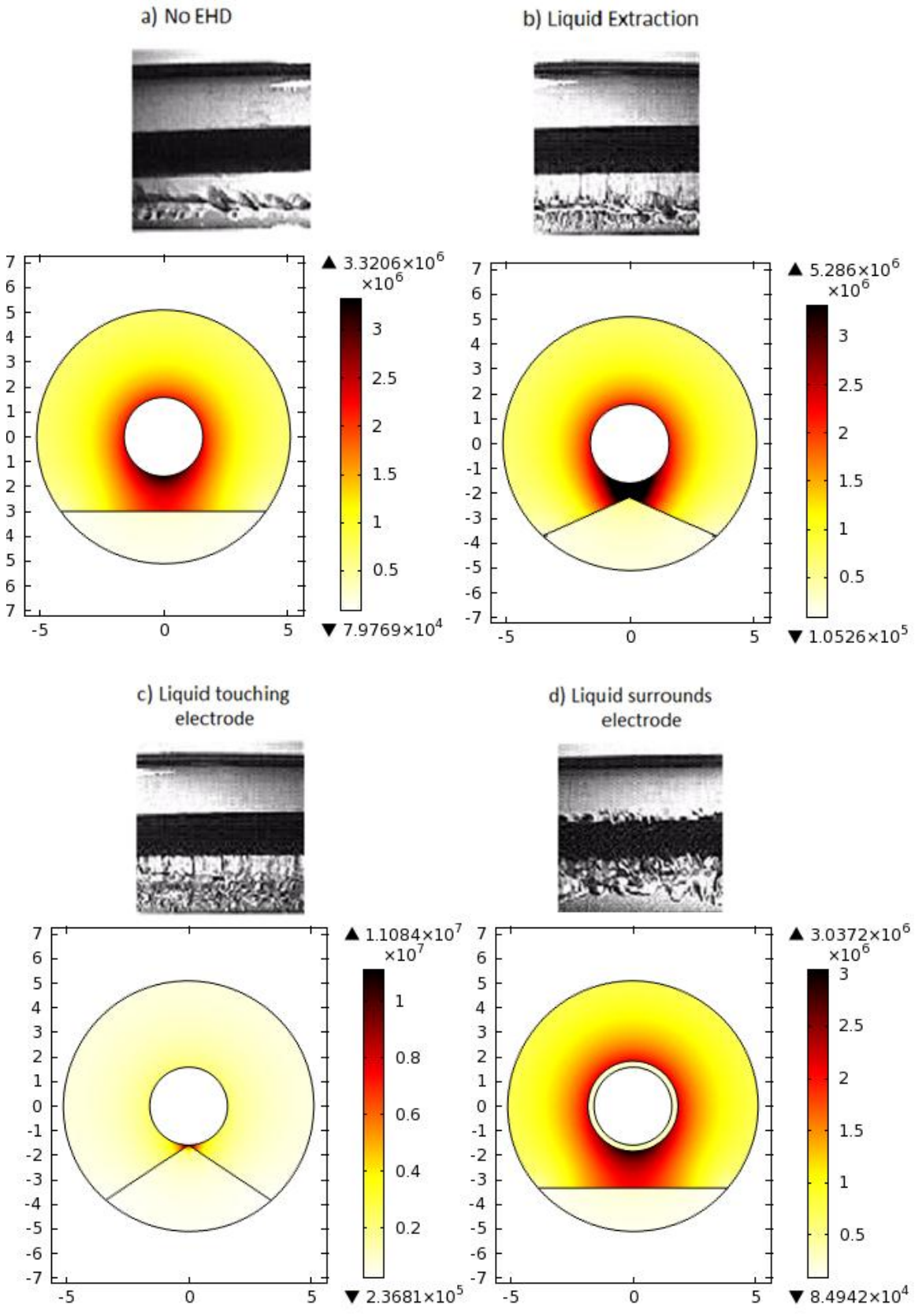

Figure 4.2: Application of 4kV DC Voltage: Flow Visualisation and Simplified, Approximated Electric Field Analysis. G = 60kg/m^{2}s, q" = -8.5kW/m^2, Xav = 40%, α = 0.164. NOTE: Different Scales

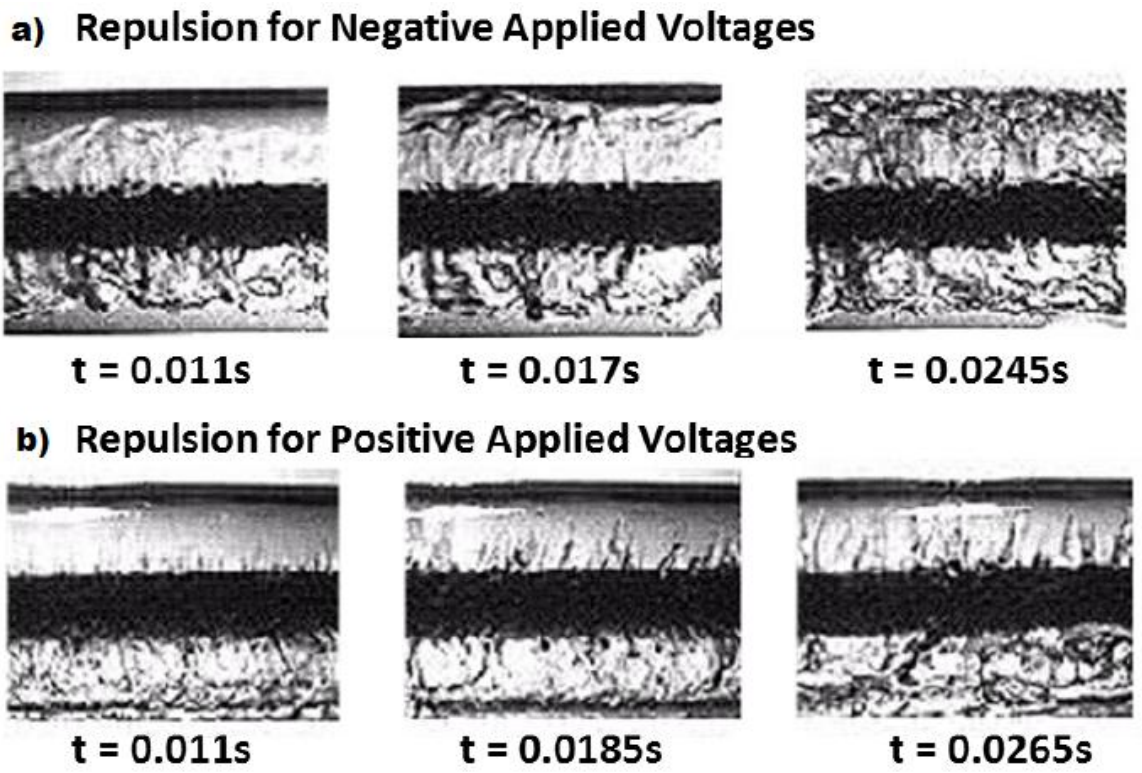

Figure 4.3: Liquid Repulsion Flow Visualisation: Application of -8kVDC (Top) +8kVDC (Bottom) G = 60kg/m^{2}s, q" = -8.5kW/m^2, Xav = 40%

The electric field distribution changes when the liquid level reaches the electrode surface. The region of highest electric field as seen in Figure 4.2c, is now at the electrode, either side of the liquid region. Therefore the liquid tends to be pulled around the electrode surface due to the polarisation forces at the interface and this is possibly partially aided by surface tension effects. The liquid continues to migrate around the electrode following the transition of the highest electric field region. The flow visualisation in Figure 4.2d shows the liquid fully surrounding the electrode.

The Comsol analysis in Figure 4.2d shows the case where the liquid has fully surrounded the electrode. Now the strongest electric field region occurs at the liquid vapour interface that is now offset from the electrode surface. The induced polarisation force arising from this configuration causes the liquid to experience a force that repels it from the electrode. From the flow visualisation in Figure 4.3 we see that liquid is expelled from the electrode at this point. However, the mechanism of liquid repulsion is different for positive and negative applied voltages as can be seen in the flow visualisation in Figure 4.3. This was also seen in research conducted by Ng, 2011, who saw twisted liquid cone structures for the positive repulsion case and twisted liquid column structures for the negative repulsion case.

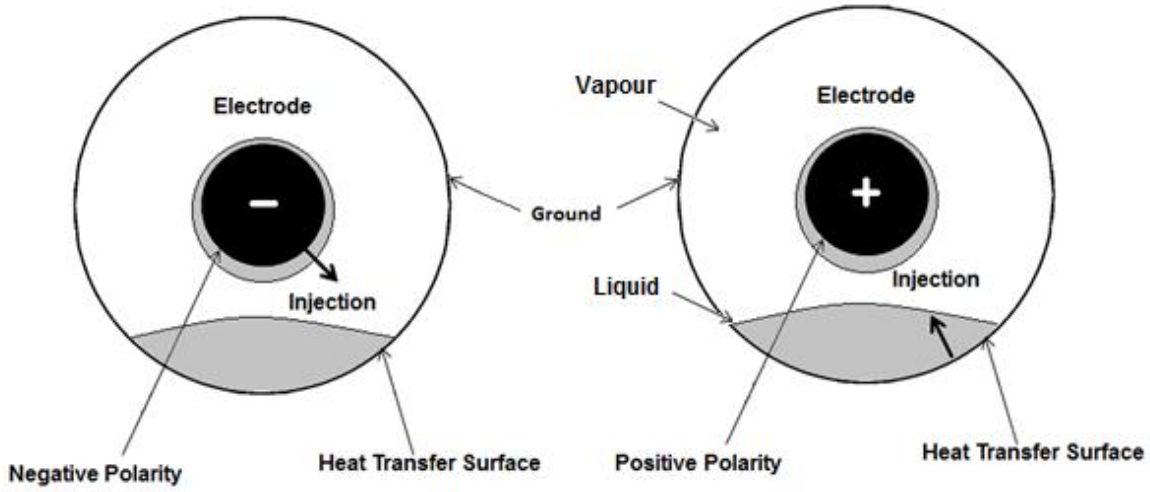

Figure 4.4: Mechanism of Charge Injection (Mobility Model)

It is suggested that it is the Coulomb or electrophoretic force, $\rho_{ei}E$, that contributes the most to the difference in repulsion between positive and negative applied voltage. It is the only component in the EHD body force where polarity has an effect since the other two terms in the EHD force are dependent on the square of the electric field. In the case of negative applied voltage, the Coulomb force aids the repulsion force whereas in the case of positive applied voltage, the Coulomb force acts against the repulsion force. The following hypothesis is proposed based on our knowledge of charge injection and liquid extraction: For the case of a negative applied voltage, when the liquid surrounds the electrode it becomes negatively charged and there is also charge injection from the negative electrode into this region. This causes the liquid to be repelled from the electrode. The

wavy flow on the bottom electrode is not charged, unless there is a gap bridged between this and the liquid surrounding the electrode. This liquid will undergo extraction as normal and will be further repelled upon reaching the electrode. For the case of a positive polarity, the liquid surrounding the electrode is positively charged and will therefore be repelled from the electrode. However charge injection of negative ions occurs from the outer tube into the wavy flow underneath the electrode. This liquid will be highly attracted toward the positive electrode both due to polarization and Coulomb forces. When this liquid is extracted and surrounds the electrode it acts against the repulsion force until charged. Since extraction and surrounding is a continuous process, the result is an inverted annular flow with some conical regions of liquid repulsion.

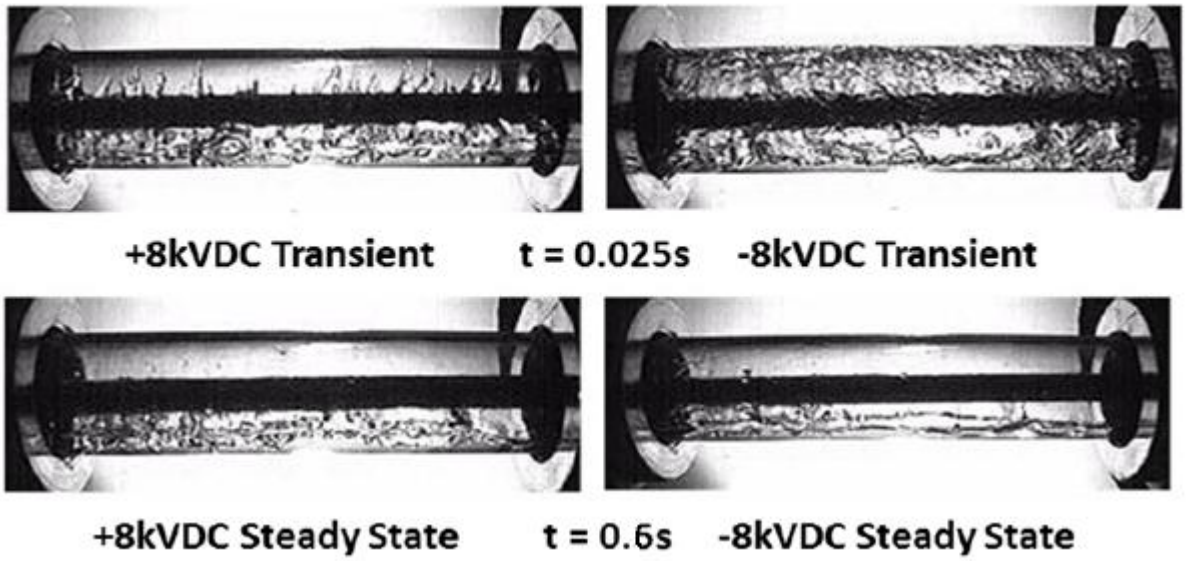

Figure 4.5: Transient and Steady State EHD Patterns, G = 60kg/m^{2}s, q" = -8.5kW/m^2, Xav = 40%

Figures 4.2 and 4.3 are transient flow patterns that occur milliseconds after the application of high voltage. After approximately 520 ms the electrophoretic and polarisation forces balance out and a steady state will exist. (Ng, 2010). Steady state flow patterns are less vigorous than the transient flow patterns but the differences in liquid repulsion mechanisms for opposing polarities still exist as seen in Figure 4.5. For the positive case, we see the twisted liquid cone structures very clearly whereas they are less well defined in the steady state case. In addition, more liquid droplets are present in the steady state case rather than large scale conical structures. In the negative polarity case we see repulsion in the transient case whereas there is some wetting of the upper surface in the steady state case but overall less liquid is repelled. The transient flow patterns provide insight into the phenomenon of EHD but the steady state data is used for all heat transfer and pressure drop readings.

4.2 The Effect of EHD on Convective Boiling Heat Transfer and Pressure Drop

Figures 4.6 and 4.7 show the results for varying DC applied voltage level on heat transfer and pressure drop for convective boiling respectively. As the applied voltage increases, the induced electric field increases in strength and this has been shown to increased mixing and redistribute the flow. This bulk mixing of the phases and phase migration can improve the heat transfer characteristics and increases the pressure drop and has been shown to varying degrees by numerous researchers. See Table 2.2. The trend of

increasing voltage resulting in increasing pressure drop and higher heat transfer coefficient can be seen clearly in Figure 4.6 and 4.7.

It is apparent from Figure 4.6 that the enhancement of heat transfer is much greater for the negative voltages than it is for the positive voltages. This is something that has not been very apparent in previous EHD convective boiling studies (Singh, et al., 1995), (Salehi, et al., 1997), (Cotton, 2000) or (Bryan & Seyed-Yagoobi, 2001). Previous work in single phase studies (Fujino, et al., 1989), (Ng, 2010) indicate a that there is an effect of polarity and that it is mainly due to the differing charge injection mechanisms and the resulting electrophoretic force for positive and negative electrodes as this is the only term that does not contain the square of the electric field and it is the dominant EHD force in single phase applications. In two phase flows, the electrophoretic force is outweighed by the dominant polarisation forces and therefore it may be harder to extract a polarity effect. It should be noted that (Ng, 2010) saw a slight difference in the effect of polarity for EHD convective condensation in a short test section with constant flow pattern along the length.

Figure 4.6 indicates that the heat transfer coefficient is higher for negative applied voltages. Ng, 2010, noted that the positive voltages resulted in higher heat transfer whereas here we see that the opposite is shown. It is hypothesised that heat transfer and pressure drop are primarily a function of flow pattern and that some flow patterns may be more favourable for different heat transfer mechanisms. The positive applied voltage attracts more liquid into the core region drying the heat transfer surface. This is advantageous in condensation where you want to condense fluid onto the heat transfer surface but less efficient in boiling as the portions of the heat transfer surface may be dry. The opposite is true for the case of negative applied voltage where more liquid is repelled toward the heat transfer surface. This is suitable for boiling as it rewets the heat transfer surface, whereas it interferes with the ease of formation of droplets in the case of condensation. Some condensation experiments at the same flow parameters were conducted for comparison purposes and also for validation of the rig. These results and the comparison are given in Appendix E.

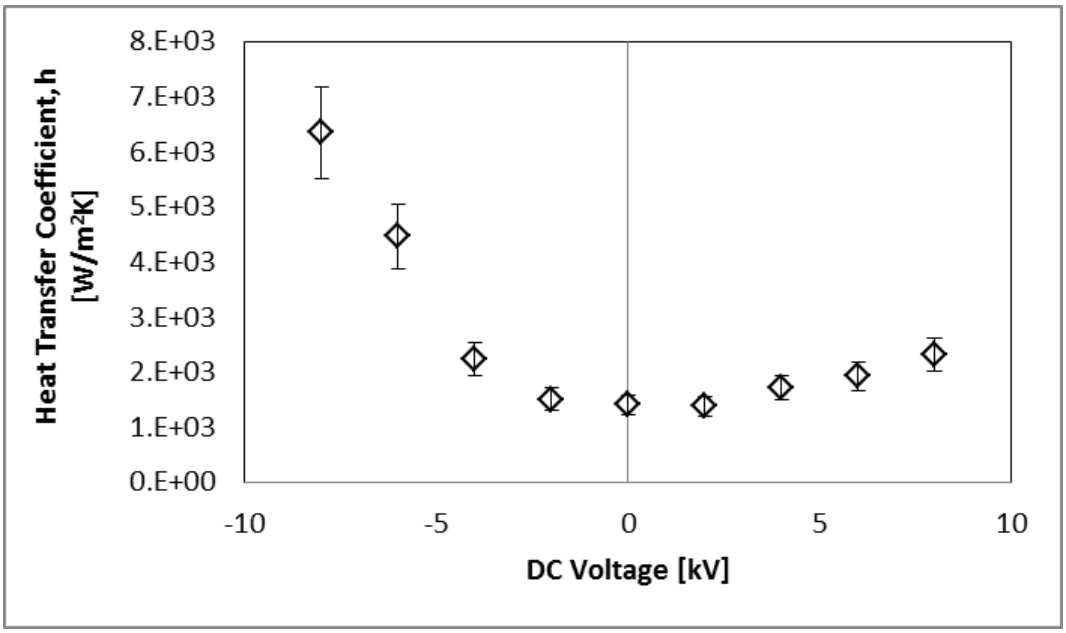

Figure 4.6: The Effect of DC Applied Voltage on Convective Boiling Heat Transfer
G = 60kg/m^{2}s, q" = -8.5kW/m^2, Xav = 40%

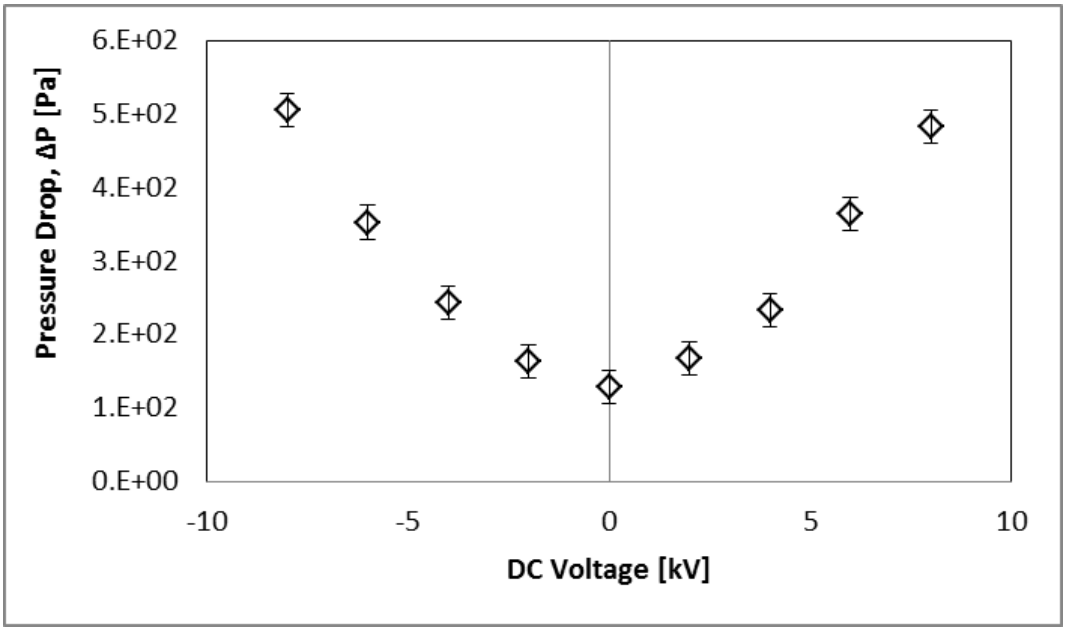

Figure 4.7: The Effect of DC Applied Voltage on Convective Boiling Pressure Drop
G = 60kg/m^{2}s, q" = -8.5kW/m^2, Xav = 40%

In Figure 4.7, we see that although there is a slightly increased pressure drop for negative voltages compared to positive applied voltages, the difference is not as pronounced as it is in the heat transfer results in Figure 4.6 which is likely explained by the different components contributing to the system pressure drop and their magnitudes. There is the system pressure drop that is composed of the frictional pressure drop due to flow along the heat transfer surface, the electrode and over the spacers. Another component of this pressure drop term is the flow acceleration due to heat transfer occurring along the tube length. This combined system pressure drop is the most dominant pressure drop component in the test section. There is also a pressure drop associated with EHD flow redistribution. Different flow patterns have varying proportions of liquid and vapour in contact with the solid resulting in different frictional components of the pressure drop. The new flow structures will have different interfacial area and this can also contribute to the pressure drop as well as the additional acceleration component that can be caused by intermittent type flow patterns. An example of the variation of pressure drop with flow pattern can be seen in Figure 2.16. From this graph we see that there can be a 4-5 fold increase in pressure upon transition from stratified to annular or intermittent flow.

When high voltages are applied, there will be significant disturbance of both the thermal and liquid hydrodynamic boundary layers in the system due to the large gradient of permittivity in these regions. Figure 4.8 shows the location of these boundary layers, magnified for clarity. The heat transfer surface is the outer tube so this will produce a circumferential thermal and hydrodynamic boundary layer, whereas the electrode only has a hydrodynamic boundary layer due to the flow travelling across it. Disturbance of the thermal boundary layer can enhance heat transfer and disturbance of hydrodynamic boundary layer can cause additional pressure drop. When EHD is applied the liquid phase, which is the phase that contributes most to the pressure drop, migrates either to the wall regions; for negative applied voltages, more to the heat transfer surface and for positive applied voltages, more to the electrode surface. Since both of these surfaces have hydrodynamic boundary layers, the pressure drop due to this EHD induced flow redistribution is quite similar. It will not be the same for the heat transfer coefficient because only one surface is a heat transfer surface. This is one potential explanation for why the pressure drop does not vary with polarity as much as the heat transfer coefficient does.

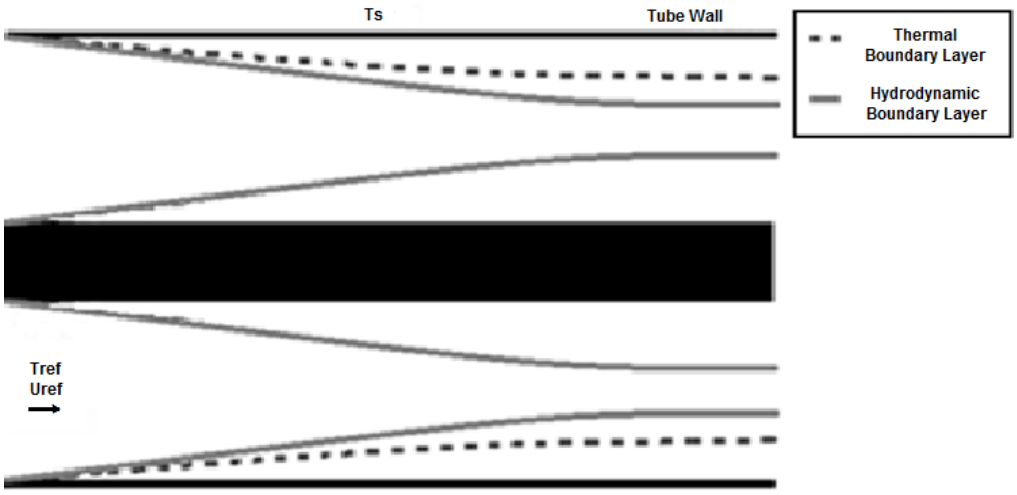

Figure 4.8: Exaggerated Sketch of the Hydrodynamic and Thermal Boundary Layers

The flow redistribution due to EHD can be seen via flow visualisation and also by analysing the test section surface temperatures, Figure 4.9, and their associated standard deviations, Figure 4.10, along the test section. Higher surface temperatures tend to be associated with vapour in contact with the surface whereas lower temperatures tend to be associated with liquid in contact with the heat transfer surface. Additionally, the standard deviation can indicate whether the flow pattern is continuous or intermittent.

For the no EHD case in Figure 4.9a the bottom surface temperature is at approximately 28 ^{0}C, indicating liquid flowing along the bottom of the tube and the top surface temperature is at 34 ^{0}C, indicating vapour flowing along the top surface of the tube. Both of these profiles have low standard deviation, approximately 0.06 ^{0}C, whereas the side temperatures are varying between 28 ^{0}C and 34 ^{0}C indicating intermittent wetting of the side walls. This implies that the flow pattern is stratified wavy. The flow visualisation in Figure 4.11a confirms that the flow pattern is stratified wavy. The local heat transfer coefficient for the top surface is approximately 1000 W/m^{2}K whereas it is double that for the bottom surface indicating a marked difference in the mechanism of heat transfer. The top surface is essentially convection in a vapour flow and the bottom is convection in a liquid flow, hence the reason why the bottom heat transfer coefficient is higher.

In the +4kV temperature profiles, Figure 4.9b, we see that the bottom surface temperature is lower than in the zero field case. This suggests a thinner liquid film on the bottom surface which improves the boiling rate due to the lower liquid thermal resistance. The other thermocouple profiles have not varied much compared to the no EHD case,

therefore it is likely that the liquid removed from the bottom surface has moved into the core region around the electrode. This inverted annular flow pattern is confirmed via flow visualisation in Figure 4.11. More insight into this flow pattern is found by looking at the local heat transfer coefficients, approximately 1400 W/m^2K for the top surface and 3500 W/m^2K for the bottom surface. Both coefficients are increased from the no EHD case. The heat transfer on the bottom surface is improved due to the thinner liquid layer on the surface that is easier to evaporate. The top surface heat transfer is greater due to the increased liquid uptake into the top portion of the tube which results in improved evaporation compared to pure vapour flow.

In the -4kV temperature profiles, Figure 4.9c, we see again a lowering of the bottom surface temperature compared with the zero field case. This is due to liquid uptake into the core region. It is also indicated from this figure and the high standard deviation Figure 4.10c that the top surface is being intermittently wetted most likely by the liquid in the core region that is being repelled from the electrode. The profiles suggest a slug type/intermittent flow pattern which is confirmed in the flow visualisation in Figure 4.11c. The heat transfer coefficient on the top surface is slightly improved over the positive 4kVDC case, 1550 W/m^2K, as more liquid is repelled toward the top of the tube with this polarity. The heat transfer coefficient on the bottom surface for this case is in the range of 3600 W/m^2K – a slight improvement over the +4kV case due to this additional mixing in the bottom portion of the tube as a result of this intermittent flow pattern.

In Figure 4.9d, it can be seen that the 8kV cases induces more redistribution than the 4kV cases as the bottom surface temperature is lower, approximately 27 ^oC for this case indicating further liquid uptake into the core due to the higher interfacial forces induced by this higher applied voltage. In addition to this there is some intermittent wetting of the top surface, as can be seen at location 2 in Figure 4.9d. This intermittent wetting is less that as seen in the -4kV case. The profiles suggest an inverted annular flow pattern as was seen in the +4kVDC case except with more uptake into the core region for this higher voltage. The flow visualisation data in Figure 4.11d confirms that there is an annular flow around the electrode. Additionally there are liquid droplets suspended in the core region which presumably are impinging on the top surface of the tube and are responsible for the intermittent type flow pattern seen on the top surface at location 2 in Figure 4.9d.

In the -8kV case, Figure 4.9e, all of the surface temperatures have collapsed on each other centred at approximately 26 ^{o}C. This suggests that the entire circumference of the tube is wet, i.e. annular flow. The slight difference in temperature between each of the profiles is related to the liquid film thickness, and therefore thermal resistance, at each location. In general, the top and side temperatures are the closest, indicating a thinner film in these regions compared with the comparably thicker flow on the bottom of the tube. This makes sense as there will be a falling film in this region due to gravity. The -8kVDC case is quite similar in behaviour to the -4kVDC case except now the applied voltage is high enough to cause the liquid to be repelled fully toward the heat transfer surface resulting in an annular flow pattern rather than an intermittent flow pattern. This annular flow pattern is confirmed in the flow visualisation data in Figure 4.11e. There is a marked difference in the heat transfer coefficients for the positive and negative 8kVDC cases. The +8kVDC top heat transfer coefficient is approximately 1700 W/m^{2}K, which is almost double the no EHD top heat transfer coefficient. The bottom +8kVDC heat transfer coefficient is approximately 8000 W/m^{2}K, which is approximately a 4 fold increase compared to the no EHD case. The improvement is due to the change in flow pattern from a stratified wavy to an inverted annular flow pattern meaning a thinner fluid flow on the bottom of the tube which is significantly easier to evaporate. The enhancement is greater for the -8kVDC case, however. The top heat transfer coefficient for -8kV are in the range of 4500 W/m^{2}K, a 4 fold increase over the no EHD case. This high value of heat transfer coefficient is similar to that seen on the bottom surface for lower applied voltages, i.e. a convective heat transfer mechanism that is enhanced by EHD induced bulk mixing. The flow regime is annular for -8kVDC so there is significant wetting of the top surface. The bottom heat transfer coefficient for -8kVDC is in the range of 15,000 W/m^{2}K, a huge 7 fold enhancement over the no EHD case. It is likely that this high value is due to the much thinner liquid flow on the bottom surface coupled with the energetic nature of the flow pattern in this region.

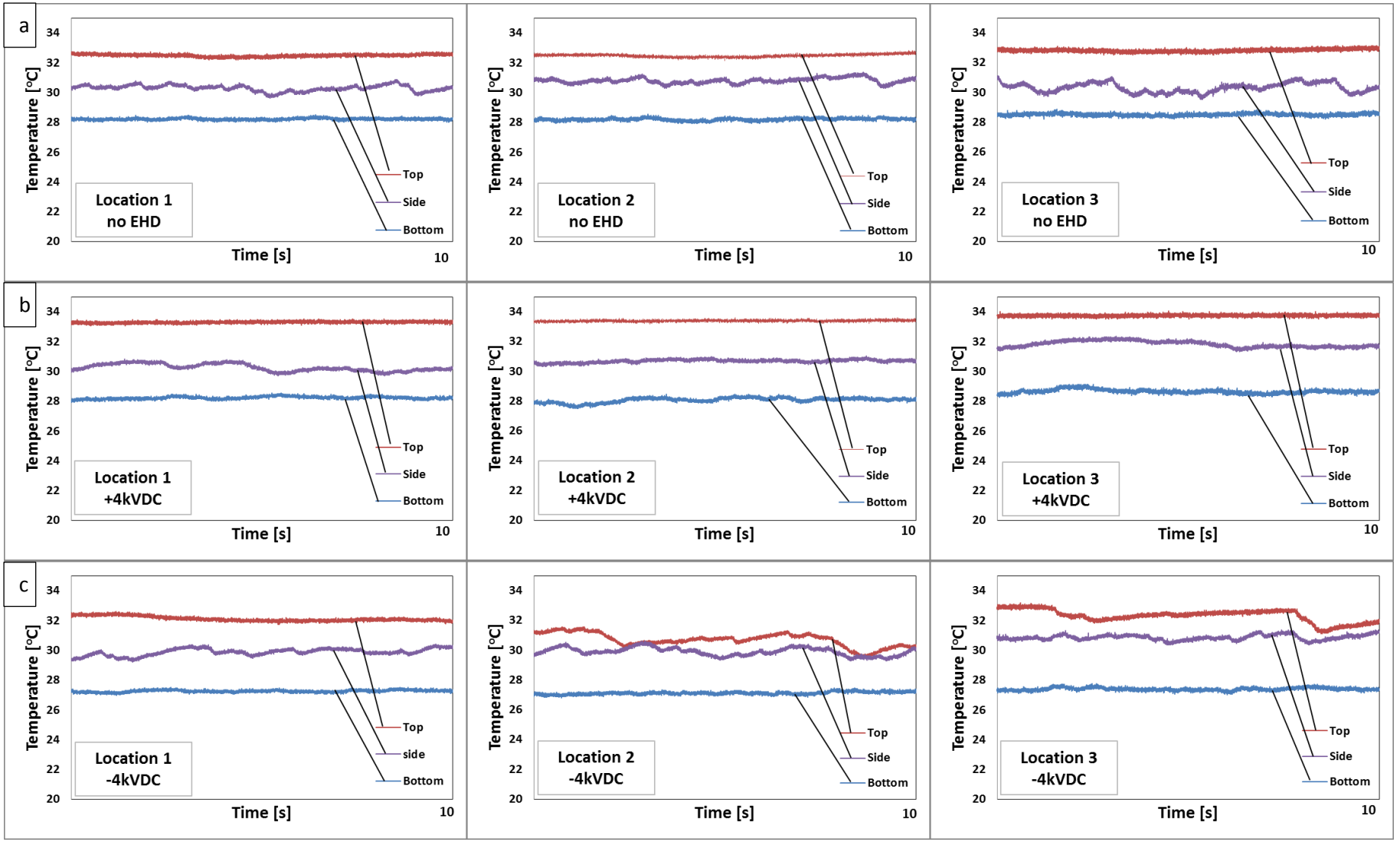

Figure 4.9(i): Convective Boiling Temporal Surface Temperature Profiles for Varying Applied DC Voltage, G = 60kg/m^{2}s, q" = -8.5kW/m^2, Xav = 40%

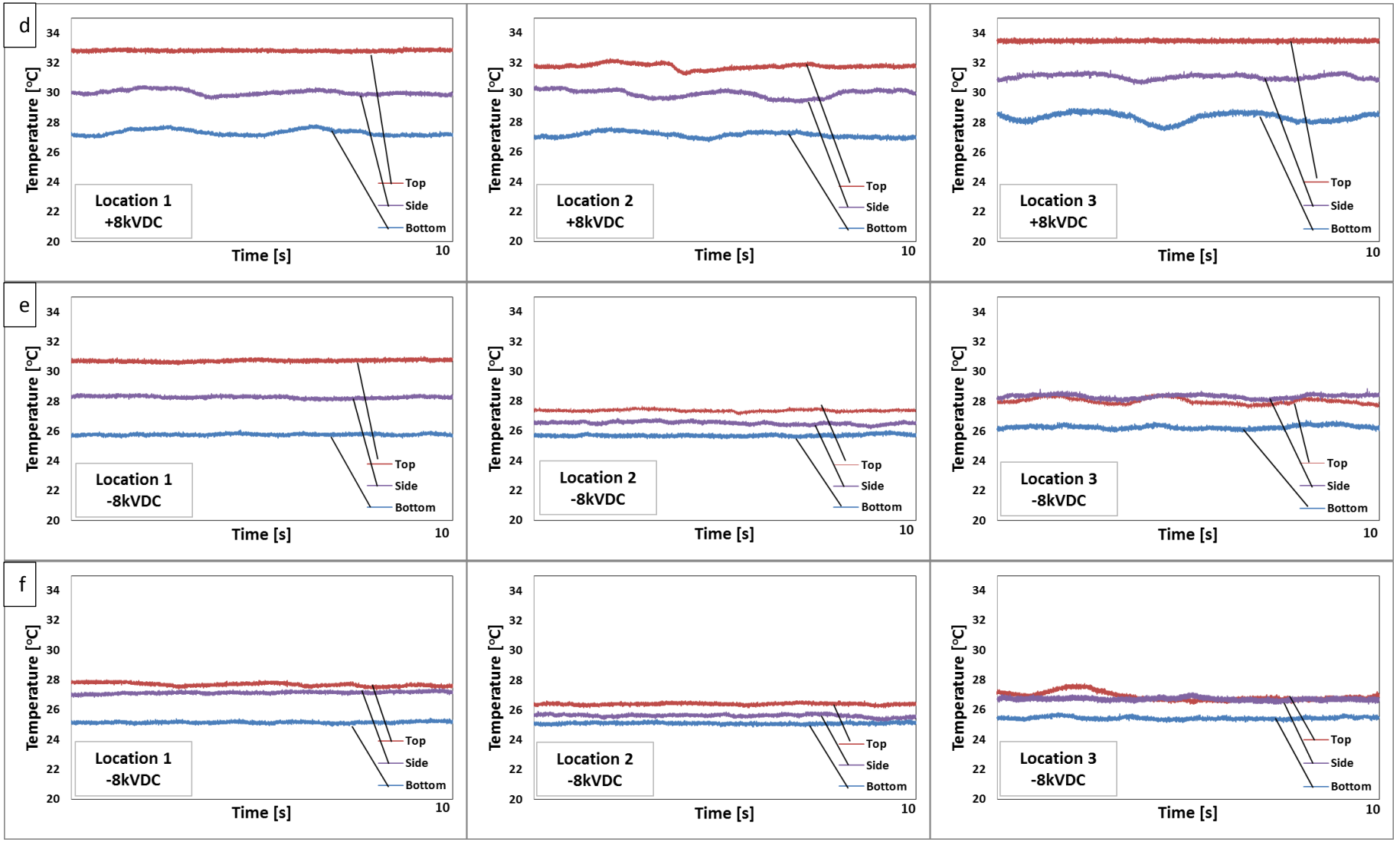

Figure 4.9 (ii): Convective Boiling Temporal Surface Temperature Profiles for Varying Applied DC Voltage, G = 60kg/m^{2}s, q" = -8.5kW/m^2, Xav = 40%

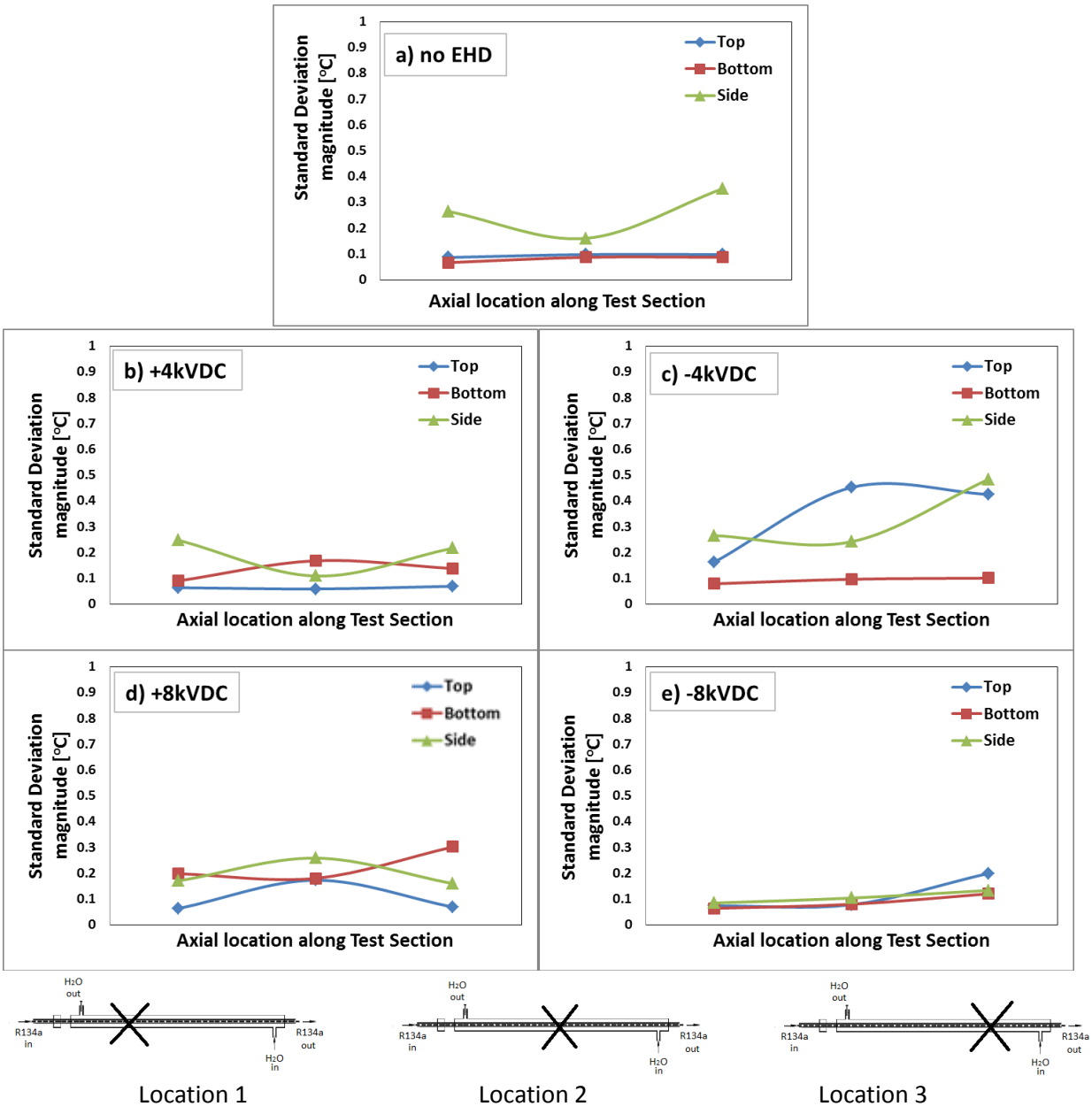

Figure 4.10: Convective Boiling Standard Deviations of Surface Temperatures for Varying Applied DC Voltage, G = 60kg/m^{2}s, q" = -8.5kW/m^2, Xav = 40%

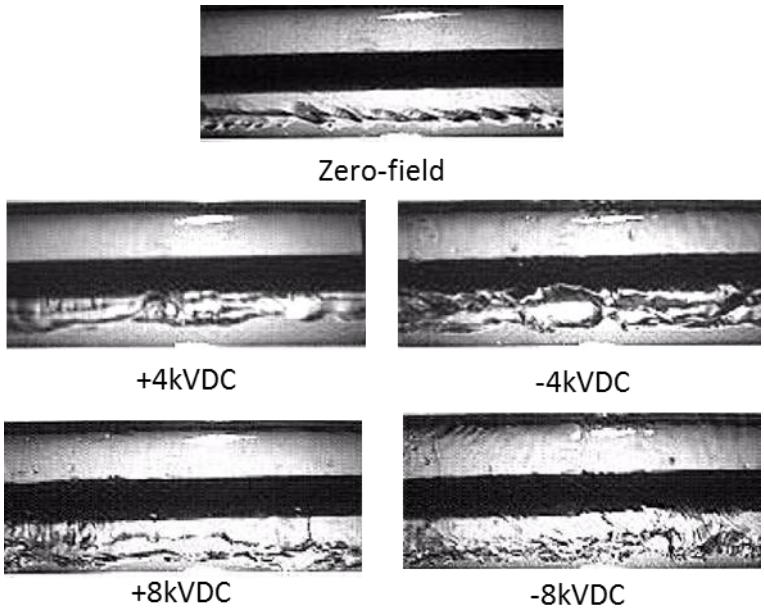

Figure 4.11: Effect of DC Voltage on Convective Boiling – Flow Visualisation
G = 60kg/m^{2}s, q" = -8.5kW/m^2, Xav = 40%

Figures 4.12 and 4.13 show the repeatability for these DC applied voltage experiments. It can be seen that the negative high DC voltage data varies the most. For the heat transfer coefficient data, some of this variability can be attributed to the uncertainty associated with the high heat transfer coefficients. However, after correlating the data points with the EHD flow pattern map developed by Cotton et al., 2005, it was hypothesised that the main contribution to the poor repeatability in this region is due to these data points coinciding with a flow pattern transition region. Figure 4.14 shows this map and the associated test points' locations on the map. It must be noted that this EHD flow pattern transition line is for a positive 8kV case and that the boundary for the negative 8kV is likely to be lower due to the fact that negative voltages induce higher heat transfer enhancement. From the repeatability graphs it appears that points; b, c and d are the furthest from the perceived trend and these points appear closest to the transition boundary. Figure 4.9e and Figure 4.9f show the surface temperature profiles, i.e. the flow pattern for points a and c respectively on Figure 4.12. The variance in the -8kV data in Figure 4.9f is due to the flow pattern not being consistently annular along the axial length of the test section. In fact it is on the annular/intermittent flow pattern transition. At this transition region, small variations in quality and saturation temperature affect the liquid level height which influences the interfacial term such that it is sometimes strong enough to cause fully annular flow but other times it will remain intermittent/annular.

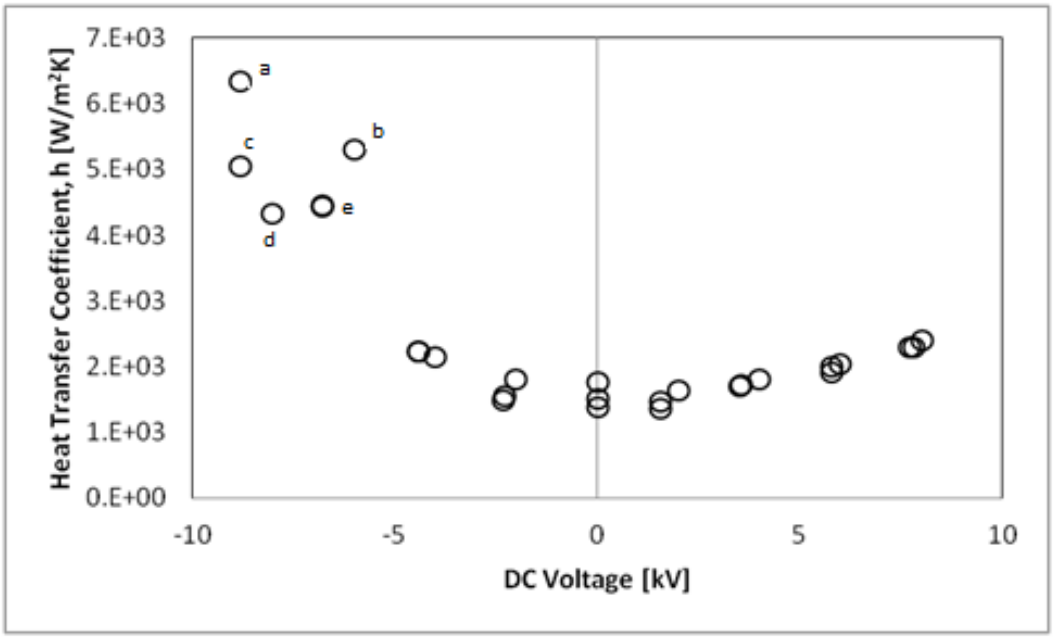

Figure 4.12: Repeatability of DC Voltage Effects on Convective Boiling Heat Transfer, G = 60kg/m^{2}s, q" = -8.5kW/m^2, Xav = 40%

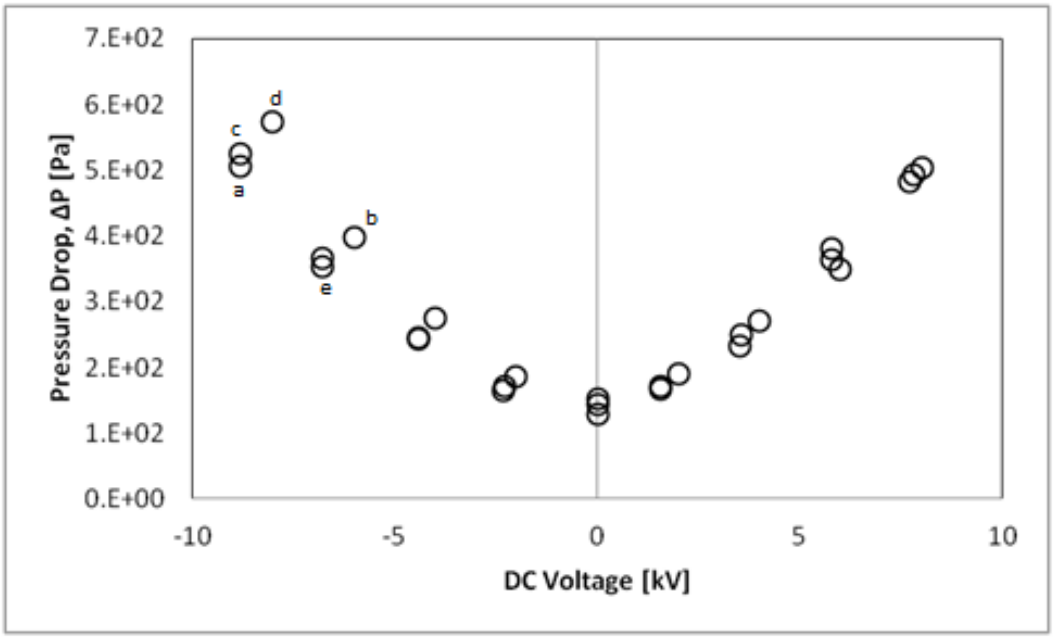

Figure 4.13: Repeatability of DC Voltage Effects on Convective Boiling Pressure Drop, G = 60kg/m^{2}s, q" = -8.5kW/m^2, Xav = 40%

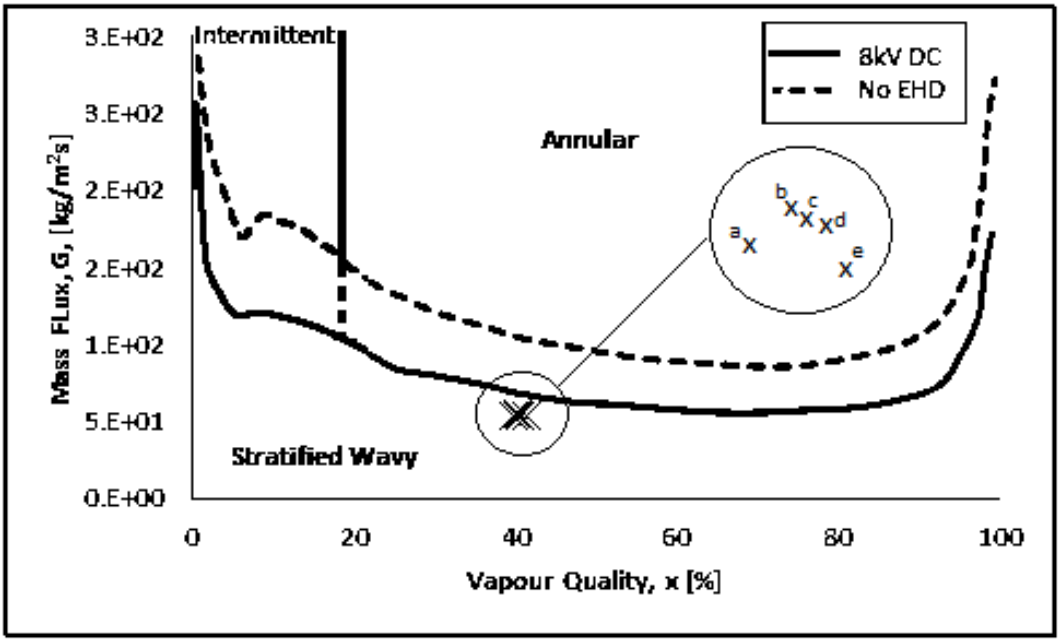

Figure 4.14: Repeatability of DC Voltage Effects on Convective Boiling – Flow Pattern Map

4.3 Chapter Summary

This chapter focuses on the effect of DC voltage on flow redistribution and ultimately heat transfer and pressure drop on convective boiling that has an initial zero field stratified wavy flow pattern. It was found that increasing the voltage increases the interfacial force extracting the liquid into the core region. Depending on the applied voltage and polarity, annular, inverted annular and intermittent flow patterns transitions were induced, each of which have differing heat transfer and pressure drop characteristics. A general trend of improved heat transfer with increasing voltage was found. However, the pressure drop penalty increases in the same manner.

It was found that polarity influences the flow distribution. For both polarities, the liquid is extracted toward the electrode due to the polarization forces acting at the liquid vapour interface. The flow then surrounds the electrode via liquid extraction as the liquid, which has a high dielectric constant, is attracted to the region of high electric field. Once the fluid surrounds the electrode, the liquid will be repelled due to the polarization forces arising from the now inverted electric field distribution. The electrophoretic force aids this repulsion for negative voltages and opposes this force for positive voltages, generating new flow distributions which were seen via flow visualization and surface temperature profiles. A liquid film on the heat transfer surface improves boiling heat transfer and removal of this

film improves condensation heat transfer. Using this knowledge we were able to show negative voltages are more suitable to evaporation heat transfer and that positive voltages are more suited to condensation heat transfer for this electrode configuration.

Chapter 5:
The Effect of Pulse Waveforms & Control

Chapter 4 discussed the effect of DC waveforms on flow redistribution. The amplitude and polarity of a DC can be controlled. However, pulse waveforms can provide more variable control compared to DC waveforms as the frequency, the pulse width and the EHD 'on-time' can be varied in addition to amplitude and polarity. Consequently, pulse waveforms can be used to generate new flow patterns that will have different heat transfer and pressure drop characteristics. This has been shown for a similar convective boiling system to the one used in this study with a longer test section by (Cotton, 2000) and for a short test section in convective condensation studies by (Sadek, et al., 2011) and (Ng, et al., 2011). In this thesis, a short test section is used to investigate the effect of these pulse parameters on convective boiling.

This chapter aims to investigate the range of controllability achievable for our given flow parameters by varying pulse waveform parameters. As presented in Chapter 4, the pre-EHD flow conditions are such that a stratified wavy flow pattern with the liquid interface below and close to the electrode, exists i.e. Mass flux = 60 kg/m^{2}s, Applied heat flux = -9 kW/m^2, Average vapour quality = 40% with a 10% differential between inlet and outlet. The chapter concludes with the proof of concept that EHD can be used for load control and compares this method of control to one of the more conventional control methodologies; changing flow rate.

5.1 The Effect of Varying Pulse Parameters

Figure 3.4 outlines the key waveform parameters associated with pulse signals. The following parameters were tested to study their importance on the flow redistribution in a similar manner to Sadek et al., 2011; DC level, peak-to-peak voltage, frequency, duty cycle and polarity. Table 5.1 summarises the ranges tested for each of these parameters. Further details on each of the tests conducted can be found in the test matrix in Appendix B1. The effect of sine waves, with corresponding properties to 50% duty cycle pulse waveforms, was also studied. As observed by Sadek et al., 2011, the trends seen for the sine wave data were

similar to the corresponding square wave. Hence, this chapter will focus only on the pulse waveform results. It should be noted that the enhancement associated with sine waves is slightly lower than for the pulse waveform, most likely due to the fact that the peak voltage is reached for a shorter length of time than the corresponding pulse wave i.e. the RMS voltage is lower by a factor of $\sqrt{2}$.

Table 5.1 Electric Field Parameters

Parameter		DC Signal	Pulse Wave	Sine Wave
DC Amplitude	[kV]	-8 to 8	-8 to 8	-8 to 8
DC Level	[kV]	-	-6 to 6	-6 to 6
Peak – Peak Voltage	[kV]	-	0 to 8	0 to 8
Frequency	[Hz]	-	2 to 2000	2 to 2000
Duty Cycle	[%]	-	0 to 100	-

5.1.1 The Effect of Frequency

The effect of frequency for a pulse wave, 50% duty cycle, zero DC Level for positive and negative 8kV amplitude was tested. These waveforms are shown in Figure 5.1. Figure 5.2 and 5.3 show the effect of these waveforms on heat transfer and pressure drop respectively. The negative polarity waveform induces higher enhancement, which follows the same trend as the DC results in chapter 4. The effect of polarity on the pressure drop results is less pronounced than the effect on heat transfer, however it is suggested here that the positive polarity induces slightly more pressure drop and this is more noticeable at higher frequencies.

An induced pulsing behaviour in the flow pattern i.e. pulsing of the transient behaviour seen upon application of EHD in chapter 4, can be seen particularly in the low frequency surface temperature profiles. This pulsing behaviour affects the wetting characteristics of the heat transfer surface and this will determine the thickness of the liquid film on the heat transfer surface, the thermal resistance and consequently the heat transfer coefficient. The liquid extraction time is also important as this will determine how much liquid will be expelled from the electrode every period. Sadek, 2009, tested the effect of frequency for the positive case in condensation and found that the effect of frequency had very little effect on the heat transfer but that pressure drop penalty was greatest at lower frequencies. From Figure 5.2 it is suggested that the peak enhancement occurs in the region of 100-200 Hz. This is higher than the peak found for condensation experiments, 1-10 Hz

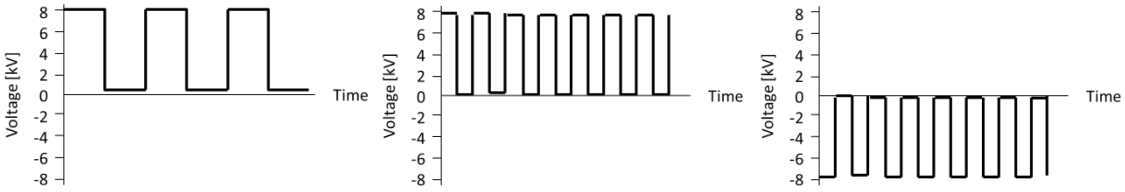

Figure 5.1: Frequency Waveforms, 50% Duty. 8kVDC Low Frequency (Left), 8kVDC High Frequency (Middle), -8kVDC High Frequency (right)

range, but that is not surprising as the optimum wetting characteristics for condensation are not the same as for boiling.

The surface temperature profiles and associated standard deviations Figure 5.4 – 5.6 can be used to estimate the flow pattern associated with each waveform and therefore, how each waveform affects the heat transfer and pressure drop.. For the positive voltage data, Figures 5.4a-c, it appears that the dominant flow regime is stratified wavy. The pulsing behaviour is clearly seen in the 2 Hz case, Figure 5.4a, and the associated standard deviation, Figure 5.5b, of the top and bottom surface temperatures has doubled compared to the no EHD case. The surface temperature wetting characteristics vary in accordance with the pulse frequency and this can change the thickness of the liquid film on the heat transfer surface and therefore the thermal resistance to boiling heat transfer.

The average heat transfer coefficient for the bottom surface decreases with increasing frequency; 4370 to 4010 W/m^2K between 2 Hz and 1 kHz. This surface temperature data suggests an inverted annular flow pattern for all frequencies for the positive voltage. However, the level of mixing induced by each frequency varies. This induced mixing in the bottom portion of the tube seems more effective at enhancing boiling heat transfer at lower frequencies possibly due to the EHD on-off time being sufficiently long to generator a full liquid extraction mechanism every cycle. However, the average heat transfer coefficient on the top surface increases with increasing frequency, the opposite to what occurs on the bottom surface. This is most likely due to increased liquid droplet impingement on the top surface which intermittently wets it, enhancing the evaporation on this portion of the tube. The high variation seen in the top surface temperatures, particularly for the 1 kHz case, Figure 5.5d, supports this assumption of droplet impingement. The optimum frequency for boiling heat transfer for the positive voltage is approximately 200 Hz striking a balance between the conflicting enhancement trends on the top and bottom surface.

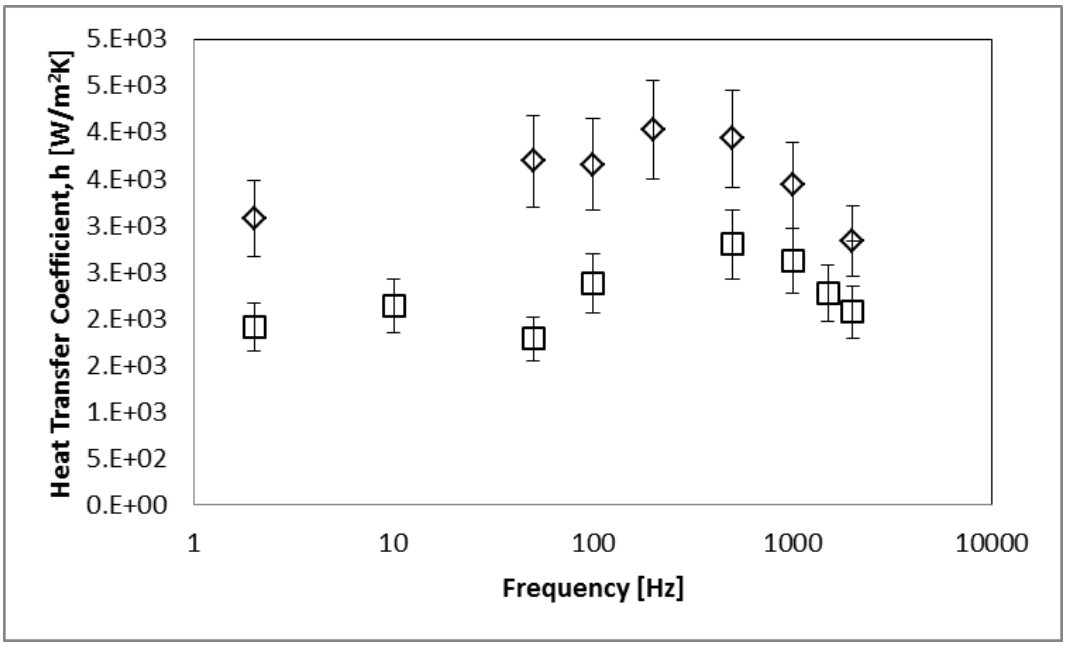

Figure 5.2: The Effect of Frequency on Convective Boiling Heat Transfer.
G = 60kg/m^{2}s, q" = -8.5kW/m^2, Xav = 40%, 50% duty, zero level □ +8kV ◊ -8kV

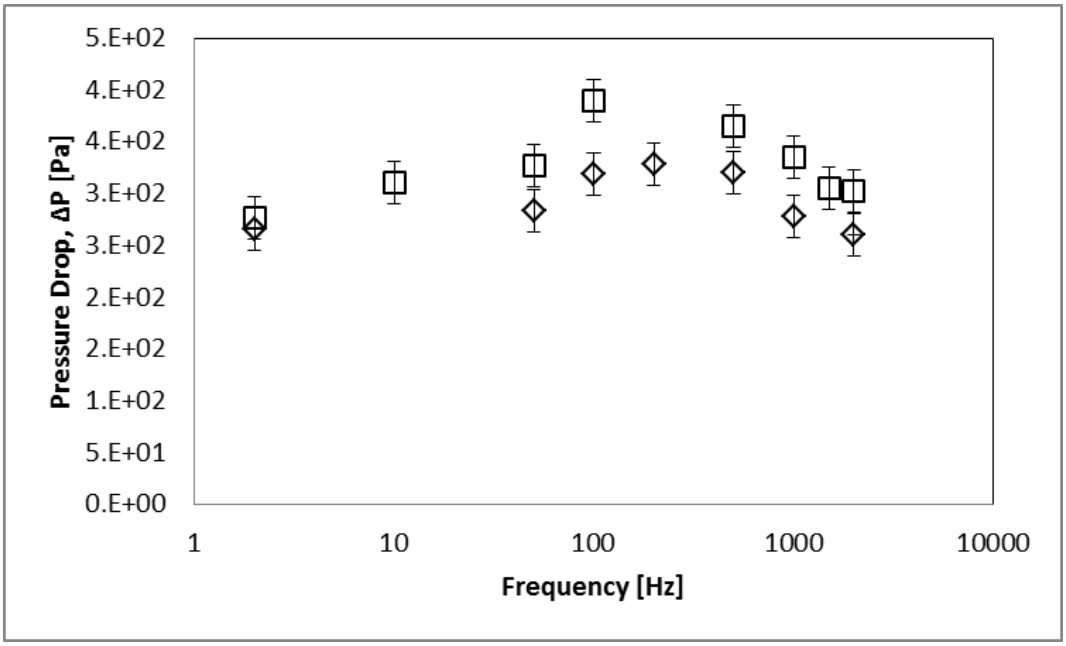

Figure 5.3: The Effect of Frequency on Convective Boiling Pressure Drop.
G = 60kg/m^{2}s, q" = -8.5kW/m^2, Xav = 40%, 50% duty, zero level □ +8kV ◊ -8kV

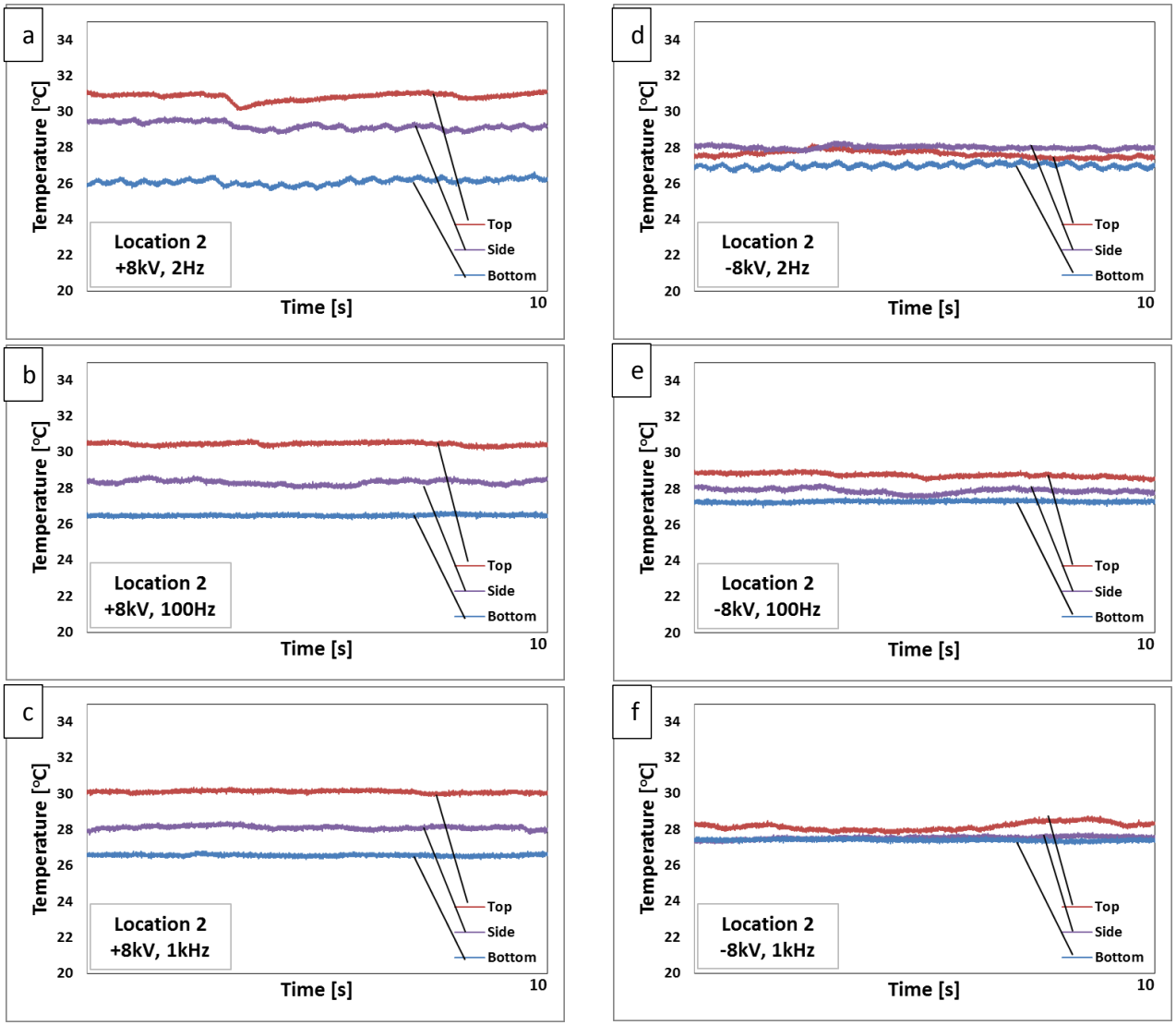

Figure 5.4: Convective Boiling Temporal Surface Temperature Profiles for the Effect of Frequency Surface Temperature Profiles, +8kV (left) -8kV ()right, G = 60kg/m^{2}s, q" = -8.5kW/m^2, Xav = 40%

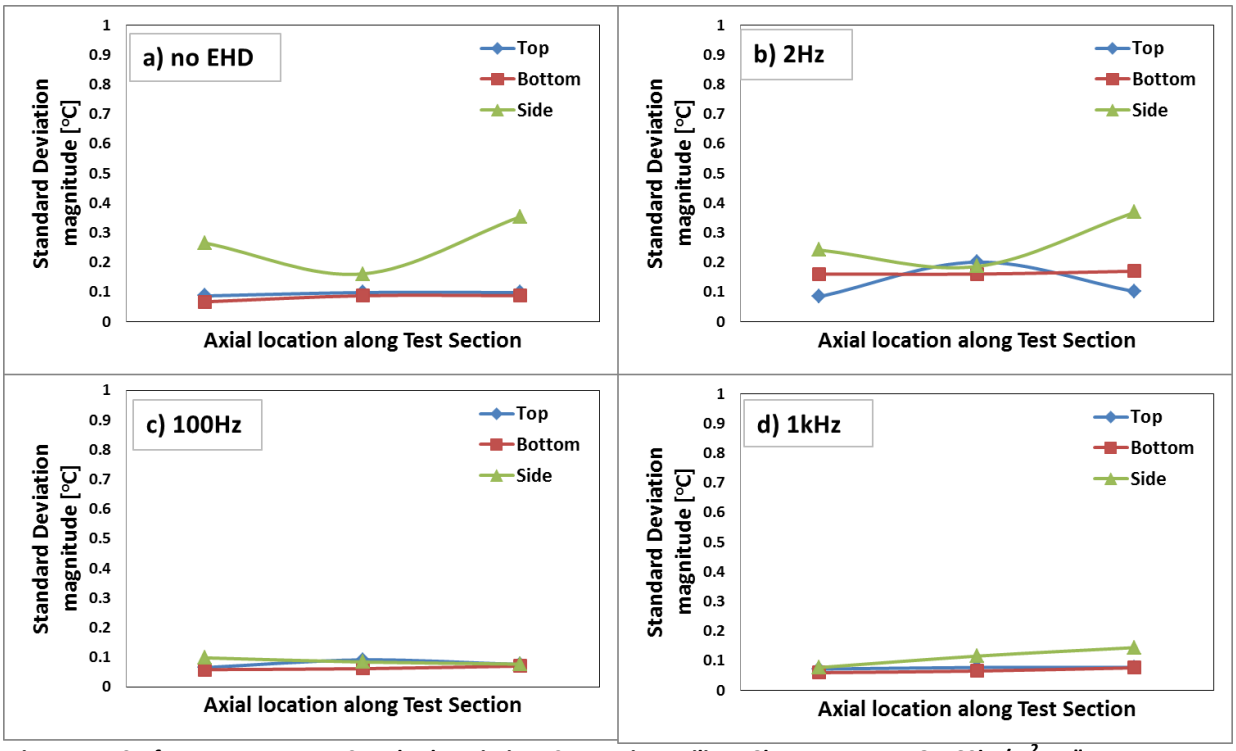

Figure 5.5: Surface Temperatures Standard Deviation: Convective Boiling +8kV Frequency. G = 60kg/m^{2}s, q" = -8.5kW/m^2, Xav = 40%, zero level, 50% duty

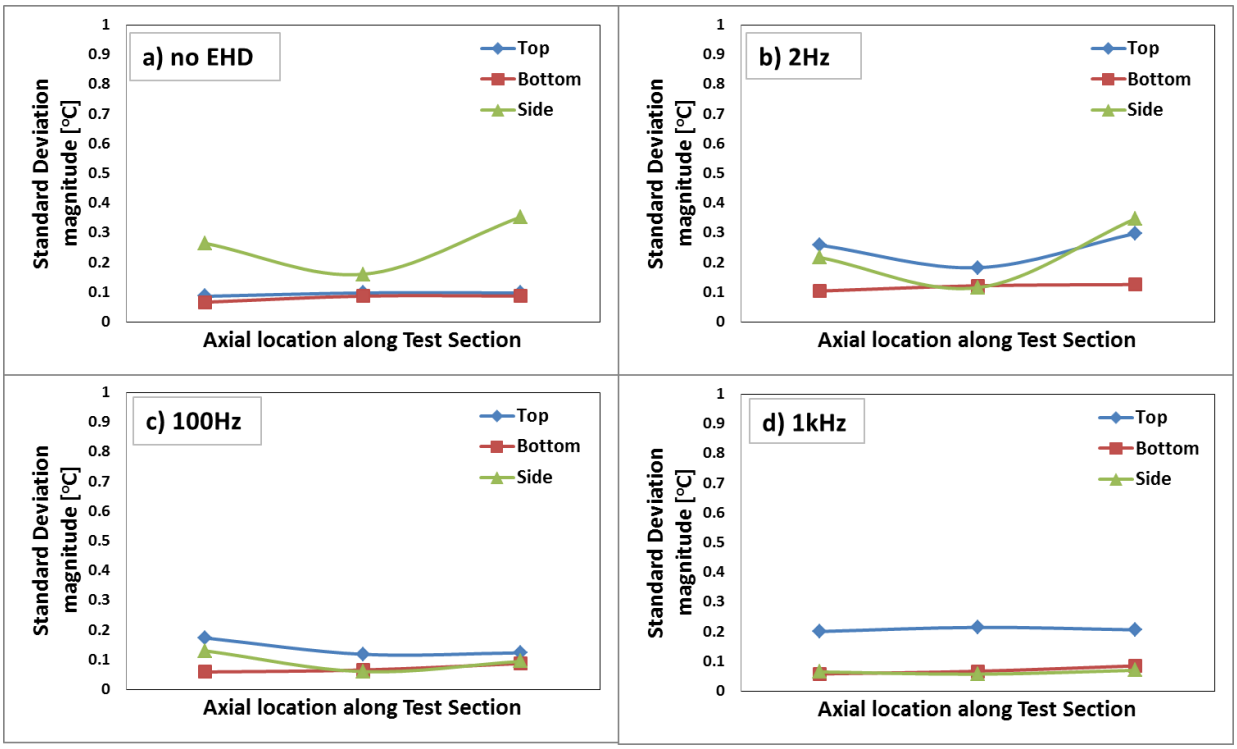

Figure 5.6: Surface Temperatures Standard Deviation: Convective Boiling -8kV Frequency. G = 60kg/m^{2}s, q" = -8.5kW/m^2, Xav = 40%, zero level, 50% duty

Figures 5.4d-f shows the effect of frequency on the surface temperature profiles for the -8kV pulse waveform. These profiles suggest an annular (Figure 5.4e) and annular intermittent type flow pattern (Figure 5.4d, f) induced by the high voltage waveform. This trend is in agreement with the -8kV DC results in chapter 4. However, more mixing and pulsing behaviour can be seen for these results, particularly the 2 Hz case, Figure 5.4d. The local heat transfer coefficients for the bottom surface steadily decrease from 4825 to 3890 W/m^2K with increasing frequency whereas the top surface heat transfer coefficients first increase from 2444 W/m^2K to 2780 W/m^2K from 2 Hz to 100 Hz and then it drops to 2350 W/m^2K at 1 kHz. This is the negative case and, as evident from chapter 4, the liquid is repelled from the electrode due to the signal polarity. This causes slightly different wetting characteristics than seen in the positive case which is responsible for the differences in heat transfer coefficient seen here. At 2 Hz the frequency is sufficiently low enough to allow for significant liquid extraction from the bottom surface and subsequent repulsion of this liquid toward the top surface. As the frequency is low the mixing induced on the bottom half of the tube will be significant and the heat transfer coefficient will be high. At 100 Hz, there is less time for a full extraction every cycle and so less liquid is taken into the core region and less liquid is repelled toward the top surface, the liquid film is thinner and therefore the top surface heat transfer is improved over the 2 Hz case. As the frequency increases further, the liquid extraction gets cut off by the next pulse and therefore it is likely that the mixing induced in the bottom half of the tube is less vigorous compared to the 2 Hz case such that the heat transfer coefficient drops. Finally at 1 kHz, the frequency is sufficiently high that the system behaves quite similarly to a DC case. There will be less liquid extraction per cycle and therefore less repulsion toward the top surface. However, now it is possible that the top surface is drying out more than in the 100 Hz case which could cause the slight drop in top heat transfer coefficient. Again the high frequency results in less mixing in the bottom half of the tube compared to lower frequencies and therefore the bottom surface heat transfer coefficient reduces further. The optimum wetting characteristics due to these conflicting trends seem to occur around the 100-200 Hz range, similar to the positive case.

It should be noted that the optimum conditions for convective condensation subject to +8kV pulse waveforms were in the 1-10 Hz range. (Ng, et al., 2011) At this range, the pulses are relatively far apart, allowing for significant falling film to occur on the top and sides of

the tube, compared to higher frequencies, and this allows for good condensation heat transfer before the next pulse occurs.

5.1.2 The Effect of Duty Cycle

The effect of duty cycle for pulse waves at 2 Hz, 10 Hz and 200 Hz, zero DC level for positive and negative 8kV amplitude on heat transfer and pressure drop was investigated. These waveforms are shown in Figure 5.7. The effect of the 200 Hz data on heat transfer and pressure drop is shown in Figures 5.8 and 5.9 respectively.

Figure 5.8 and 5.9 show both pressure drop and heat transfer increasing with increasing duty cycle, with the maximum occurring at the 100% duty a.k.a. the DC case. This trend of increased enhancement with increasing duty cycle was also found for condensation tests studied by (Sadek, 2009) and (Ng, 2010). Increasing the duty cycle increases the EHD "on-time" or the "effective voltage" so the time spent at high voltage increases and this induces more flow redistribution and consequently improves the heat transfer at the expense of additional pressure drop. As expected, negative voltages are more effective in increasing heat transfer and pressure drop for convective boiling than positive voltages.

The flow redistribution can be inferred using the surface temperature profiles, Figure 5.10 and their associated standard deviations, Figure 5.11 and 5.12. For the case of positive 8kV amplitude, Figure 5.10a-c, the surface temperatures and standard deviations seem to suggest a stratified wavy to inverted annular flow pattern transition with increasing duty as the bottom surface temperature drops indicating lower thermal resistance as the liquid is extracted toward the electrode. There is also more variance in the top and side temperatures with increasing duty cycle possibly indicating the increasing presence of liquid droplets impinging on these surfaces expelled from the highly mixed flow surrounding the electrode. Increasing the duty cycle increases the average local top and bottom heat transfer coefficients steadily from 1300 – 1400 W/m^{2}K and 3000 – 8000 W/m^{2}K respectively.

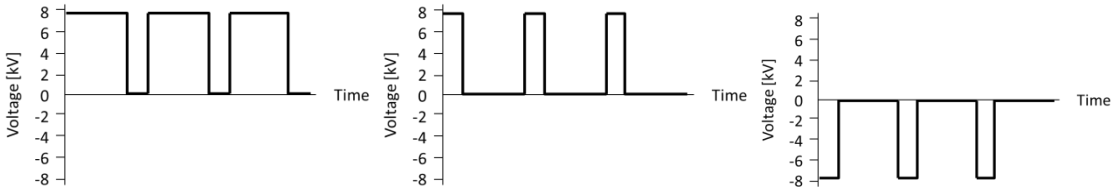

Figure 5.7: **The Effect of Duty Cycle Waveforms, 10Hz. 8kV High Duty Cycle (Left), 8kV Low Duty Cycle (Middle), -8kV Low Duty Cycle (right)**

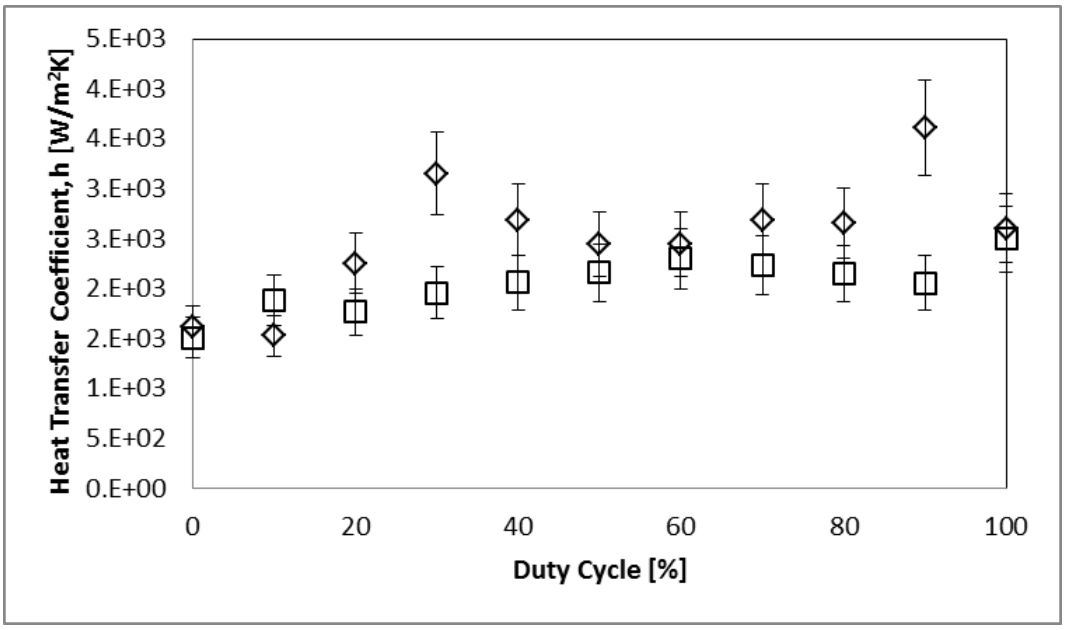

Figure 5.8: **The Effect of Duty Cycle on Convective Boiling Heat Transfer.**
G = 60kg/m^{2}s, q" = -8.5kW/m^2, Xav = 40%, 10Hz, □ +8kV ◊ -8kV

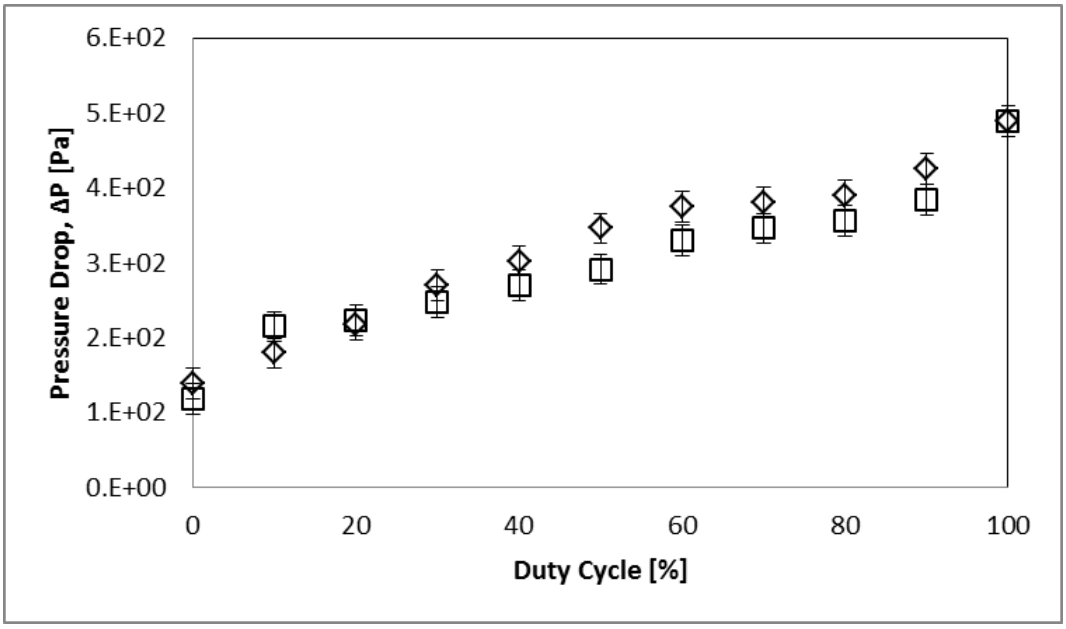

Figure 5.9: **The Effect of Duty Cycle on Convective Boiling Pressure Drop.**
G = 60kg/m^{2}s, q" = -8.5kW/m^2, Xav = 40%, 10Hz, □ +8kV ◊ -8kV

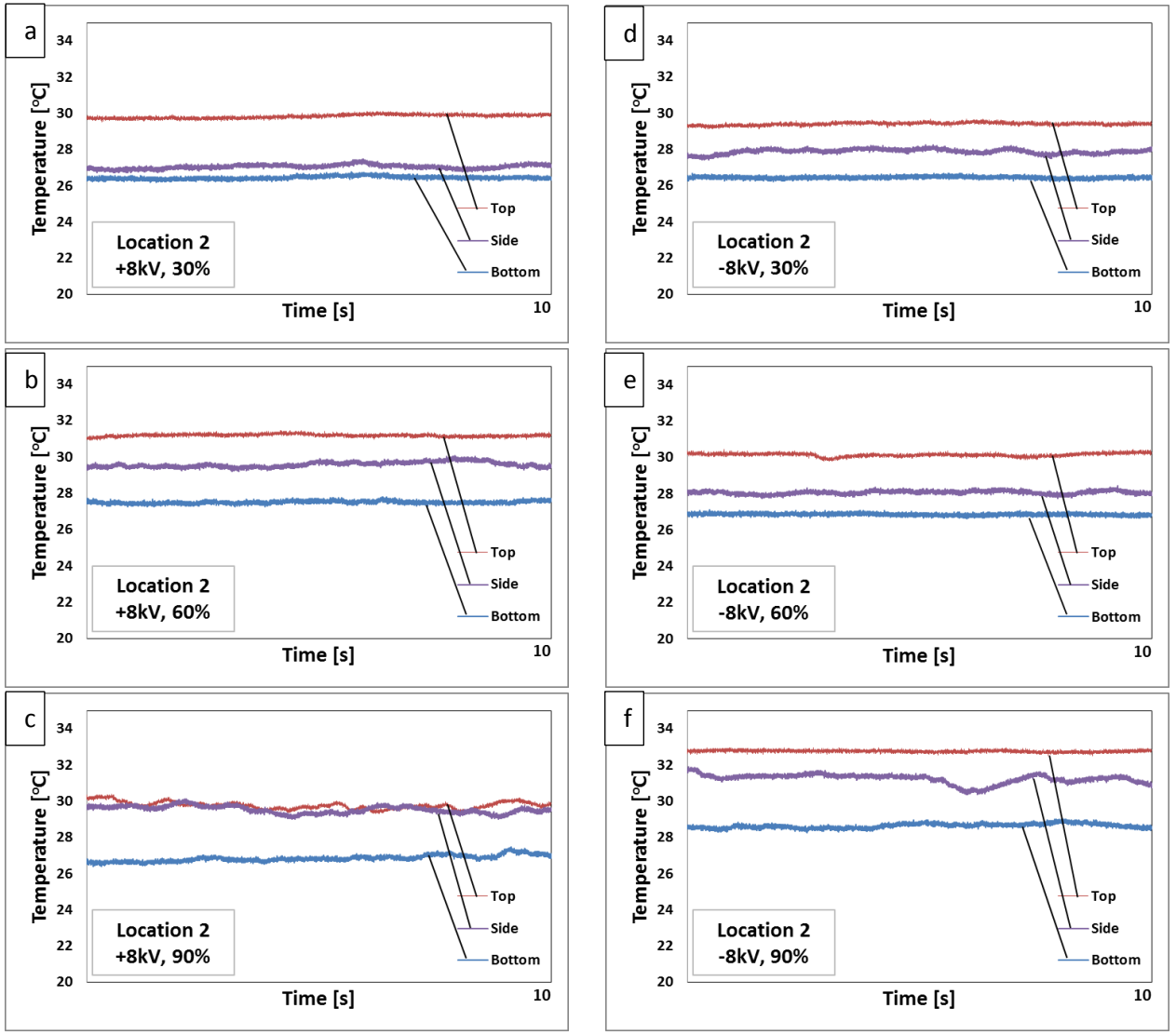

Figure 5.10: Convective Boiling Temporal Surface Temperature Profiles for the Effect of Duty Cycle Surface Temperature Profiles, +8kV (left) -8kV (right), G = 60kg/m^{2}s, q" = -8.5kW/m^2, Xav = 40%

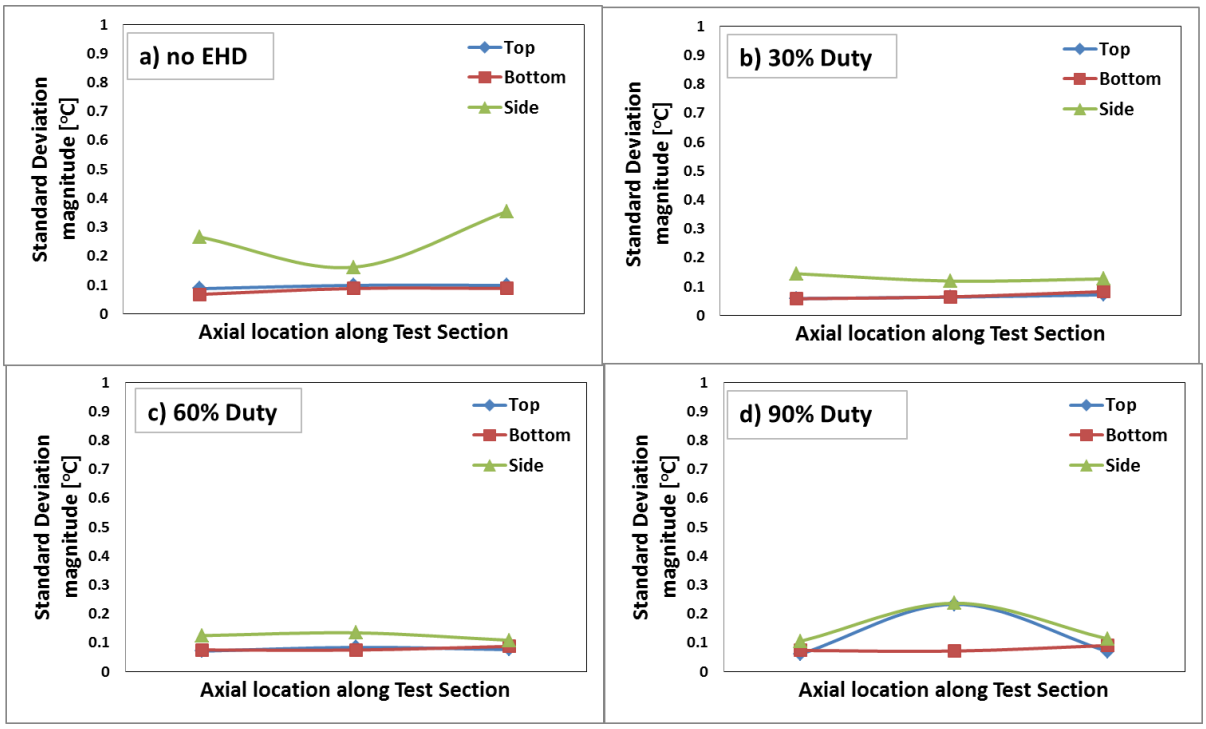

Figure 5.11: Convective Boiling Surface Temperatures Standard Deviation: +8kV Duty. G = 60kg/m^{2}s, q" = -8.5kW/m^2, Xav = 40%, zero level, 10Hz

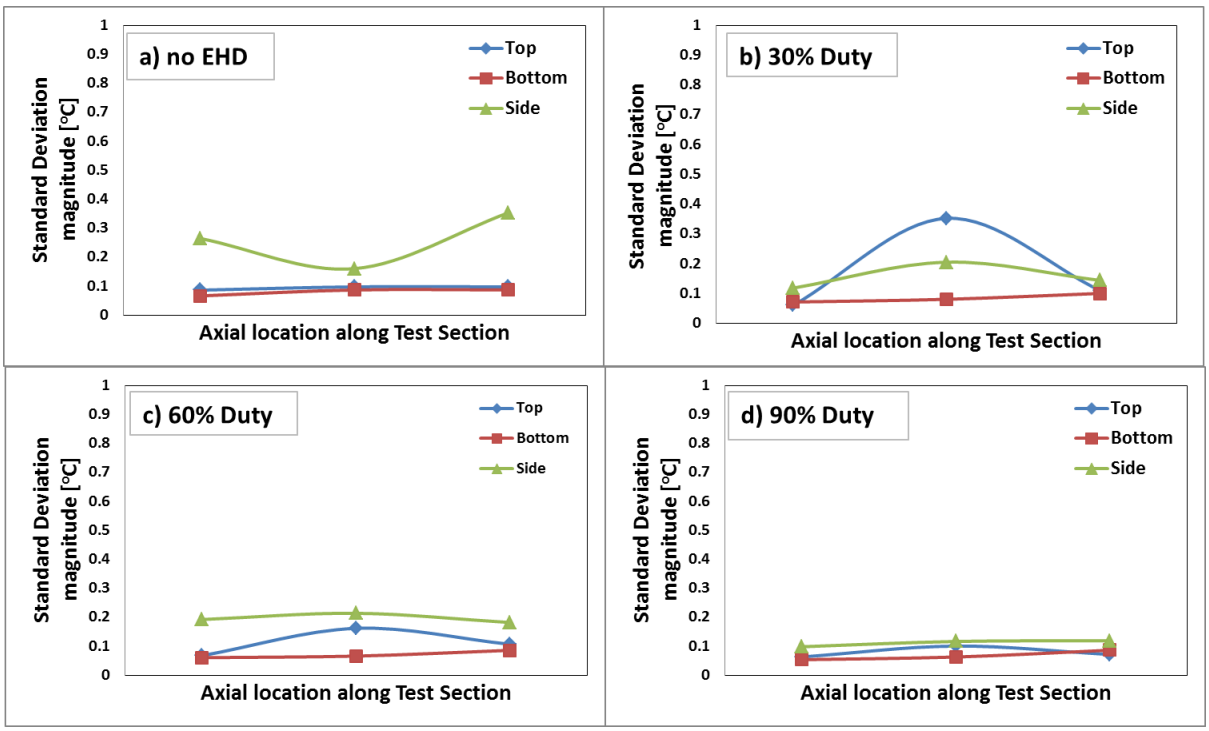

Figure 5.12: Convective Boiling Surface Temperatures Standard Deviation: -8kV Duty. G = 60kg/m^{2}s, q" = -8.5kW/m^2, Xav = 40%, zero level, 10Hz

Figures 5.10d-f show the surface temperature profiles for the case of -8kV duty cycle. They seem to suggest a transition from stratified wavy to intermittent and subsequently an intermittent annular flow regime with increasing duty cycle. For the case of negative 8kV amplitude, as the duty is increased, the effective voltage is increased and therefore the stronger the liquid repulsion mechanism. At high duty cycles, this liquid repulsion force causes more of the axial length of the test section to be in the annular regime rather than the intermittent regime which improves the heat transfer. The average local heat transfer for the top and bottom heat transfer surfaces increase from 1100 – 3000 W/m^2K and 3500 – 9000 W/m^2K respectively with increasing duty cycle.

The effect of duty cycle for 2 Hz, 10 Hz and 200 Hz on heat transfer and pressure drop is compared in Figures 5.13 and 5.14 respectively. As the frequency decreases, the EHD 'on-time' increases and therefore the signal behaves more like a DC signal which increases the system heat transfer and pressure drop. This increase in EHD induced mixing can be seen clearly from the flow visualisation of the -8kV, 2 Hz frequency data in Figure 5.15. Without EHD, the system remains in a stratified wavy flow pattern. Upon application of the 30% duty cycle pulse waveform, the liquid is extracted toward the electrode and starts to form a stratified wavy/inverted annular type flow pattern. Some twisted liquid columns are seen forming at this point. Increasing the duty to 60% and 90% results in an increase in the number of twisted liquid column like structures, more bulk mixing and an intermittent type flow pattern where some slugs reach the top surface. Finally for the DC case, the continuous applied voltage allows for liquid to be consistently repelled such that an annular flow on the heat transfer surface is established, greatly enhancing the boiling heat transfer characteristics.

It must be noted that there seem to be some anomalies from the main trend in heat transfer coefficient data in Figure 5.13 and that similar anomalies were found in Sadek et al., 2011. It is likely that these locations correspond to points where the induced wetting characteristics are quite suitable for convective boiling heat transfer enhancement.

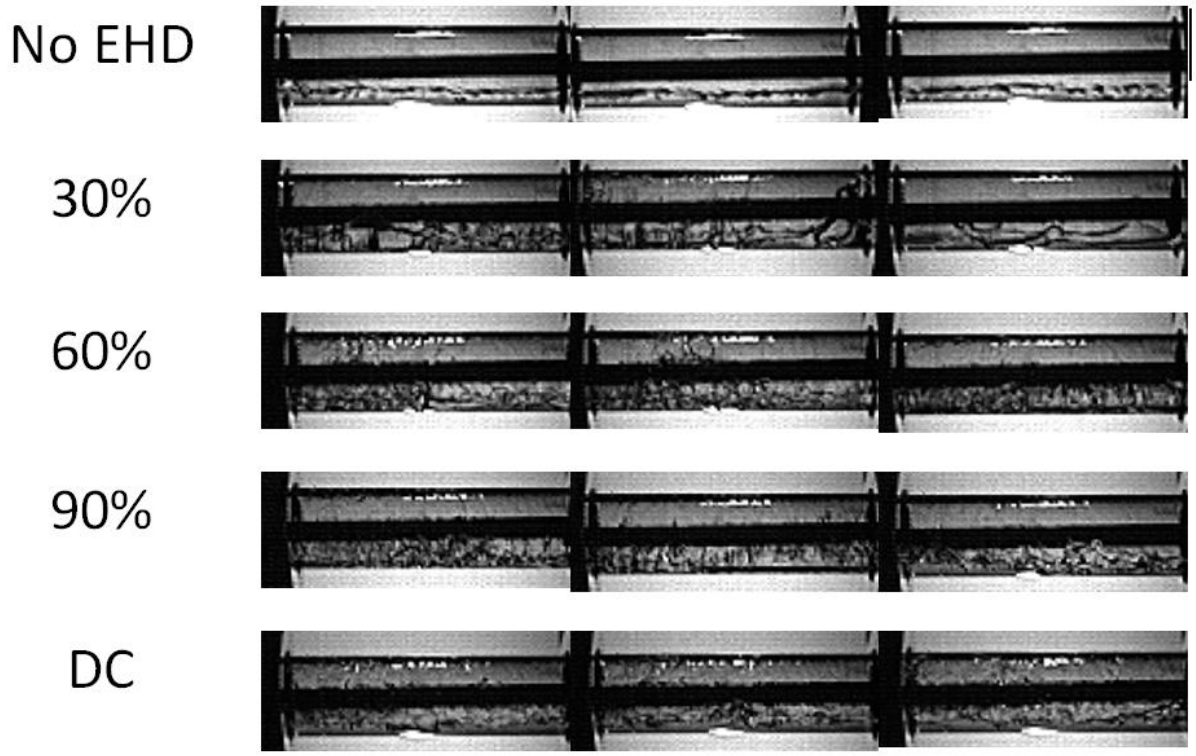

Figure 5.13: Flow Visualisation: The Effect of -8kV, 2Hz, Duty Cycle on Convective Boiling, G = 60kg/m2s, q" = -8.5kW/m2, Xav = 40%

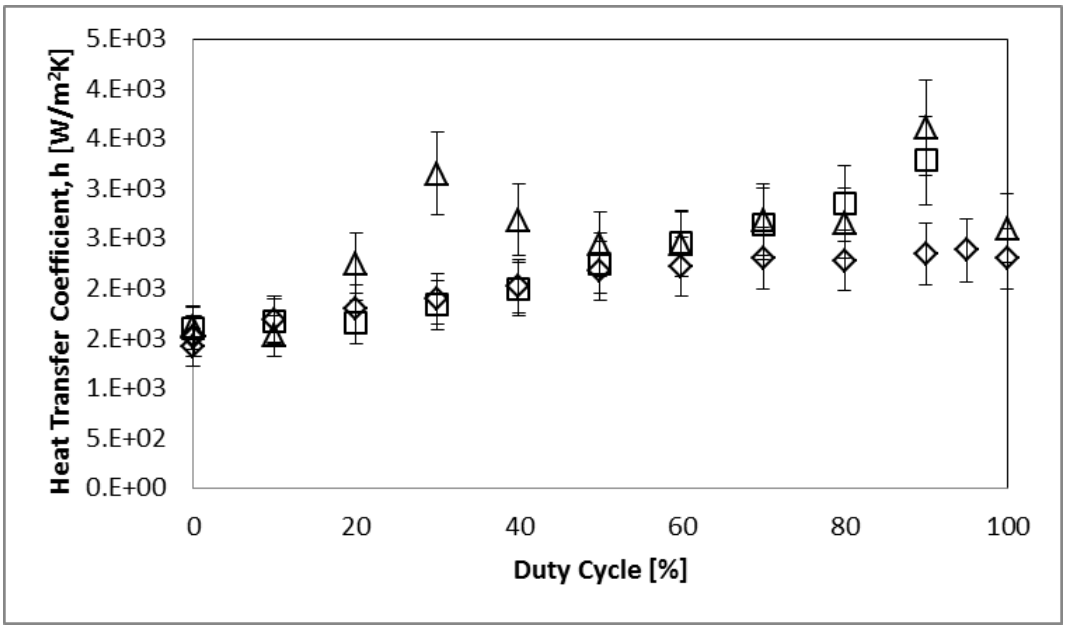

Figure 5.14: The Effect of Frequency and Duty Cycle on Convective Boiling Heat Transfer: G = 60kg/m^{2}s, q" = -8.5kW/m^2, Xav = 40%, zero level, -8kV. ◊ 2Hz □ 10Hz Δ 200Hz

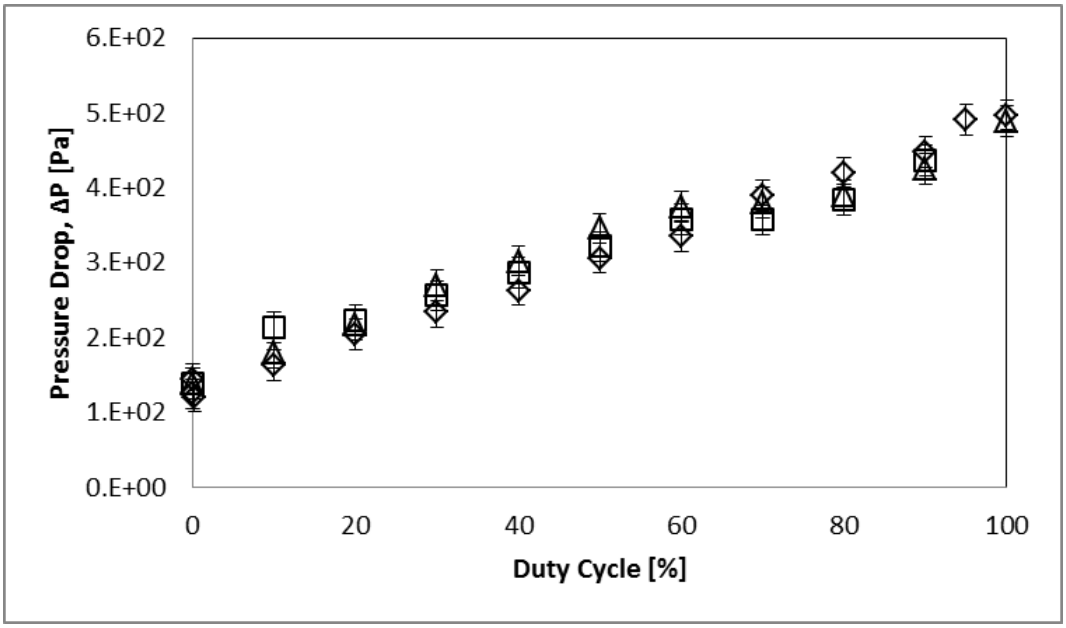

Figure 5.15: The Effect of Frequency and Duty Cycle on Convective Boiling Pressure Drop: G = 60kg/m^{2}s, q" = -8.5kW/m^2, Xav = 40%, zero level, -8kV. ◊ 2Hz □ 10Hz Δ 200Hz

5.1.3 The Effect of DC Level

The effect of DC level for a pulse wave, 50% duty cycle, 2kV peak-peak voltage, 200Hz on heat transfer on pressure drop is shown in Figure 5.17 and 5.18 respectively. Due to the small peak to peak voltage, the results are similar in trend to the DC results with increasing pressure drop and heat transfer coefficient corresponding to increasing voltage as a result of increased induced bulk mixing.

Looking at the surface temperatures in Figures 5.19 and the associated standard deviations in temperature, Figure 5.20, we can infer the flow pattern redistribution due to the effect of DC level. Figure 5.19a shows a very similar stratified wavy flow pattern to the one associated with the no EHD case. This suggests that the effect of flow redistribution due to EHD is minimal. This is confirmed when looking at the heat transfer and pressure drop results in Figures 5.17 and 5.18 respectively, where the zero DC level case and the no EHD case are almost identical. The average heat transfer coefficient for the top surface without EHD is 1090 W/m^{2}K and 1068 W/m^{2}K for the zero DC level case. The average heat transfer coefficient for the bottom surface without EHD is 2189 W/m^{2}K and 2208 W/m^{2}K for the zero DC level case. As the voltage amplitude is very small, 1kVDC oscillating around zero, this induces a weak electric field that is unlikely to be able to overcome the inertia of the fluid, hence the similar behaviour between the no EHD case and the zero DC level case.

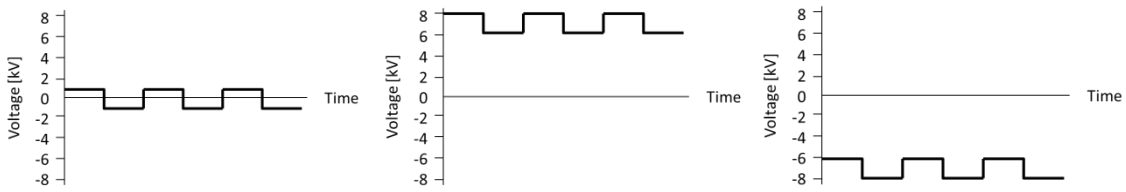

Figure 5.16: DC Level Waveforms. Zero Level (Left), +6KV Level (Middle), -6kVDC Level (Right)

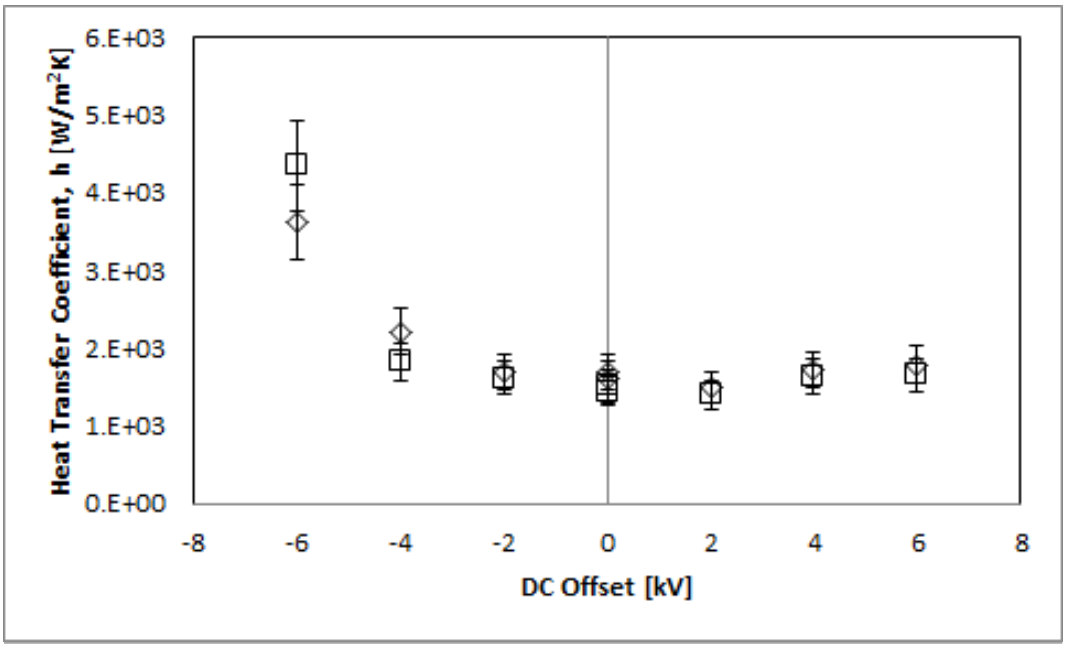

Figure 5.17: The Effect of DC Level on Convective Boiling Heat Transfer.
G = 60kg/m^{2}s, q" = -8.5kW/m^2, Xav = 40% ◊ 2kV pp, 1kHz, 50% duty □ 2kVpp, 200Hz, 50% duty

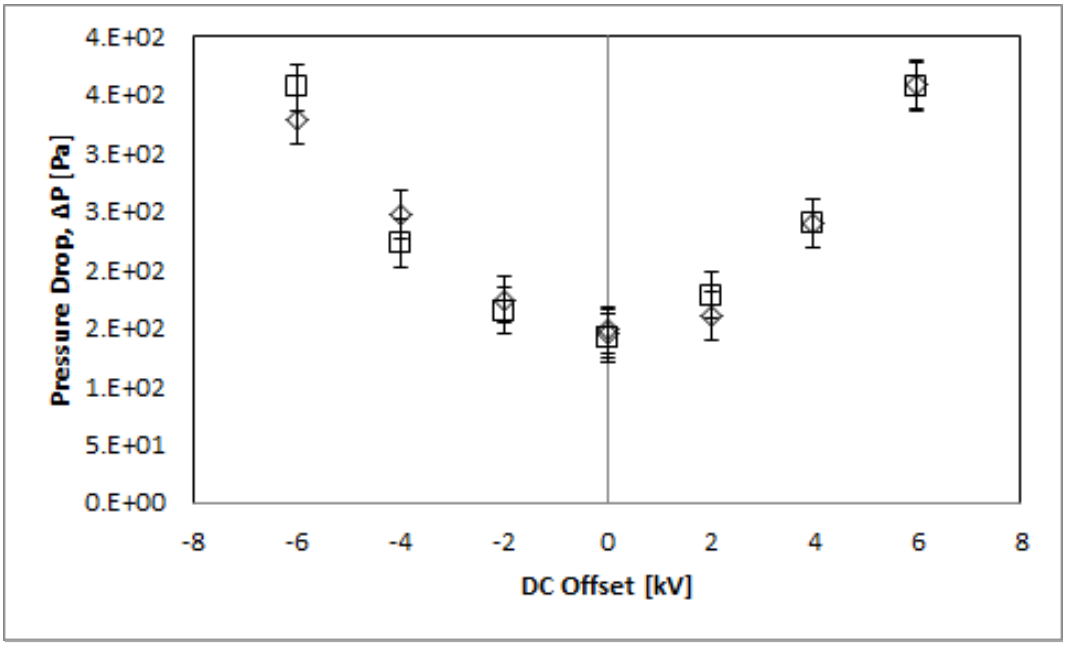

Figure 5.18: The Effect of DC Level on Convective Boiling Pressure Drop.
G = 60kg/m^{2}s, q" = -8.5kW/m^2, Xav = 40% ◊ 2kV pp, 1kHz, 50% duty □ 2kVpp, 200Hz, 50% duty

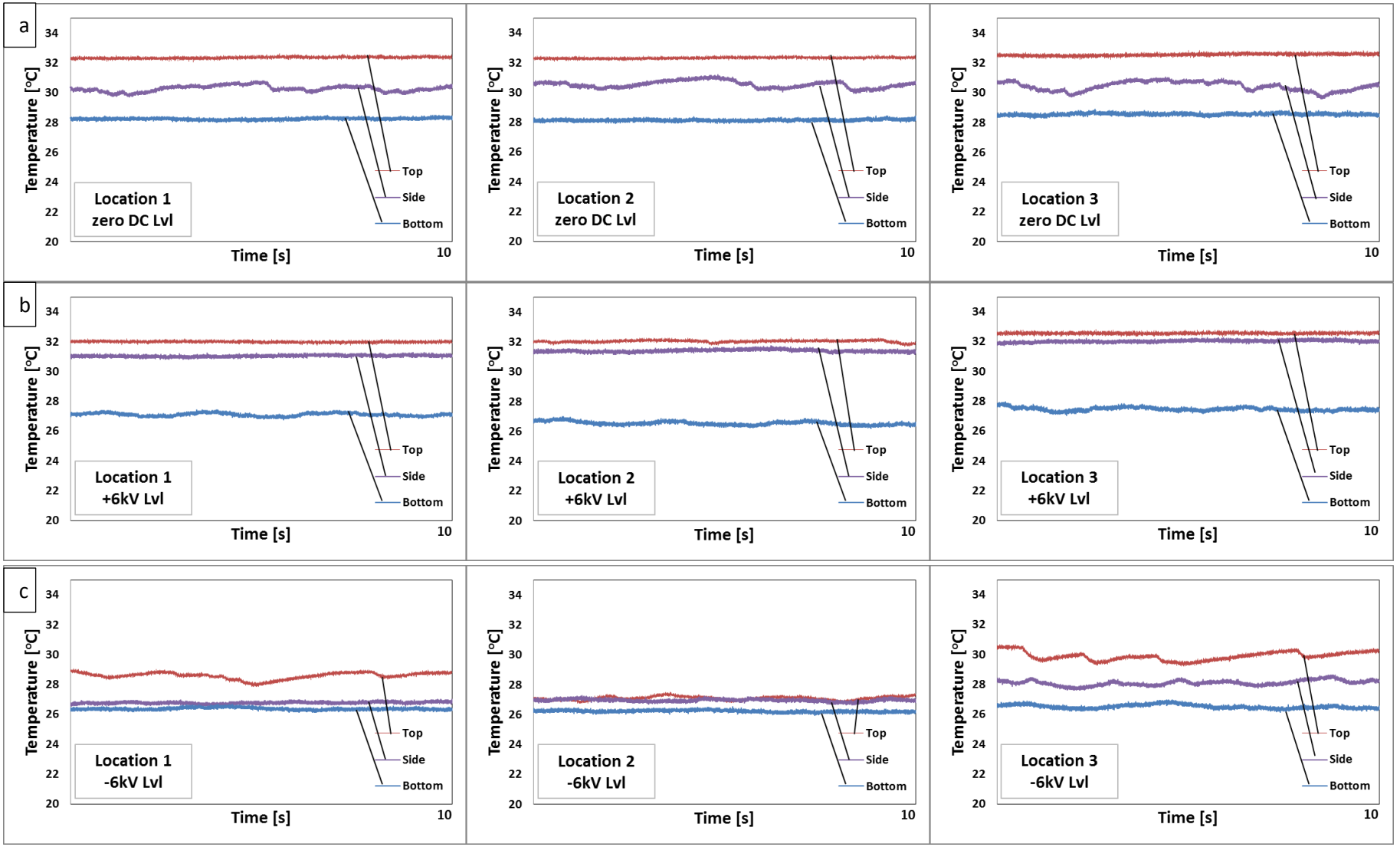

Figure 5.19: Convective Boiling Temporal Surface Temperature Profiles for the Effect of DC Level, 2kVpp, 200Hz, 50% Duty Temperature Profiles, G = 60kg/m^{2}s, q" = -8.5kW/m^2, Xav = 40%

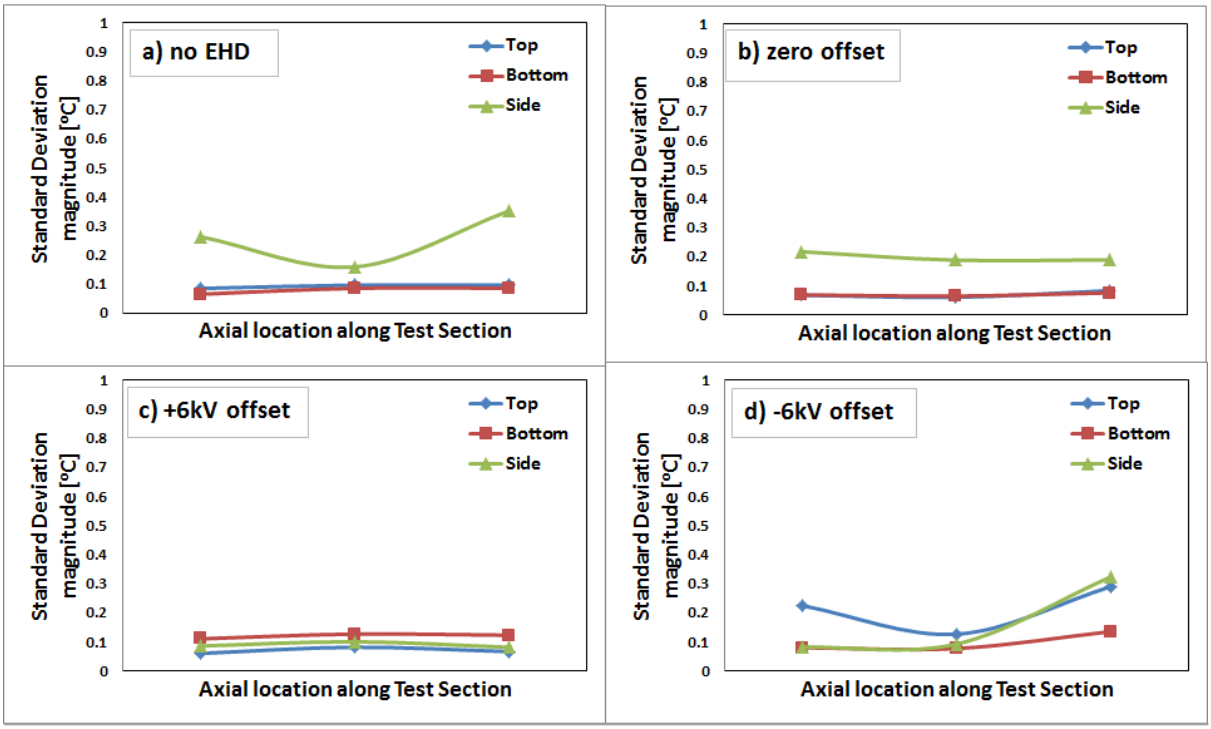

Figure 5.20: Convective Boiling Surface Temperature Standard Deviations. The Effect of DC Level G = 60kg/m^{2}s, q" = -8.5kW/m^2, Xav = 40%, 2kVpp, 50% duty, 200Hz

For the case of +6kV DC level, Figure 5.19b, we see that the bottom surface temperature is lower than the no EHD case, indicating a lower thermal resistance due to liquid uptake into the core region. This will improve the heat transfer for convective boiling as the liquid film is thinner on the heat transfer surface. The average heat transfer coefficient for the top surface has increased to approximately 1200 W/m^{2}K and the bottom heat transfer coefficient has increased to approximately 4700 W/m^{2}K, a twofold increase. For the case of -6kV DC level, Figure 5.19c, it is apparent that the surface wetting characteristics are different along the axial length of the tube as temperatures are varying along the length. The standard deviation of the top temperature Figure 5.20d, in particular, is higher than seen for both the no EHD case and the +6kV DC level case. This suggests that the flow pattern is a low frequency slug type intermittent pattern. Again the heat transfer enhancement for the negative case is higher than seen for the positive case. The average top heat transfer coefficient for the -6kV DC level case varies between 1800 W/m^{2}K and 5000 W/m^{2}K depending on the wetting of the top side of the tube i.e. the heat transfer is maximum when a slug of liquid wets the top surface as this increases the amount of liquid being evaporated locally. The average bottom surface heat transfer coefficient is approximately 8100 W/m^{2}K, an almost 4 fold improvement over the no EHD case. This is due to liquid uptake into the

core region and the upper portion of the tube, thus thinning out the liquid flow on the bottom surface, making it easier to evaporate.

5.1.4 The Effect of Peak-to-Peak Voltage

The effect of peak to peak voltage for a square wave at a frequency of 1kHz and a DC level of zero was investigated. This waveform is shown in Figure 5.21. The effect on heat transfer and pressure drop is minimal as shown in Figures 5.22 and 5.23 respectively.

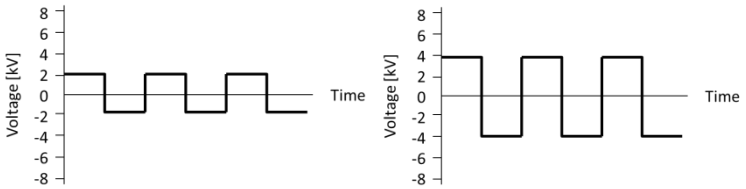

Figure 5.21: The Effect of DC Peak-Peak Waveforms. 4kVpp (Left, 8kVpp (Right)

Figure 5.22 seems to indicate that the peak to peak voltage, with zero DC level has little effect on the heat transfer. The effective applied voltage[1] is relatively small (<2.5kV) and the frequency is very high, therefore there the induced body force will be quite weak and the flow redistribution that these waveforms induce does not enhance heat transfer effectively. The pressure drop, Figure 5.23, seems to be increasing slightly with effective voltage although not as much as that seen in the DC or DC level tests, again likely due to the small effective voltage and high frequency.

The surface temperature profiles, Figure 5.24 show little deviation from the stratified wavy flow regime which supports the assumption that the effective voltage is small and not large enough to induce effective flow redistribution to improve heat transfer significantly. Some small enhancement can be seen from looking at the local heat transfer coefficients. Without EHD the average heat transfer coefficients were 1090 and 2189 W/m^2K for the top and bottom surfaces respectively. Upon application of 4kVpp, the top heat transfer coefficient remains within a similar margin of error at 1070 W/m^2K and the bottom heat transfer coefficient increases marginally to 2400 W/m^2K. Figure 5.25c shows some deviation in the top surface temperature induced by the applied 8kVpp waveform the heat transfer

[1] *Effective voltage is duty cycle x peak voltage. Peak voltage is half of the peak to peak voltage e.g. 4kV peak to peak with zero DC level has a peak of 2kV. So the effective voltage at 50% duty is 1kV.*

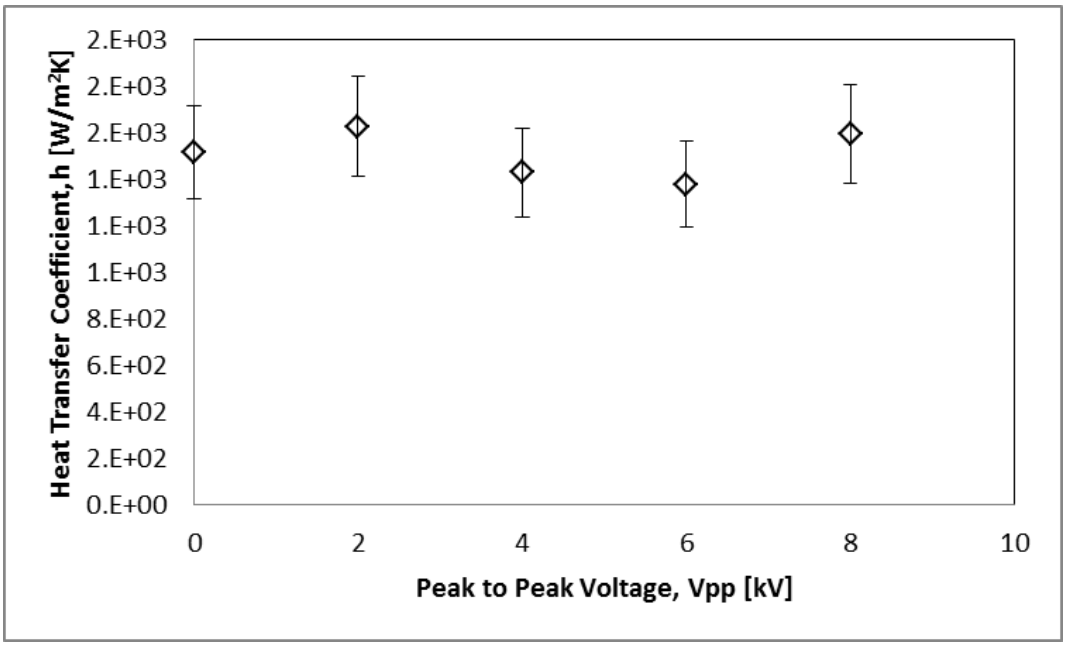

Figure 5.22: The Effect of Vpk-pk on Convective Boiling Heat Transfer (Vpk-pk).
G = 60kg/m^{2}s, q" = -8.5kW/m^2, Xav = 40%, zero level, 1kHz, 50% Duty

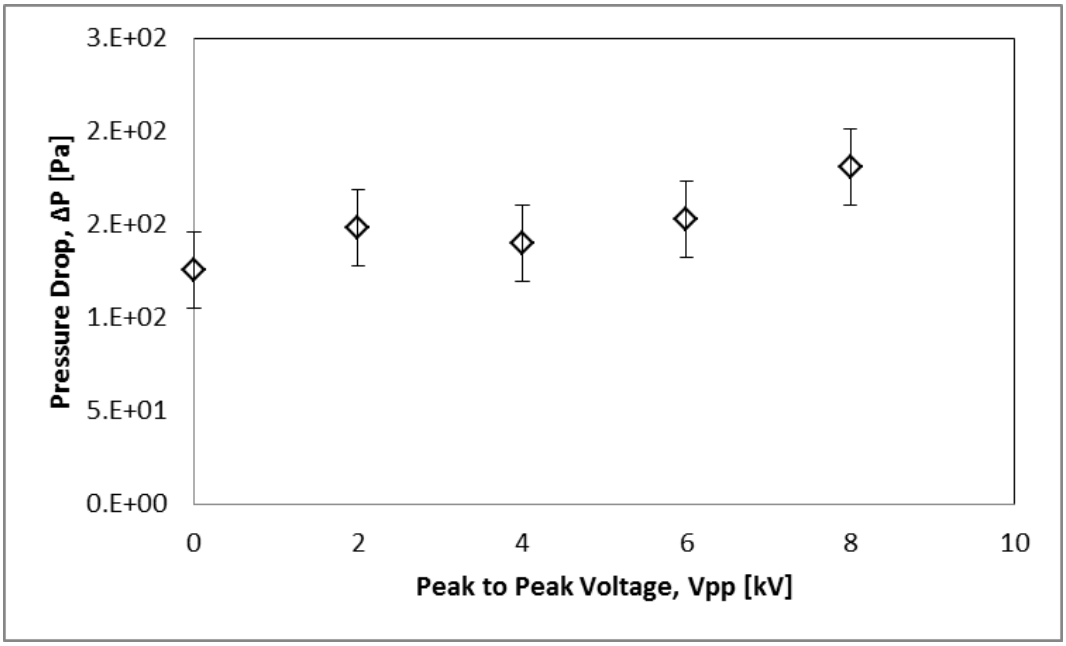

Figure 5.23: The Effect of Vpk-pk on Convective Boiling Pressure Drop (Vpk-pk).
G = 60kg/m^{2}s, q" = -8.5kW/m^2, Xav = 40%, zero DC level, 1kHz, 50% duty

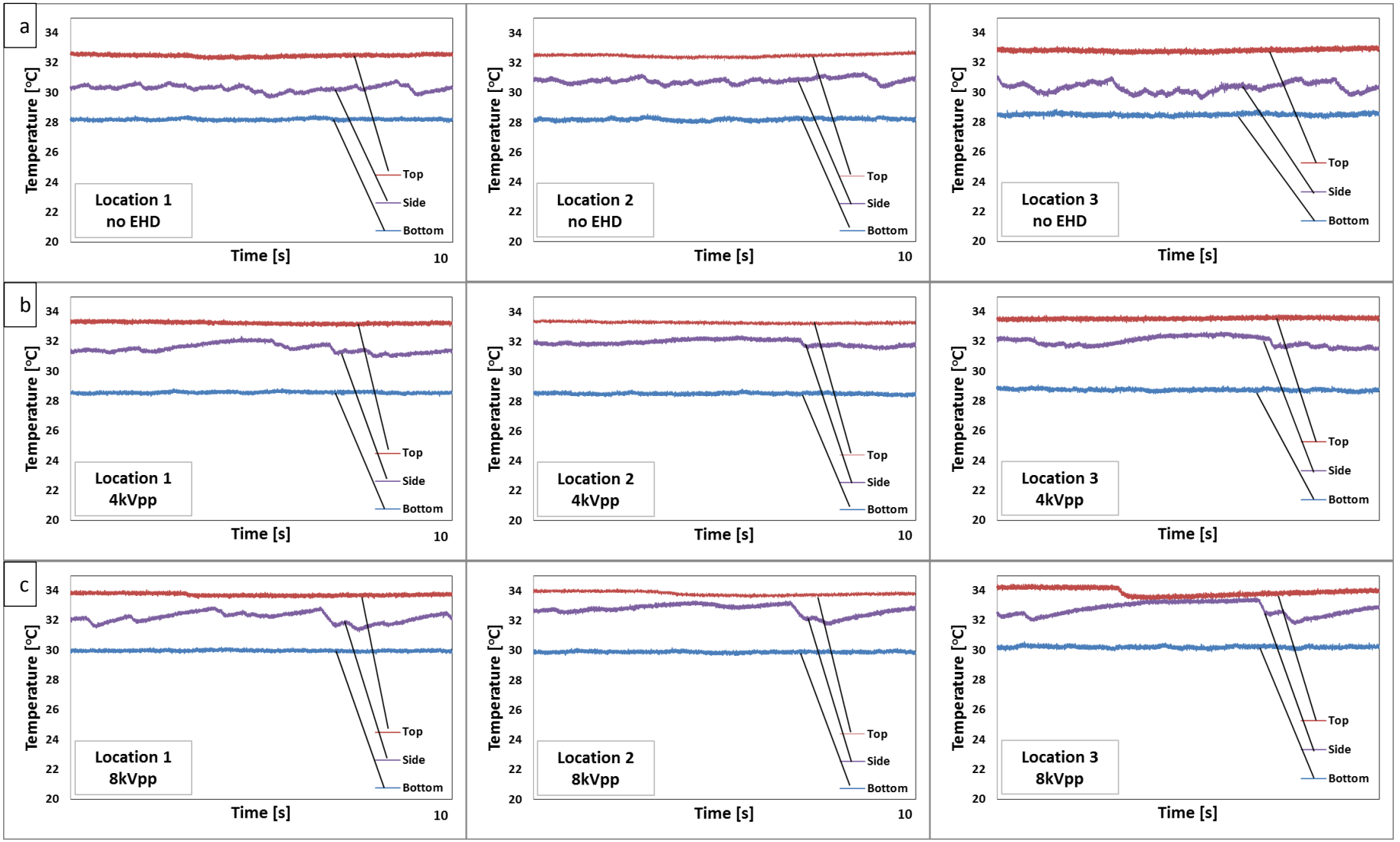

Figure 5.24: Convective Boiling Temporal Surface Temperature Profiles for the Effect of Peak to Peak Voltage, zero DC Level, 1kHz, 50% Duty Temperature Profiles, G = 60kg/m^{2}s, q" = -8.5kW/m^2, Xav = 40%

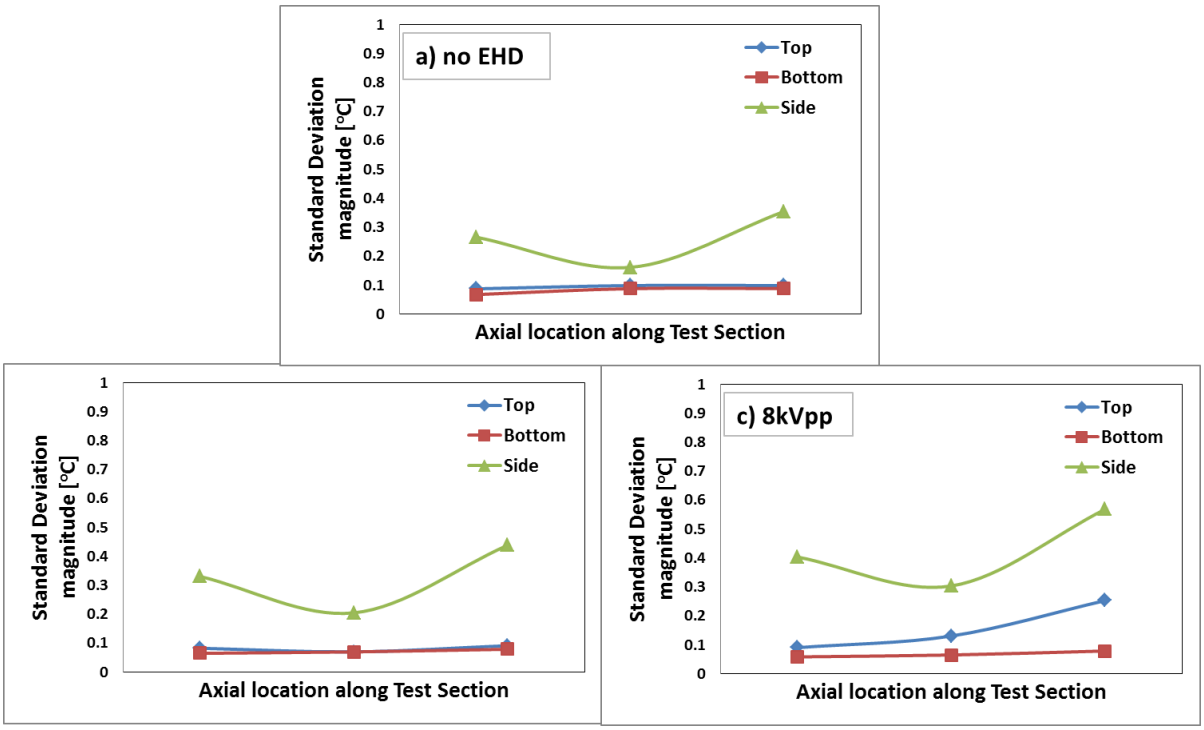

Figure 5.25: Convective Boiling Surface Temperatures Standard Deviation: Peak to Peak Voltage. G = 60kg/m^{2}s, q" = -8.5kW/m^2, Xav = 40%, zero DC level, 1kHz, 50% duty

coefficients have increased slightly at approximately 1150 and 2800 W/m^{2}K for the top and bottom surfaces respectively. These coefficients are within the range of what has been seen for a stratified wavy flow regime which supports the theory that the flow pattern hasn't changed significantly as a result of the applied waveforms.

5.2 Range of Controllability

Following the parametric study discussed in section 5.1, Figure 5.26 summarises the compilation of test results. The heat transfer enhancement ratio versus the pressure drop penalty for a number of different high voltage configurations including, the effect of DC voltage, the effect of varying DC level for two different peak to peak amplitudes, the effect of varying peak to peak voltage for zero DC level, the effect of varying frequency and the effect of varying duty cycle. The key point that this graph shows is that different EHD waveforms can induce variations in the flow pattern and thereby produce different heat transfer and pressure drop configurations. This plot can be used to design an EHD control strategy for the current system flow parameters. It must be noted that the pressure drop plotted in this graph is the test section pressure drop. The overall pressure drop is a combination of this and the system pressure drop which includes friction losses along the tubes and the losses in each component. The overall system pressure drop is system dependent and depending on

the system design can be more of less dominant than the EHD induced component of pressure drop. This is important as it will change the shape of Figure 5.26 and ultimately the controllability achievable with EHD. Additionally, different flow conditions other than those tested in this study may broaden or narrow this range of controllability, particularly if the electrode configuration is changed. For example higher quality flows have a lower liquid vapour interface and therefore an electrode placed eccentrically closer to the bottom of the tube may be more suitable.

Figure 5.26 shows that for most heat transfer coefficients achievable, there is a range of associated pressure drop penalties depending on the waveform applied. For example we can see that high heat transfer is achievable using 8kVDC waveforms, -8kV pulse waves at various frequencies and even -4kV DC level waveforms but the -8kV, 200 Hz pulse waveform is likely to have the lowest pressure drop penalty associated with it. At the other end of the scale, the varying peak to peak data at zero DC level, some of the 2kVpp with varying DC level data and some of the +8kV frequency data has very low heat transfer enhancement with relatively high pressure drop. In a system where the pressure drop due to EHD is highly dominant compared with the system pressure drop, it may be possible to use EHD as a method of reducing the heat transfer by retarding the system via increased pressure drop, rather than enhancing it.

It has been suggested that EHD can reduce the heat transfer at high vapour qualities as it can promote dryout. A set of experiments at a mass flux of 60 kg/m^{2}s, applied heat flux of -10 kW/m^2 and average test section quality of 55% and an applied voltage of positive 8kV were conducted. It was thought that the positive voltage would pull the liquid away from the heat transfer surface and promote dryout, thus reducing the heat transfer. In fact the heat transfer still improved by a factor of 1-1.2 for varying duty cycles. It is likely that the liquid interface – electrode gap distance in this case was too large to achieve a high enough interfacial force for sufficient liquid uptake into the core region to promote dryout and that the induced bulk mixing caused by the EHD waveform resulted in an enhancement. A smaller gap distance or a higher applied voltage, once below the breakdown limit, and higher vapour qualities may induce sufficient liquid uptake to promote dryout.

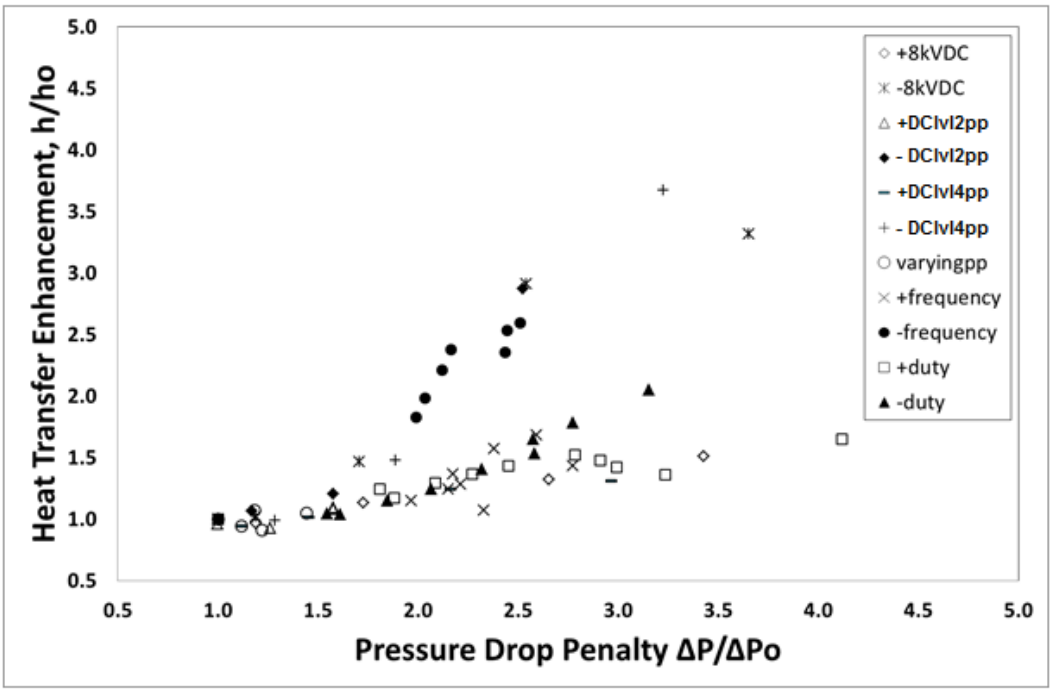

Figure 5.26: Convective Boiling Heat Transfer Enhancement v Pressure Drop Penalty. G = 60kg/m^{2}s, q" = -8.5kW/m^2, Xav = 40%

5.3 Load Control – Proof of Concept

From the results in chapter 4 and also from Figure 5.26, it is evident that the DC results provide one of the largest ranges of control of the heat transfer coefficient. Additionally, from an application point of view, DC voltage in proximity to commercial heat exchangers is most likely easier and cheaper to implement than pulse waveforms would be. For example spark plugs in an internal combustion engine of a car operate at 25kVDC so there is the potential to connect an EHD system up to an evaporator system in a car using the same power source. Based on this, a set of load control experiments using DC voltages was conducted and the results are shown in Figure 5.27.

DC EHD was used to control of the water side load (heat flux, q") in a R134a heat exchanger system. The system is initially operating at steady state flow conditions of 60 kg/m^{2}s mass flux, negative 7.6 kW/m^2 water side heat flux with an average flow quality of 40%. (red curve) At t = 5 seconds, the water flow rate is dropped from 2.554 L/min to 0.94 L/min. This sudden drop results in a spike in the load which recovers and the water side heat flux is now reduced to -4.4 kW/m^2. There are two different applications of EHD shown in this plot. The slow and wavy (purple) line corresponds to a manual increasing of the DC applied

voltage until the original load conditions are re-established. The green line corresponds to -8kVDC being applied instantly at t=15 s to re-establish the original load conditions. The response time for full recovery based on this signal is approximately 5 seconds. Finally the last portion of the graph (orange) shows the removal of EHD and again, over a period of approximately 5 seconds, the system returns to the pre-EHD flow conditions. This graph highlights the proof of concept of using EHD to rapidly control heat exchanger performance with changes of up to approximately 3.2 kW/m^2 achievable within 5 seconds for the current system.

The Power required to achieve this enhancement is calculated using Equation 5.1

$$EHD \text{ Power} = \text{V x I} \qquad \textbf{Eqn 5.1}$$

The applied voltage, V, used was 8kV and (Ng, 2010) measured the current voltage characteristics for the system used in this study and found the corresponding current, I, associated with +8kV was 1.5E^{-6} A. Therefore the power used to achieve this enhancement is 0.012 W.

For comparison purposes, the same experiment was conducted using the refrigerant flowrate as a method of controlling the water side heat flux load. Figure 5.28 shows the results from this test. The water side heat flux at time t = 0 s is approximately -7.4 kW/m^2 and at time t = 3 s the water flowrate is dropped such that the heat flux drops to approximately -4.3 kW/m^2 as before. This time the flowrate is dropped more slowly and as a result the spike seen in Figure 5.27 is eliminated. At approximately t = 6 seconds the refrigerant flowrate is increased from 60 kg/m^{2}s to approximately 120 kg/m^{2}s and this restores the load to its original value in approximately 5 seconds. Then at approximately t = 12 s the refrigerant flow rate is brought back to its original 60 kg/m^{2}s set point and the load drops again to -4.3 kW/m^2 in approximately 4 seconds.

A power meter connected to the variac controlling the refrigerant gear pump was used to record the pumping power. At the no EHD mass flux of 60kg/m^{2}s, the required pumping power was 15 W. When the mass flux was increased to 120kg/m^{2}s to control the load, the pumping power increased to 19W. Therefore the additional pumping power required is 4W. This is approximately two orders of magnitude higher than as required for the same level of control using EHD. It should be noted that it is not ideal to change the flowrate in a system that is operating at steady state as it is generally optimised to operate within a narrow range

of flowrates and it may not be possible to double the flowrate without degregating the system performance. For example, this EHD control test shown in Figure 5.27 resulted in a minimal change in the flow quality, within 10%, whereas the test section flow quality dropped significantly, from 40% to approximately 15%, when the flowrate was increased in test shown in Figure 5.28. Such a significant change in vapour quality would not be tolerated in a real application as it may damage system components such as pumps, fans or turbines. Although the load is brought back to its setpoint, the system has not been controlled as the flow quality has changed by over 20% and the refrigerant would need to be preheated to restore the inlet vapour quality to what it was before the load dropped.

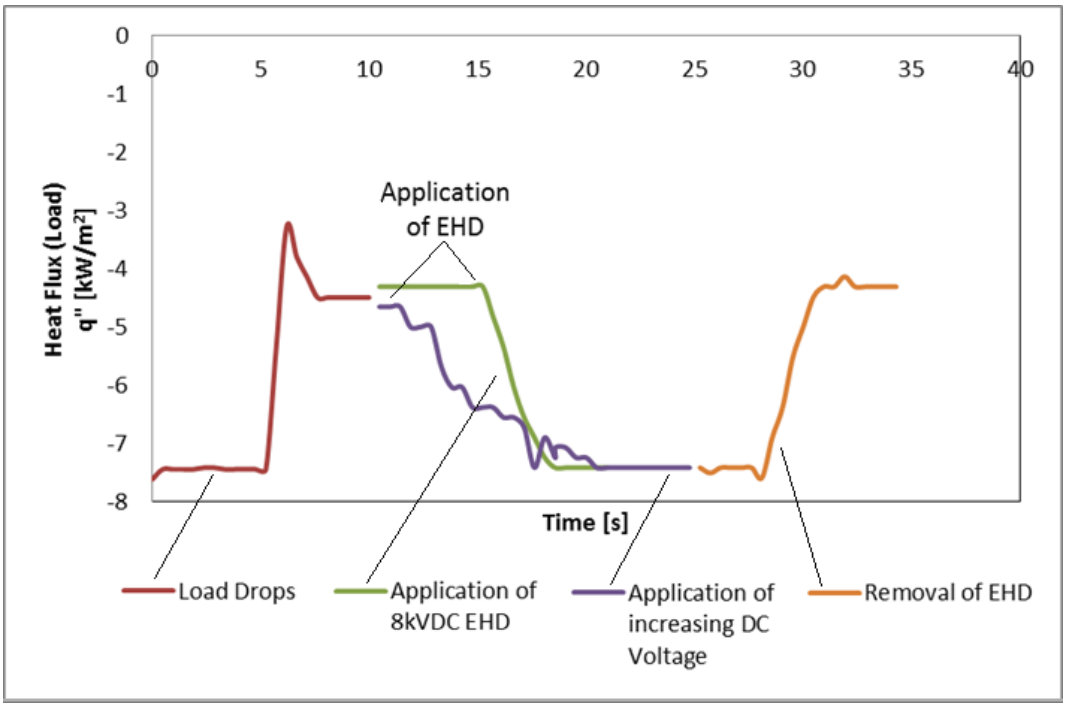

Figure 5.27: Load Control using -8kVDC Applied Voltage.
G = 60kg/m^{2}s, q" = -7.5kW/m^2, Xav = 40%

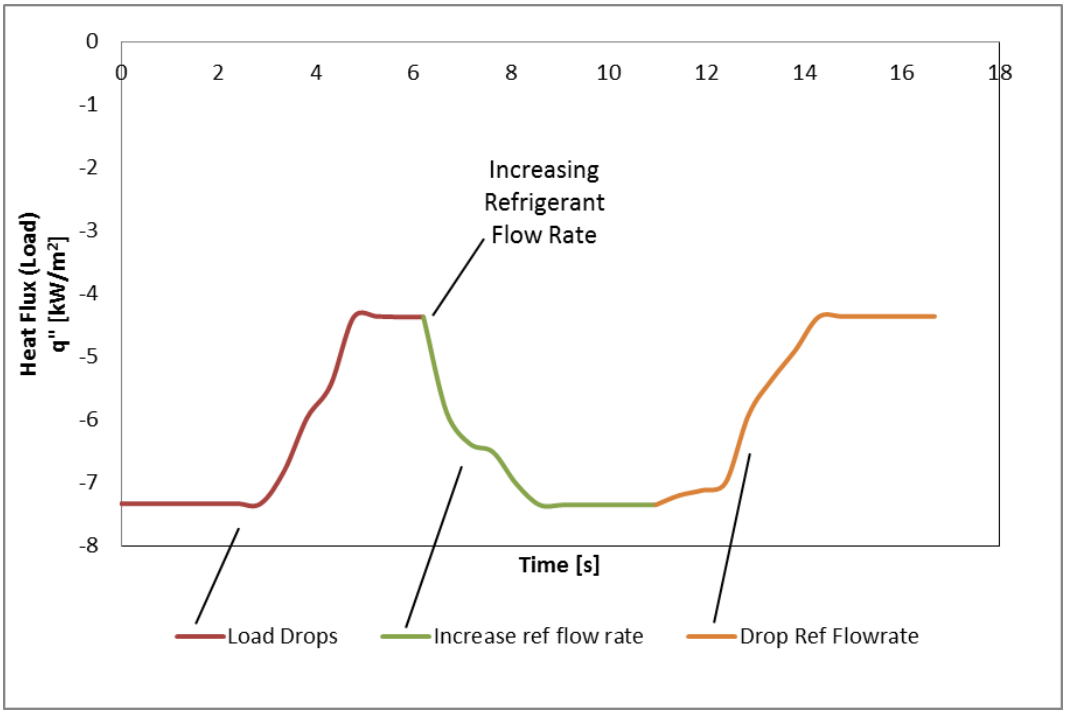

Figure 5.28: Load Control using Refrigerant Flow Rate.
G = 60kg/m^{2}s, q" = -7.5kW/m^2, Xav = 40%

5.4 Chapter Summary

The range of controllability for the same set of flow parameters used in Chapter 4 was explored using pulse waveforms. The effect of DC level, peak to peak voltage, frequency and duty cycle waveform parameters on convective boiling enhancement were studied. It was found that these various waveform parameters can induce different flow patterns and consequently different heat transfer and pressure drop configurations. In general the heat transfer is enhanced by EHD, but different pressure drop penalties can be achieved for a given enhancement ratio using different waveforms. High heat transfer with low pressure drop was seen for the 50% duty, -8kV frequency data and negative DC data. In some cases the enhancement is quite little compared to the pressure drop, for example the zero DC level, varying peak to peak voltage data. It is suggested that in a system where the heat exchanger pressure drop due to EHD is more dominant than the system pressure drop, it may be possible to use EHD as a method of retarding the system rather than enhancing it thereby broadening the scope of controllability.

Finally the proof of concept of using DC EHD as a rapid control mechanism for the load conditions was shown. Using -8kVDC the water side heat flux could be varied by approximately ±3.2 kW/m^2 within 5 seconds. This was compared to a method of control whereby the load is controlled by varying the refrigerant flow rate. Similar response times and ranges of control were achievable using EHD compared with varying the flow rate. However the required power is two orders of magnitude higher than that using EHD. In addition, the variation of flow parameters is minimal with EHD control compared to that when varying the flow rate and as such, EHD is a more useful method of control without degrading system performance or damaging system components that may occur with large changes in the flow quality.

Chapter 6: Conclusion

Electric fields can be used as a method of enhancing heat transfer and furthermore have the potential to control the heat transfer as they are an active enhancement technique. This technique is most effective when used in multiphase applications as the dielectrophoretic and the electrostrictive components in the electric body force are dominant when there is a large difference in the permittivity between the phases and this can induce phase migration, a.k.a. flow pattern redistribution which ultimately affects the system heat transfer and pressure drop characteristics.

In this study, a short, 300 mm, test section was used to study the effect of EHD forces on flow redistribution in a horizontal, shell and tube heat exchanger subject to both boiling and condensation heat transfer. The parameters generally used to gauge the enhancement achieved with EHD are heat transfer coefficient and the two phase pressure drop. These are both flow pattern dependent parameters and since EHD causes flow pattern redistribution, the test section should be sufficiently short to maintain a consistent flow pattern along the length. The use of the short test section for this purpose has not been a priority for the majority of past researchers and those who have used it have not analysed the effect of voltage polarity or conducted a complete parametric study into the effect of different waveform parameters for convective boiling.

Chapter 4 explored the effect of DC signals on flow redistribution, heat transfer and pressure drop. It was found that there is an effect of polarity, something that was seen by Ng, 2010, for convective condensation for a similar system geometry type. For both polarities, the liquid is extracted toward the electrode due to the polarization forces acting at the liquid vapour interface. The flow then surrounds the electrode via liquid extraction as the liquid, which has a high dielectric constant, is attracted to the region of high electric field. Once the fluid surrounds the electrode, the liquid will be repelled due to the polarization forces arising from the now inverted electric field distribution. The electrophoretic force aids this repulsion for negative voltages and opposes this force for positive voltages, generating new flow patterns. Due to the repulsion seen for negative voltages, +8kVDC waveforms were shown to move the flow pattern from the stratified wavy regime to the annular/intermittent transition along the test section with some tests showing a fully annular induced flow

pattern. Lower voltages move the flow pattern to the intermittent regime where liquid slugs periodically reach the top surface. The positive voltages cause liquid uptake into the core region which changes the flow pattern from a stratified wavy pattern to an inverted annular flow pattern. In addition to this, flow phenomenon unique to EHD is seen. Twisted liquid cone structures are generated for positive applied voltages and twisted liquid column structures for negative applied voltage. For voltages above 4kV, the EHD induced bulk mixing is sufficient to cause droplet entrainment in the core and sometimes droplet impingement on the heat transfer surface. DC tests were carried for convective condensation and convective boiling with corresponding flow parameters. The flow pattern redistribution was inferred by analysis of the test section surface temperature profiles along with their standard deviations. The estimated flow patterns were then compared to flow visualisation data captured using a high speed camera at 2000 fps (frames per second). Using the surface temperature profiles to distinguish between the different flow patterns for the convective condensation tests was more difficult than for convective boiling as there is always a thin film of condensate on the top and side surfaces which results in surface temperatures being much closer in value. However, the flow visualisation data indicates that the EHD flow patterns are essentially the same for both condensation and boiling with the exception that there is, in fact, a thin film present on the top surface in condensation for the current flow parameters tested.

A liquid film on the heat transfer surface improves boiling heat transfer and removal of this film improves condensation heat transfer. Using this knowledge we were able to show that these flow distributions could be used to enhance different modes of heat transfer. Since the positive voltages maintain most of the liquid flow in the core region, they work best for condensation enhancement, whereas the negative voltages repel the liquid, wetting the heat transfer surface, making them more suitable to boiling heat transfer. A 2 fold increase in heat transfer performance was seen for positive applied voltages on convective condensation tests and a 4 fold increase in heat transfer performance was seen for the negative applied voltages on the convective boiling tests. The pressure drop penalty was approximately twofold for both condensation and boiling, as the flow patterns induced are the same for both. However, there is no discernible effect of polarity on the pressure drop results which is likely due to the EHD induced pressure drop not being the dominant pressure drop component in the current system and this can mask the effect of voltage polarity on the results.

In chapter 5, a parametric study into the effect of AC waveforms on convective boiling was discussed. As there are more variable parameters associated with AC waveforms e.g. the effect of DC level, peak to peak voltage, frequency and duty cycle, there is the potential to induce different flow patterns and consequently different heat transfer and pressure drop configurations compared to the DC signals. This can be used to expand the range of controllability achieveable for the current set of flow parameters tested. It was found that, in general, the heat transfer is enhanced by EHD, but different pressure drop penalties were be achieved for a given enhancement ratio using different waveforms. For some cases very high enhancement compared to pressure drop penalty was achieved e.g. the -8kVDC data and the -8kV, 50% duty, pulse data. These waveforms are ideal where performance enhancement with minimal power usage is required. In other cases the enhancement was minimal compared to the pressure drop, for example the zero DC level, varying peak to peak voltage data, where the heat transfer remained within the error bounds of the no EHD case but the pressure drop increased up to two fold. It is possible that in a system where the heat exchanger pressure drop due to EHD is more dominant than the system pressure drop, it may be possible to use EHD as a method of retarding the system rather than enhancing it thereby further broadening the scope of controllability.

Finally we showed the proof of concept of using DC EHD as a rapid control mechanism for the load conditions. Using -8kVDC the water side heat flux could be varied by approximately ±3.2 kW/m^2 within 5 seconds. This was then compared to a similar test where the refrigerant flow rate is used as an active method of load control. The response time for both control methodologies was similar but the pumping power requirements for increasing the flow rate were larger than the EHD power requirements by approximately two orders of magnitude for this particular test. In addition, it was found that EHD is a more suitable method of control as it causes a minimal change in the flow parameters, mass flux, G and vapour quality, x. On the other hand, to achieve the same level of enhancement, the refrigerant flow rate had to be doubled and this caused the flow quality to decrease by over 20%. In an industrial application, this large scale variation of flow conditions while the system is running at steady state would be unacceptable from both a performance point of view (pump/turbine efficiencies) and also from a safety point of view as low quality two phase mixtures at the outlet of an evaporator can pose serious risks for components such as turbines and compressors.

6.1 Recommendations for Future Work

This thesis discusses the use of various voltage waveforms on the enhancement of convective boiling transfer primarily for a set of flow parameters associated with a stratified wavy flow pattern before the application of EHD. These parameters were chosen to assess the mechanism of transition to other flow distributions, similar to the analysis of Taitel & Dukler, 1976, and they correspond roughly to the second pass of a 4-pass shell and tube boiler for most applications. Further work should be carried out using flow parameters which correspond to the other passes in these heat exchangers. It may be more suitable to use an eccentrically placed electrode in these regions to maintain a similar interfacial force as is induced in these experiments as it works quite effectively.

The use of EHD as a control mechanism was briefly touched on in this thesis. The concept of the use of DC EHD to control the load conditions was proved and this work should be expanded on, for example, by developing a PID controller that takes the water side heat flux as an input and regulates it to the required setpoint. Furthermore the scope of controllability was established for our flow conditions and this should be developed for flow conditions associated with other passes in an industrial heat exchanger, such that a control mechanism for the refrigerant side heat transfer coefficient and pressure drop can be developed. Having rapid flexibility in controlling both the load side and the refrigerant side performance would certainly promote EHD as a viable active heat transfer enhancement technique and move this research closer to developing a prototype.

Appendix A: Refrigerant Properties

Table A.1 shows the thermo-physical[2] and electrical properties for R134a.

Table A.1: Refrigerant Properties

Property	State	Correlation	R^2
Pressure [kPa]	Saturated	$\mathrm{P}_{sat} = -184.53 + 474.73\exp\left\{\frac{T_{sat}}{42.96}\right\}$	0.9999968
Density [kg/m^3]	Subcooled Liquid	$\rho_{\mathrm{l}} = 1290.68 - 2.317\mathrm{T}^{1.1173}$	0.999979
	Saturated Liquid	$\rho_{l,\mathrm{sat}} = (38.378 - 0.1414\mathrm{P}^{0.5})^2$	0.9999959
	Saturated Vapour	$\rho_{v,\mathrm{sat}} = -371.336 + 372.316\exp\left\{\frac{P}{8230.56}\right\}$	0.9999995
Specific Heat [kJ/kg.K]	Subcooled Liquid	$C_{Pl} = 1.1527 + 0.1824\exp\left\{\frac{-\mathrm{T}}{62.569}\right\}$	0.9999528
	Saturated Liquid	$C_{Pl,sat} = 1.5364 + \left(0.00482\frac{P}{\ln(\mathrm{P})}\right)$	0.9999293
	Saturated Vapour	$ln(C_{Pv,sat}) = -0.304973 + 0.0018896\mathrm{P}^{0.5}\ln(P)$	0.9999316
Viscosity [µPas]	Subcooled Liquid	$\mu_l = 18.382 + 268.55\exp\left\{\frac{-\mathrm{T}}{77.425}\right\}$	0.9999945
	Saturated Liquid	$\mu_{l,sat} = (32.299 - 2.87848\ln(\mathrm{P}))^2$	0.9999916
	Saturated Vapour	$\mu_{v,sat} = (2.9554 - 0.02081\mathrm{P}^{0.5})^2$	0.9999128
Thermal Conductivity [mW/mK]	Subcooled Liquid	$\mathrm{k}_l = 93.443 - 0.4648\mathrm{T}^{0.99816}$	0.9999426
	Saturated Liquid	$\mathrm{k}_{l,\mathrm{sat}} = 1/[0.008661 + 2.11\mathrm{E}^{-5}P^{0.5}\ln(P)]$	0.9999232
	Saturated Vapour	$\mathrm{k}_{v,\mathrm{sat}} = 1/[0.17917 - 0.01662\ln(P)]$	0.9999789
Dielectric Constant	Liquid	9.51[3]	
	Vapour	1.053[3]	
Breakdown voltage		9-10 kV[4]	

[2] Dupont Correlations
[3] ASHRAE, 2001
[4] Cotton, 2000

Appendix B1: Flow Parameters and Energy Balance

The flow parameters chosen for these tests are shown in the table below. These flow parameters were chosen to maintain consistent stratified-wavy two phase flow pattern along the axial length of the test section with the liquid level is below the electrode. High voltage waveforms were applied to the electrode and the effects on flow pattern, heat transfer and pressure drop were investigated for both convective boiling (AC and DC) and convective condensation (DC only).

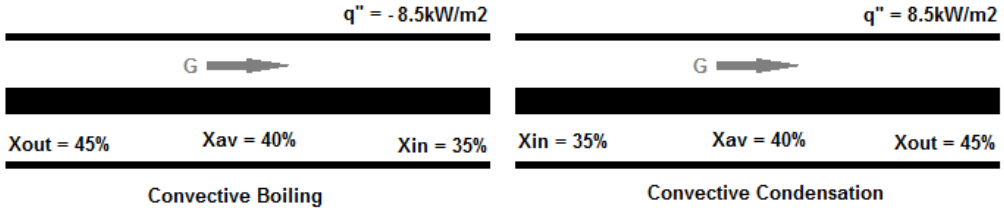

Flow Parameter	Description	Value
G	Mass Flux	60 kg/m^{2}s
q”	Test Section Applied Heat Flux	± 8.5 kW/m^2
Xav	Average Test Section Quality	40%
ΔX	Difference between inlet and outlet test section quality	10%
Tsat	Test Section Saturation Temperature	25 ^{o}C

The test rig was validated by repeating a convective condensation test: G=57 kg/m^{2}s, q” = 6 kW/m^2, Xav = 45%. Sadek, 2009, published a two fold increase in heat transfer coefficient and a corresponding five fold increase in the pressure drop for the current system geometry which matched the condensation test results conducted in this study.

Test Section Energy Balance

$$q''_{water} = q''_{ref}$$

$$\dot{m}_{water} C_{P,water} \Delta T_{water} = \dot{m}_{ref} C_{P,ref} \Delta T_{ref}$$

$$q''_{water} = (0.00538)(4.177)(2.1895) = 0.0492\ W$$

$$q''_{ref} = (0.0014477)(1.38437)(2.4835) = 0.049774\ W$$

$$\text{Difference} = 0.00057097 \text{ or } 1.16\%$$

Overall System Energy Balance Within 10%

Appendix B2:
Test Matrix

TEST MATRIX

G	Xav	ΔX	q"	Tsat	waveform	freq	duty cycle	# phases	mode h.t.	EHD	repeat	video
			-4					1			2	
variable	30	10%			DC			2	evap	effect of +8kV		
variable	40	10%			DC			2	evap	effect of +8kV		
variable	50	10%			DC			2	evap	effect of +8kV		
80	50	10%	-10		DC			2	evap	effect of DC		
80	50	10%	-10		square	60Hz	50%	2	evap	effect of offset, pk-pk = 2kV		
60	50	10%	-8		DC			2	evap	effect of DC & polarity		
60	40	0.1	8.5	25°C	DC			2	cond	effect of DC & polarity	3	yes
60	40	0.1	-8.5	25°C	DC			2	evap	effect of DC	4	yes
60	40	10%	-8.5	25°C	square	1kHz	0.5	2	evap	effect of offset, pk-pk = 2kV		
60	40	10%	-8.5	25°C	sine	1kHz	0.5	2	evap	effect of offset, pk-pk = 2kV		
60	40	10%	-8.5	25°C	square	200Hz	0.5	2	evap	effect of offset, pk-pk = 2kV		
60	40	10%	-8.5	25.5°C	sine	200Hz		2	evap	effect of offset, pk-pk = 2kV		
60	40	10%	-8.5	25.5°C	square	1kHz	0.5	2	evap	effect of offset, pk-pk = 4kV		
60	40	10%	-8.5	25.8°C	square	1kHz	0.5	2	evap	zero offset, effect of pk-pk		
60	40	10%	-8.5	24°C	square	variable	0.5	2	evap	effect of frequency, +8kV, zero offset		
60	40	10%	-8.5	24°C	sine	variable	0.5	2	evap	effect of frequency, +8kV, zero offset		
60	40	10%	-8.5	24.4°C	square	variable	0.5	2	evap	effect of frequency, +4kV offset, 4kV pk-pk		
60	40	10%	-8.5	24.8°C	sine	variable	0.5	2	evap	effect of frequency, +4kV offset, 4kV pk-pk		
60	40	10%	-8.5	25°C	square	variable	0.5	2	evap	effect of frequency, -8kV, zero offset		
60	40	10%	-8.5	24.4°C	pulse	200Hz	variable	2	evap	effect of duty, +8kV, zero offset		
60	40	10%	-8.5	24.4°C	pulse	200Hz	variable	2	evap	effect of duty, -8kV, zero offset		Veff
60	40	10%	-8.5	26.5°C	pulse	10Hz	variable	2	evap	effect of duty, +8kV, zero offset		
60	40	10%	-8.5	24.4°C	pulse	10Hz	variable	2	evap	effect of duty, -8kV, zero offset		
60	40	10%	-8.5	26.2°C	pulse	2Hz	variable	2	evap	effect of duty, -8kV, zero offset		yes

Appendix C: Uncertainty Analysis

The following uncertainty analysis was calculated in accordance with Kline and McClintock, 1973.

Measurement Uncertainty

The total uncertainty of any measured parameter is given as:

$$\delta x_i = \sqrt{(B)^2 + (P)^2}$$

Where B is the bias error as quoted by the manufacturer or independently calibrated.

P is the precision error or twice the standard deviation of the experimental measurements taken.

RTD Temperature Uncertainty, δT_{RTD}

Instrument: Automatic Systems Labs Platinum Probe RTD, T100-250-1

Bias Error

- Manufacturer Uncertainty ±0.01 °C
- Resolution of Omega DP-251 RTD Reader ±0.01 °C
- Drift in Accuracy of probe[5] ±0.0375 °C

Total Bias = $\sqrt{(0.01)^2 + (0.01)^2 + (0.0375)^2} = \pm 0.04\ ^0\text{C}$

Precision Error

2σ = ±0.084 °C

$$\delta T_{RTD} = \sqrt{(0.04)^2 + (0.084)^2} = \pm 0.09\ ^0\text{C}$$

Thermocouple Temperature Uncertainty, δT_{TC}

Instrument: Type T Calibrated thermocouples

Bias Error

- Uncertainty of RTD used for Calibration ±0.09 °C
- Uncertainty of TC after Calibration with RTD ±0.01 °C
- Uncertainty of Cold Junction: Ice Bath ±0.01 °C

[5] Assuming ±0.0075 °C/year drift for at least 5 years (Drnovsek, et al., 1998)

- Uncertainty of Cold Junction: Measurement Probe ±0.01 °C
- Uncertainty of Data Acquisition System ±0.20 °C

Total Bias = $\sqrt{3(0.01)^2 + (0.093)^2 + (0.195)^2} = \pm 0.2\ ^0\text{C}$

Precision Error

2σ = ±0.24 °C

$$\delta T_{TC} = \sqrt{(0.24)^2 + (0.22)^2} = \pm 0.326\ ^0\text{C}$$

Pressure Drop Uncertainty, δP

Instrument: Validyne DP-15 pressure transducers connected to 2-channel Validyne Signal Conditioner

Low Range Diaphragm [1.4 kPa], δP_{Low}

Bias Error

- Transducer Uncertainty ±3.5 Pa
- Calibrator Uncertainty ±10 Pa

Total Bias = $\sqrt{(3.5)^2 + (10)^2} = \pm 10.59\ Pa$

Precision Error

2σ = ±10 Pa

$\delta P_{LOW} = \sqrt{(10.59)^2 + (10)^2} = \pm 14.56$ Pa

High Range Diaphragm 3.5 kPa], δP_{HIGH}

Bias Error

- Transducer Uncertainty ±8.75 Pa
- Calibrator Uncertainty ±10 Pa

Total Bias = $\sqrt{(8.75)^2 + (10)^2} = \pm 13.3\ Pa$

Precision Error

2σ = ±18.4 Pa

$\delta P_{HIGH} = \sqrt{(13.3)^2 + (18.4)^2} = \pm 22.7$ Pa

Refrigerant Flowrate Uncertainty, $\delta \dot{m}_{ref}$

Instrument: Omega FTB-502 Turbine Flow Meter

Bias Error

- Instrument Accuracy (±0.05% of rdg) ±0.0000025 kg/s
- Instrument Repeatability (±0.25% of rdg) ±0.0000125 kg/s

Total Bias = $\sqrt{(2.5E^{-6})^2 + (1.25E^{-5})^2} = \pm 1.275\text{E}^{-5}\ kg/s$

Precision Error

2σ = ±0.0012 kg/s

$$\delta \dot{m}_{ref} = \sqrt{(1.275\text{E}^{-5})^2 + (0.0012)^2} = \pm 0.0012\ \text{kg/s}$$

Water Flowrate Uncertainty, $\delta\dot{m}_{water}$

Instrument: McMillan 104-Flo-sensor microturbine

Bias Error

- Instrument Uncertainty (1%% of FS) ±0.0003 kg/s
- Instrument Repeatability (±0.2% of FS) ±0.00006 kg/s

Total Bias = $\sqrt{(0.0003)^2 + (0.00006)^2} = \pm 0.0003\ kg/s$

Precision Error

2σ = ±0.0002 kg/s

$$\delta\dot{m}_{water} = \sqrt{0.0003^2 + (0.0002)^2} = \pm 0.00036\ \text{kg/s}$$

<u>Calculated Parameter Uncertainty</u>

The relative uncertainty of any calculated parameter is given as:

$$\delta f = \sqrt{\sum_{i=1}^{n} \left(\frac{\delta f}{\delta x}\delta x_i\right)^2}$$

Electrical Heater Uncertainty, $\delta QElec$

Voltage

DMS-20PC-2-RS series digital panel voltmeter: ±0.5% or rdg 3.5±0.0175 V

Electrical Heater Current

DCA5-20PC-6-DC4-R2 digital current meter: ±0.1% of rdg 53A±53 mA

$$\frac{\delta QElec}{QElec} = \sqrt{\left(\frac{\delta V}{V}\right)^2 + \left(\frac{\delta I}{I}\right)^2} = \sqrt{\left(\frac{0.0175}{3.5}\right)^2 + \left(\frac{0.053}{53}\right)^2} = 0.0051 = 0.51\%$$

Relative Uncertainty in Test Section Applied Heat Flux, δq"/q"

$$q" = \frac{\dot{m}_{water} C_{p,water} \Delta T_{RTD}}{\pi D_i L}$$

Neglecting the uncertainty in the test section diameter and length as well as the uncertainty associated with the Cp value as this is calculated from the temperature.

$$\frac{\delta q"}{q"} = \sqrt{\left(\frac{\delta \dot{m}_{water}}{\dot{m}_{water}}\right)^2 + \left(\frac{\delta \Delta T_{RTD}}{\Delta T_{RTD}}\right)^2}$$

$$= \sqrt{\left(\frac{0.00036}{0.025}\right)^2 + \left(\frac{0.093}{0.8}\right)^2}$$

$$= 11.7\%$$

Relative Uncertainty in heat transfer coefficient, δh/h

$$h = \frac{q"}{T_{sat} - T_{s,av}}$$

Where h is the inner tube heat transfer coefficient and $T_{s,av}$ is the average inner surface temperature in the test section. Note these thermocouples are embedded into the pipe wall and the conductive thermal resistance of the pipe wall is neglected.

$$\frac{\delta h}{h} = \sqrt{\left(\frac{\delta q"}{q"}\right)^2 + \left(\frac{\delta\left(T_{sat} - T_{s,av}\right)}{T_{sat} - T_{s,av}}\right)^2}$$

Where

$$\delta(T_{sat} - T_{s,av}) = \sqrt{(\delta T_{sat})^2 + \left(\delta T_{s,av}\right)^2}$$

And $\delta T_{s,av} = \frac{1}{\sqrt{12}}\,\delta T_s = \frac{1}{\sqrt{12}}\,(\pm 0.326^0\mathrm{C}) = \pm 0.094\ ^0C$

Therefore $\delta\left(T_{sat} - T_{s,av}\right) = \sqrt{(0.326)^2 + (0.094)^2} = \pm 0.339\ ^0C$

$$\frac{\delta h}{h} = \sqrt{(0.117)^2 + \left(\frac{0.339}{24.3 - 29.96}\right)^2}$$

$$= 13.15\%$$

Relative Uncertainty in test section inlet vapour quality, δXin/Xin

The inlet quality is calculated from the energy added to the subcooled single phase flow temperature.

$$X_{in} = \frac{\frac{QElec}{\dot{m}_{ref}} - C_{P,ref}(T_{sat} - T_{sub})}{h_{fg}}$$

Again we neglect the parameters $C_{P,ref}$ and h_{fg} as these are calculated from the temperature. So the relative uncertainty in inlet quality is as shown below:

$$\frac{\delta Xin}{Xin} = \sqrt{\left(\frac{\delta T_{sub}}{T_{sub}}\right)^2 + \left(\frac{\delta \dot{m}_{ref}}{\dot{m}_{ref}}\right)^2 + \left(\frac{\delta QElec}{QElec}\right)^2 + \left(\frac{\delta Qloss}{Qloss}\right)^2}$$

Where $\frac{\delta Qloss}{Qloss}$ is the uncertainty in the heat lost to the surroundings before the refrigerant reaches the test section. This value has been found from the system energy balance to be approximately ±3% of the added electrical heat value.

$$\frac{\delta Xin}{Xin} = \sqrt{\left(\frac{0.326}{17.7}\right)^2 + \left(\frac{0.0012}{0.0052}\right)^2 + (0.0051)^2 + (0.0000153)^2}$$

$$= 23.15\%$$

Appendix D: Dimensional Analysis

This dimensional analysis shows the relative importance of each of the components in the electric body force term compared to the other terms in the fluid momentum equations.

Conservation of momentum equation

$$\rho\frac{\partial\bar{u}}{\partial t}+\rho(\bar{u}\cdot\nabla)\bar{u}=\ -\rho\bar{g}\beta(T-T_0)-\nabla P+\mu\nabla^2\bar{u}+\bar{f}_{eB}$$

Where

$$\bar{f}_{eB}=\rho_{ei}\bar{E}-\frac{1}{2}E^2\nabla\varepsilon+\frac{1}{2}\nabla\left[\rho\mathrm{E}^2\left({}^{\partial\varepsilon}/_{\partial\rho}\right)_T\right]$$

Non dimensional parameters

$$\tilde{u}=\frac{\bar{u}}{u_0}\quad\tilde{P}=\frac{\bar{P}}{\rho_0u_0}\quad\theta=\frac{T}{T_0}\quad\tau=\frac{tu_0}{L}\quad\tilde{x}=\frac{x}{L}\quad\varepsilon_r=\frac{\varepsilon}{\varepsilon_0}\quad\eta=\frac{\bar{E}}{E_0}\quad\tilde{\nabla}=L\nabla$$

The momentum equation becomes

$$\frac{\rho{u_0}^2}{L}\left(\frac{\partial\tilde{u}}{\partial\tau}\right)+\frac{\rho{u_0}^2}{L}(\tilde{u}\cdot\ \tilde{\nabla})\tilde{u}=\ -\rho\bar{g}\beta(T_0\theta-T_0)-\frac{\rho{u_0}^2}{L}\left(\frac{\partial\tilde{P}}{\partial\tilde{x}}\right)+\frac{\mu u_0}{L^2}\left(\frac{\partial^2\tilde{u}}{\partial\tilde{x}^2}\right)$$

$$+\left\{\ \ \rho_{ei}E_0\eta-\frac{1}{2}E_0^2\eta^2\varepsilon_0\nabla\varepsilon_r+\frac{1}{2}\nabla\left[\rho{E_0}^2\eta^2\left({}^{\partial\varepsilon}/_{\partial\rho}\right)_T\right]\ \ \right\}$$

Dividing across by $\frac{\rho{u_0}^2}{L}$ (implicitly assumes viscous forces aren't important, rather convective/inertial terms and pressure is important) gauges the importance of EHD with respect to these terms

$$\left(\frac{\partial\tilde{u}}{\partial\tau}\right)+(\tilde{u}\cdot\ \tilde{\nabla})\tilde{u}=\ -\frac{\bar{g}\beta L}{{u_0}^2}(T_0\theta-T_0)-\left(\frac{\partial\tilde{P}}{\partial\tilde{x}}\right)+\frac{\mu}{\rho Lu_0}\left(\frac{\partial^2\tilde{u}}{\partial\tilde{x}^2}\right)$$

$$+\frac{L}{\rho{u_0}^2}\left\{\ \ \rho_{ei}E_0\eta-\frac{1}{2}E_0^2\eta^2\varepsilon_0\nabla\varepsilon_r+\frac{1}{2}\nabla\left[\rho{E_0}^2\eta^2\left({}^{\partial\varepsilon}/_{\partial\rho}\right)_T\right]\ \ \right\}$$

Looking at each EHD term

Electrophoretic term $\boldsymbol{\rho_{ei}\bar{E}}$

$$\frac{L}{\rho{u_0}^2}\ \rho_{ei}E_0\eta$$

Noting that $\rho_{ei} = \sigma_e/\mu_e$

$$\frac{L}{\rho {u_0}^2}\frac{\sigma_e}{\mu_e}E_0\eta$$

To compare against inertial effects we want the Reynolds number to be included

$$Re = \frac{u_0 L}{\nu}$$

$$\frac{L}{\rho {u_0}^2}\frac{\sigma_e}{\mu_e}E_0\eta = \frac{1}{Re^2}\frac{\sigma_e}{\mu_e}\frac{E_0 L^3 \eta}{\nu^2 \rho}$$

Define the EHD number

$$E_{hd} = \frac{\sigma_e E_0 L^3}{\mu_e \nu^2 \rho} = \frac{I_0 L^3}{\mu_e \nu^2 \rho A}$$

Since

$$\sigma_e E_0 = J_0 = I_0/A$$

Term becomes

$$\boxed{\left(\frac{E_{hd}}{Re^2}\right)\eta}$$

Dielectrophoretic term $-\frac{1}{2}\boldsymbol{E^2\nabla\varepsilon}$

$$-\frac{L}{2\rho {u_0}^2}E_0^2\eta^2\varepsilon_0\nabla\varepsilon_r$$

$$\nabla\varepsilon_r = \left(\frac{\partial\varepsilon}{\partial T}\right)_\rho \nabla T + \left(\frac{\partial\varepsilon}{\partial\rho}\right)_T \nabla\rho$$

Assuming constant density - $\nabla\rho = 0$ and multiplying across by ν^2/ν^2

$$= -\frac{L}{2\rho {u_0}^2}E_0^2\eta^2\varepsilon_0\left[\left(\frac{\partial\varepsilon}{\partial T}\right)_\rho \nabla T\right]\frac{\nu^2}{\nu^2}$$

Using dimensionless parameters

$$= -\frac{\nu^2 L}{2\rho {u_0}^2\nu^2}E_0^2\eta^2\varepsilon_0\left[\left(\frac{\partial\varepsilon}{\partial T}\right)_\rho T_0\frac{\partial\theta}{\partial\tilde{x}}L\right]$$

$$= -\frac{1}{Re^2}\left(\frac{E_0^2 \varepsilon_0 T_0 L^2 \left(\frac{\partial \varepsilon}{\partial T}\right)_\rho}{2\rho\nu^2}\right)\eta^2 \widetilde{\nabla}\theta$$

Define the Masuda number

$$M_d = \frac{E_0^2 \varepsilon_0 T_0 L^2 \left(\frac{\partial \varepsilon}{\partial T}\right)_\rho}{2\rho\nu^2}$$

Term becomes

$$\boxed{\left(\frac{M_d}{Re^2}\right)\eta^2 \widetilde{\nabla}\theta}$$

Electrostrictive term $\frac{1}{2}\nabla\left[\mathbf{E}^2\left(\partial\boldsymbol{\varepsilon}/\partial\boldsymbol{\rho}\right)_{\boldsymbol{T}}\right]$

$$\frac{L}{2\rho {u_0}^2}\nabla\left[\rho {E_0}^2 \eta^2 \left(\partial\varepsilon/\partial\rho\right)_T\right]$$

Using the approximation from (Landau amd Lifshitz 1960

$$\rho\left(\partial\varepsilon/\partial\rho\right)_T \sim \varepsilon_0\left(\partial\varepsilon/\partial T\right)_\rho T$$

$$\frac{L}{2\rho {u_0}^2}\nabla\left[{E_0}^2 \eta^2\, \varepsilon_0\left(\partial\varepsilon/\partial T\right)_\rho T_0\theta\right]$$

Multiplying by $L^2\nu^2/L^2\nu^2$

$$\frac{1}{Re^2}L\nabla\left[\frac{E_0^2 \varepsilon_0 T_0 L^2\left(\frac{\partial\varepsilon}{\partial T}\right)_\rho}{2\rho\nu^2}\theta\eta^2\right]$$

$$\boxed{\left(\frac{M_d}{Re^2}\right)\widetilde{\nabla}(\theta\eta^2)}$$

Final form of the dimensionless Navier-Stokes equations is

$$\frac{\partial\tilde{u}}{\partial\tau} + \tilde{u}\cdot\widetilde{\nabla}\tilde{u} = \frac{Gr}{Re^2}(\theta - 1) - \widetilde{\nabla}p + \frac{1}{Re^2}\widetilde{\nabla}^2\tilde{u} + \frac{E_{hd}\eta - M_d\eta^2\widetilde{\nabla}\theta + M_d\widetilde{\nabla}(\theta\eta^2)}{Re^2}$$

where

$$Gr = \frac{\bar{g}\beta(T - T_0)L^3}{\nu^2}$$

Appendix E: The Effect of DC Applied Voltage; Condensation and Comparison

This appendix outlines the effect of DC applied voltage on the convective condensation of R134a in a horizontal, counter-current heat exchanger and also compares this with the similar case for convective boiling as discussed in Chapter 4. The pre-EHD flow conditions are such that a stratified wavy flow pattern with the liquid interface below and close to the electrode, exists i.e. Mass flux = 60 kg/m^{2}s, Applied heat flux = +9 kW/m^2, Average vapour quality = 40% with a 10% differential between inlet and outlet. The evolution of the flow pattern redistribution for convective condensation is similar to that in the case of convective evaporation except there will always a thin, condensing film exists at much higher flow qualities on the top tube surface, i.e. the heat transfer surface in condensation.

E.1 The Effect of EHD on Convective Condensation Heat Transfer and Pressure Drop

Figures E.1 and E.2 show the results for varying DC applied voltage level on heat transfer and pressure drop for convective condensation. It should be noted that the twofold enhancement of heat transfer coefficient and associated threefold increase in pressure drop due to EHD agrees with that found in experiments conducted by previous researchers (Sadek, 2009), (Ng, 2010).

For condensation, it appears that the enhancement of heat transfer is slightly greater for the positive voltages than it is for the negative voltages, Figure E.1. This is the opposite of what was seen for the convective boiling tests in chapter 4 but agrees with the convective condensation tests conducted by Ng, 2010. The positive applied voltage attracts more liquid into the core region drying the heat transfer surface. This is advantageous in condensation as it is easier to condense fluid onto a dry heat transfer surface but less efficient in boiling where maximum enhancement occurs when the entire heat transfer is wet. The opposite is true for the case of negative applied voltage, where more liquid is repelled toward the heat transfer surface. This is suitable for boiling as it rewets the heat

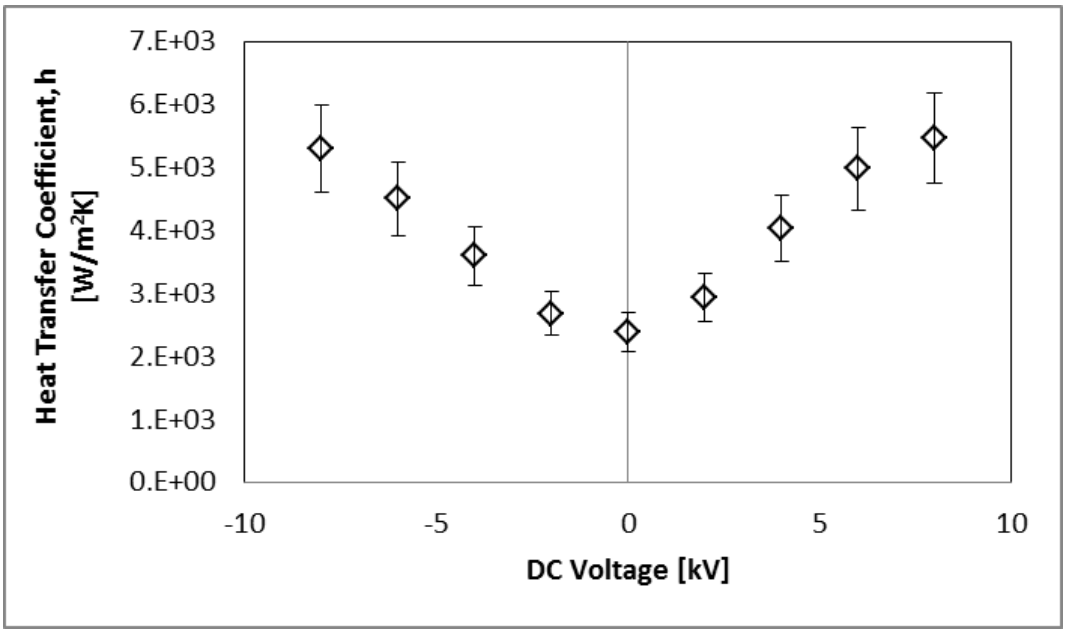

Figure E.1: The Effect of DC Applied Voltage on Convective Condensation Heat Transfer. G = 60kg/m^{2}s, q" = 8.5kW/m^2, Xav = 40%

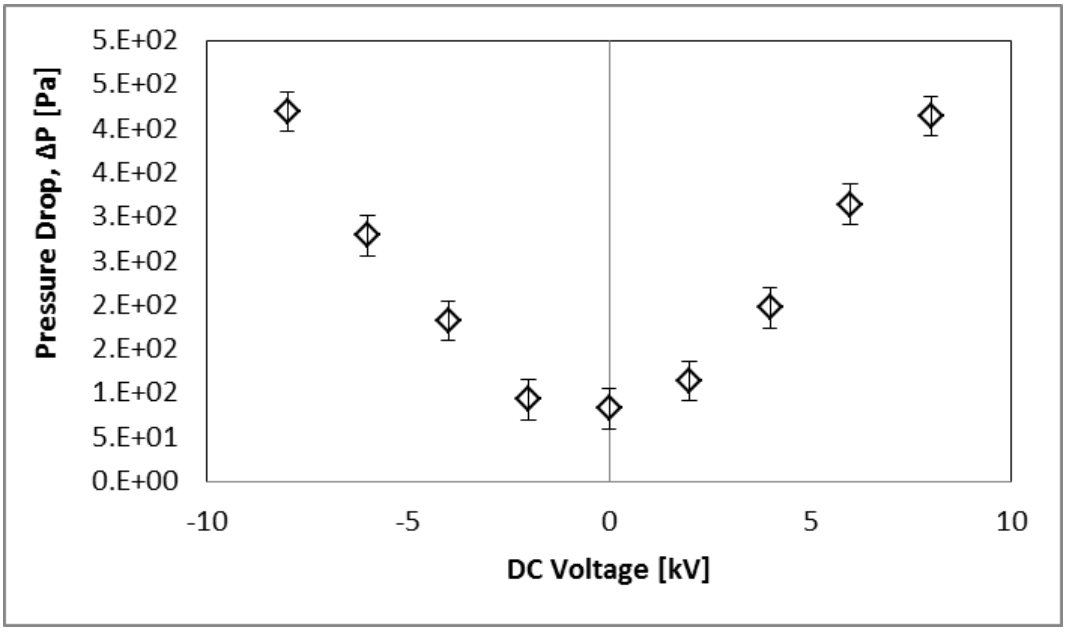

Figure E.2: The Effect of DC Applied Voltage on Convective Condensation Pressure Drop. G = 60kg/m^{2}s, q" = 8.5kW/m^2, Xav = 40%

transfer surface, whereas it is less suitable for condensation as it is more difficult to condense liquid on a surface that is already wet.

From Figure E.2 the pressure drop is seen to increase with increasing applied voltage. This is likely to be due to the increased mixing in the system induced by EHD with increasing voltage. Flow redistribution due to EHD can cause intermittency in the flow pattern which can increase the acceleration component of the two phase pressure drop. In addition, uptake into the core region means there will be an additional growing hydrodynamic boundary layer as liquid flows along the electrode surface and this will also greatly increase the test section pressure drop. When high voltages are applied, there will be significant disturbance of both the thermal and hydrodynamic boundary layers in the system due to the large gradient of permittivity in these regions. Figure 4.7 shows the location of these boundary layers, magnified for clarity. The heat transfer surface is the outer tube so this will have produce a circumferential thermal and hydrodynamic boundary layer, whereas the electrode only has a hydrodynamic boundary layer due to the flow travelling across it. Disturbance of the thermal boundary layer can enhance heat transfer and disturbance of hydrodynamic boundary layer can cause additional pressure drop.

In Figure E.2, there is no discernible difference in the pressure drop for different polarities. There is pressure drop due to new flow patterns induced by EHD and there is pressure drop that occurs due to flow along the pipe, along the electrode and due to the spacers holding the electrode in place. The latter pressure drop is the most dominant pressure drop in the system and therefore the pressure drop due to different flow patterns associated with positive and negative polarities can be masked by this. The difference in pressure drop with polarity is less marked than in the case of that for evaporation, see Figure 4.7. It is possible that this is because the differences in flow pattern between positive and negative polarities are not as dissimilar in the case of condensation compared to evaporation. This is because of the existence of the annular type flow pattern due to the condensing liquid on the top surface, which is not found in evaporation experiments.

Figures E.3 and E.4 show the repeatability for these DC applied voltage experiments. There is some variance in the heat transfer results at positive, high applied voltages which may be in part due to the high value of the heat transfer coefficient and associated relative error with this calculated parameter and also due to proximity to a flow pattern transition

region, as discussed in chapter 4. However the variation in the condensation results shown here are not as marked as for the evaporation results in Figure 4.12 for the negative voltages. This is likely attributed to the fact that there is a liquid film present on the top surface in condensation whereas this only exists when the interfacial force is high enough for the -8kVDC evaporation case. Near transition regions, small changes in flow parameters such as quality or mass flux can result in different liquid levels and consequently slight variations in the enhancement achievable through EHD.

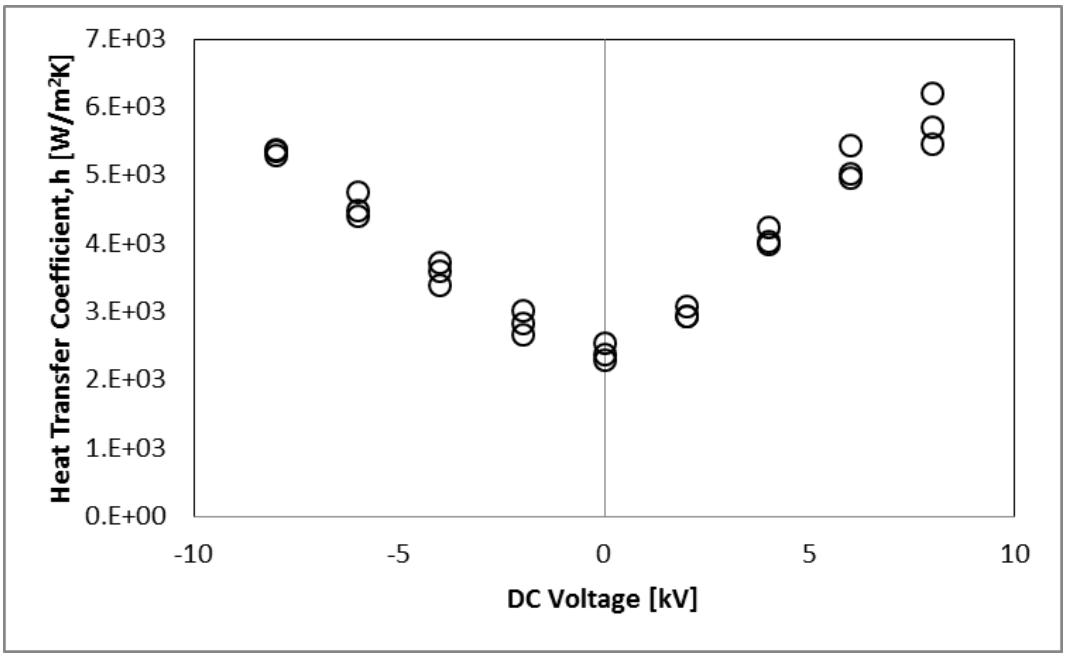

Figure E.3: Repeatability of DC Voltage Effects on Convective Condensation Heat Transfer

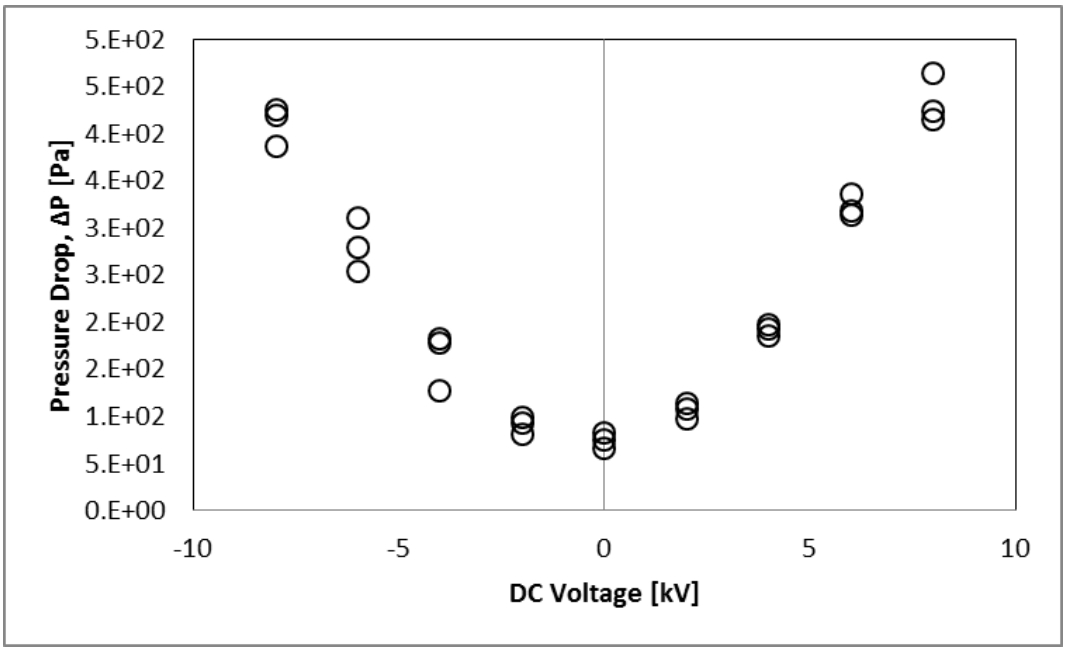

Figure E.4: Repeatability of DC Voltage Effects on Convective Condensation Pressure Drop

E.2 Localised Flow Redistribution

The local flow redistribution is seen via flow visualisation, Figure E.7, and surface temperature data, Figure E.5. The main difference between the condensation and boiling flow patterns is that there exists a thin film of fluid on the top surface of the tube up to very high flow qualities, i.e. the flow is almost always annular.

The flow patterns produced for the condensation tests are almost identical to those in the case of evaporation except for the thin film of liquid on the top surface, Figure E.7 & Figure 4.11. For this reason, it can be difficult to establish the flow pattern. The surface temperature profiles for the cases of no EHD, +8kVDC and -8kVDC applied voltage are shown in Figure E.5. The no EHD case has a top heat transfer coefficient of approximately 3000 W/m^2K and the bottom has 1500 W/m^2K. This bottom value is comparable to that seen for the bottom in the convective boiling case, 2000 W/m^2K but the top heat transfer coefficient in condensation is far higher as the mechanism of heat transfer on the top surface is falling film condensation which is a very effective mechanism of heat transfer.

The +4kV case, as seen via flow visualisation in Figure E.7, remains stratified wavy except there are liquid droplets formed and there is some uptake into the core. The heat transfer coefficient on the top surface has increased to approximately 4800 W/m^2K and the bottom has increased to approximately 3200 W/m^2K. This is likely due to the thinning of the liquid films on the heat transfer surface due to the liquid uptake. The -4kV produces a slug-type flow regime where liquid is periodically expelled to the top surface when the waviness is high enough. The heat transfer coefficients are approximately 4700 W/m^2K and 3000 W/m^2K for the top and bottom surfaces respectively which are slightly lower than for the positive 4kV case. This is due to the rewetting caused by negative polarities being less suitable for convective condensation applications.

The +8kV case induces a lot of liquid uptake into the core and liquid droplets regularly impinge the heat transfer surface. The twisted liquid cone structures associated with high positive DC voltages (Sadek, 2009), (Ng, 2010) are seen in Figure E.7. The heat transfer coefficients have increased to approximately 5800 W/m^2K and 8000 W/m^2K for the top and bottom respectively, due to liquid uptake into the core region. It is likely that the high value for the bottom surface is due to the turbulent nature of the twisted liquid cone structures coupled with the forced convection in the flow. The -8kVDC case induces an

annular flow regime through high liquid repulsion forces. Remnants of the twisted liquid column flow structures (Ng, 2010) can be seen underneath the electrode for this case. The heat transfer coefficients are approximately 5300 W/m^2K and 7500 W/m^2K for the top and bottom surfaces respectively, slightly lower than those seen in the positive case as positive voltages are more suitable for condensation heat transfer enhancement.

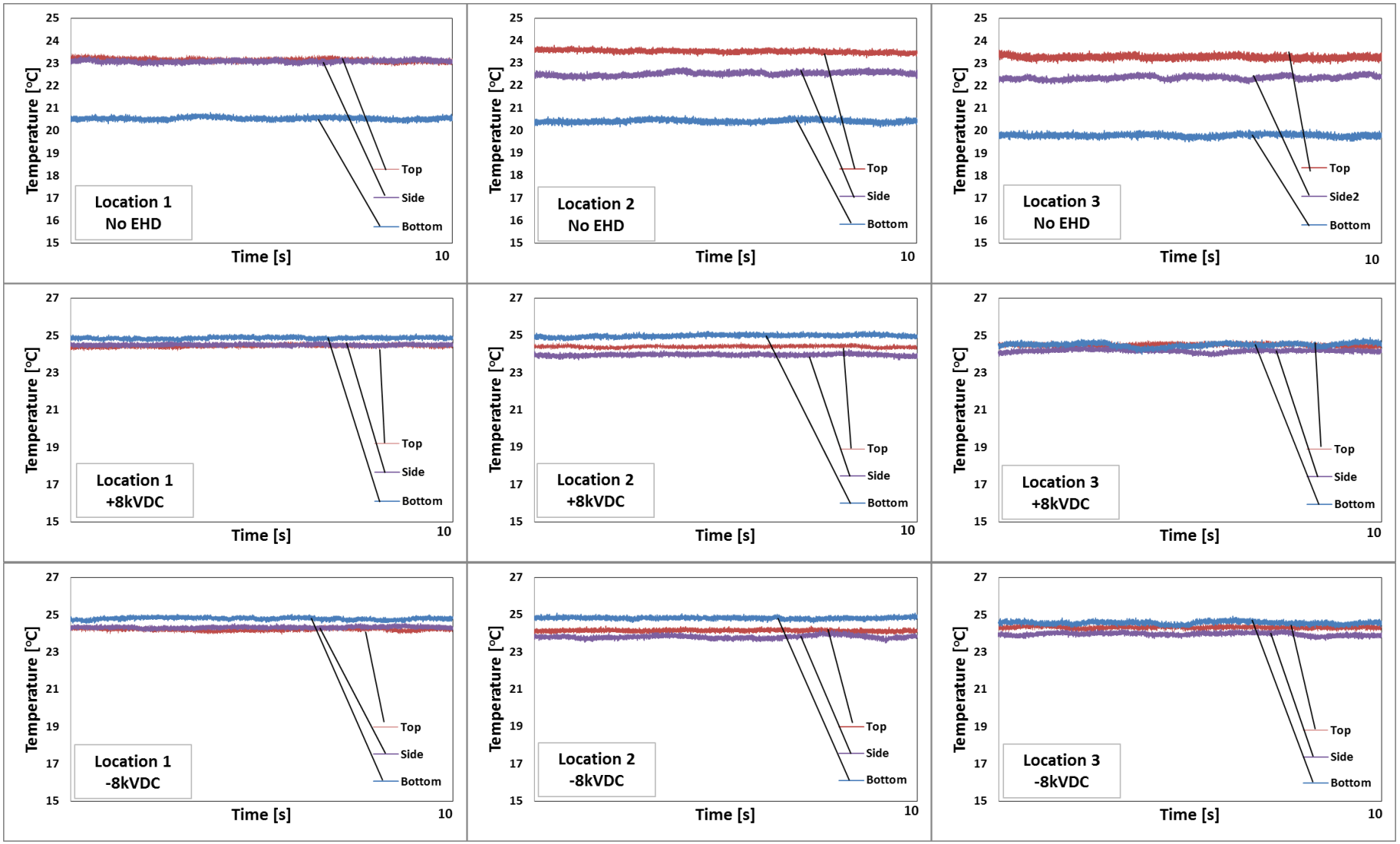

FigureE.5: Convective Condensation Temporal Surface Temperature Profiles for Varying Applied DC Voltage, G = 60kg/m^{2}s, q" = 8.5kW/m^2, Xav = 40%

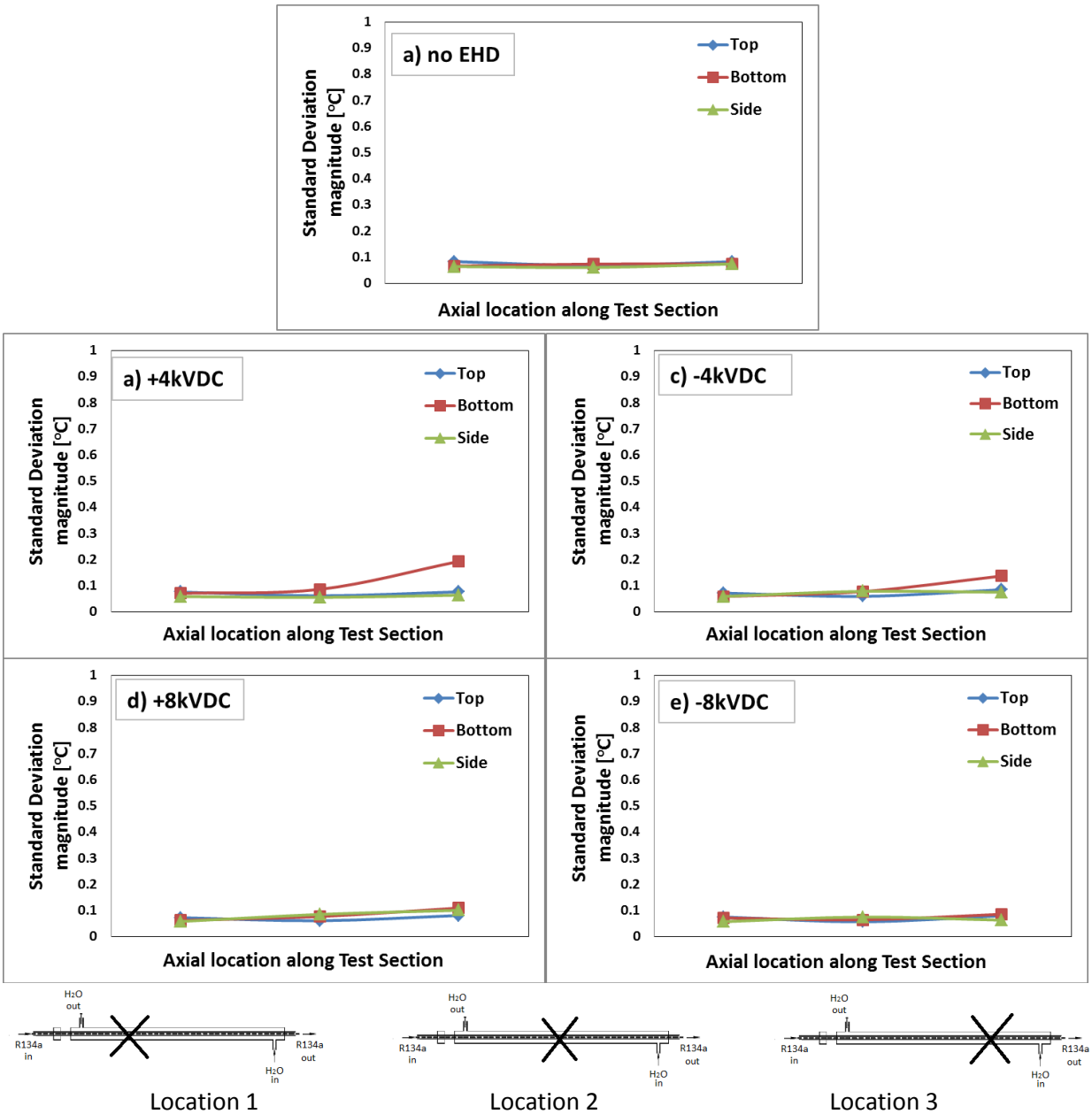

Figure E.6: Surface Temperature Standard Deviations for Varying Applied Voltage on Convective Condensation G = 60kg/m2s, q" = 8.5kW/m2, Xav = 40%

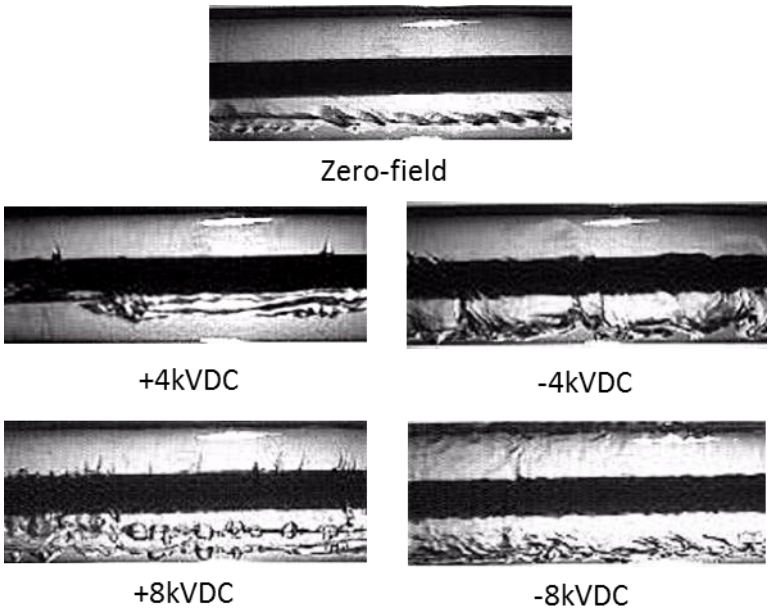

Figure E.7: Effect of DC Voltage on Convective Condensation Flow Visualisation G = 60kg/m2s, q" = 8.5kW/m2, Xav = 40%

It should be noted that the top heat transfer coefficients up to ±4kVDC are higher than those for the bottom in convective condensation. This is due to the highly efficient mechanism of dropping thin film heat transfer on this surface which has a higher heat transfer coefficient than the convective slow heat transfer mechanism occurring on the bottom surface. In the case of evaporation, the top surface heat transfer coefficient is actually lower than the bottom convective coefficient and this is due to the poor heat transfer mechanism of convection through a vapour with some suspended liquid droplets. However for the ±8kV DC applied voltages the bottom heat transfer coefficient is higher than the top for both evaporation and condensation. This is likely due to the thin liquid flow on the bottom surface, caused by liquid uptake into the core, couple with the turbulent nature of the EHD flow structures. Both of these contribute to in enhancement of convective flow heat transfer.

Figure E.8 shows a direct comparison of the heat transfer enhancement ratio for evaporation and for condensation. The heat transfer enhancement ratio is relative to the no EHD case. The effect of polarity on the enhancement of both cases is apparent with negative voltages being more suitable for convective boiling heat transfer and positive voltages for convective condensation heat transfer. The reason for this has been explained through the mechanism of liquid repulsion.

It is more difficult to determine the flow pattern through surface temperature techniques for condensation because most of the surfaces are wet and therefore the temperature values will be quite close in value. However in Figure E.5 we can see a stratified wavy flow regime with a smaller temperature difference between the top and side temperatures. In the first third of the test section they are almost identical and this is because the quality is lower so there is less wetting of the sides and therefore the liquid film in these locations is thinner. For the -8kV we can see the induced annular flow pattern and again the differences in temperatures are a function of the thermal resistance of the liquid film thickness in these localised regions of the tube.

The standard deviations of the heat transfer surface temperatures, as shown in Figure E.6, can provide some more insight into the flow pattern occurring in each test. In general the standard deviations are very similar as most of the tube is occupied by a flowing liquid. The top and sides at low/no EHD cases have a lowest deviation as the flow is in film form on the heat transfer surface. The ±4kVDC show the beginning of a deviation in the bottom surface temperature due to the intermittent flow pattern that is established. For the ±8kV case the deviation again reduces and this is due to the induced annular flow pattern due to uptake into the core region. Due to condensation and this uptake of liquid, the heat transfer surface is completely wet and therefore the standard deviation of temperature is small.

Finally Figure E.9 shows a comparison of the pressure drop penalty for evaporation and condensation tests. It appears that at low applied voltages there is a larger discrepancy in the pressure drop between condensation and evaporation but they merge closer in value at higher voltages. This may also be explained by the flow pattern. At low voltages the flow patterns are quite different between condensation and evaporation due to the presence of the liquid film on the top surface for the case of condensation. This difference is likely the reason for the discrepancy in the pressure drop at these low voltage data points. At higher voltages, the effect of EHD is more dominant and this determines the flow redistribution in the tube. Therefore at higher voltages, the flow patterns for condensation and evaporation cases are more similar and therefore the associated pressure drop will be closer in value.

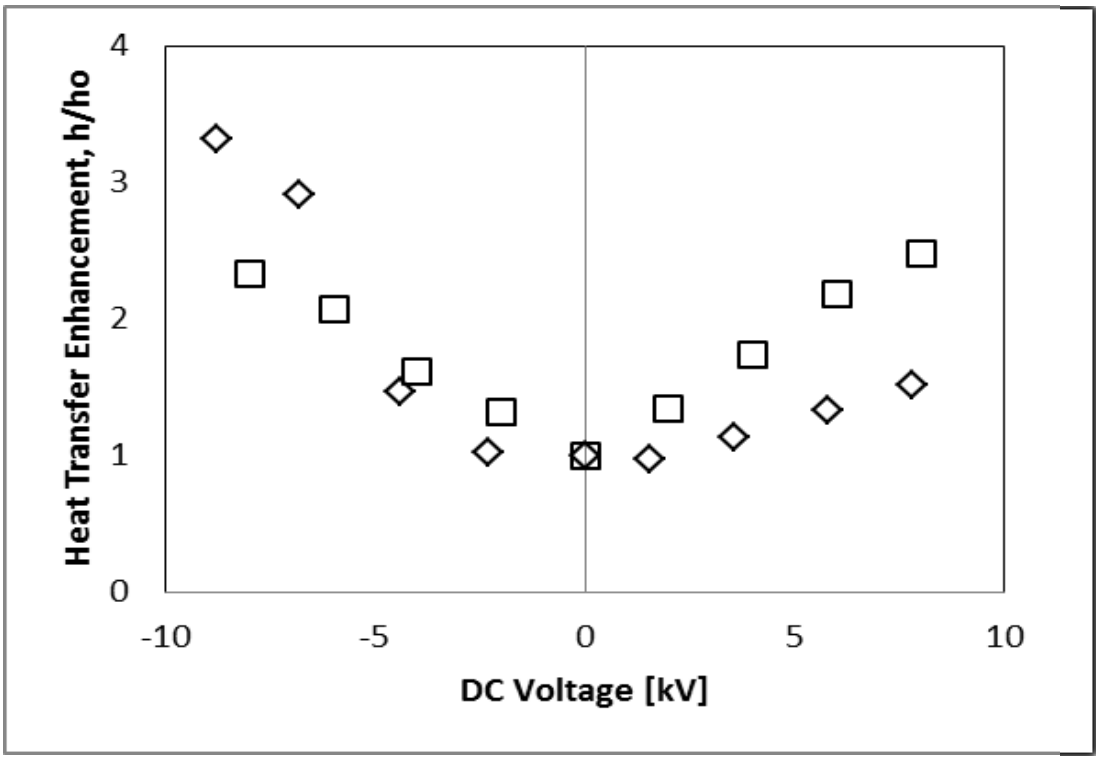

Figure E.8: Heat Transfer Enhancement Comparison: The Effect of DC Applied Voltage.
G = 60kg/m^{2}s, q" = ±8.5kW/m^2, Xav = 40%. ◊ Evaporation □ Condensation

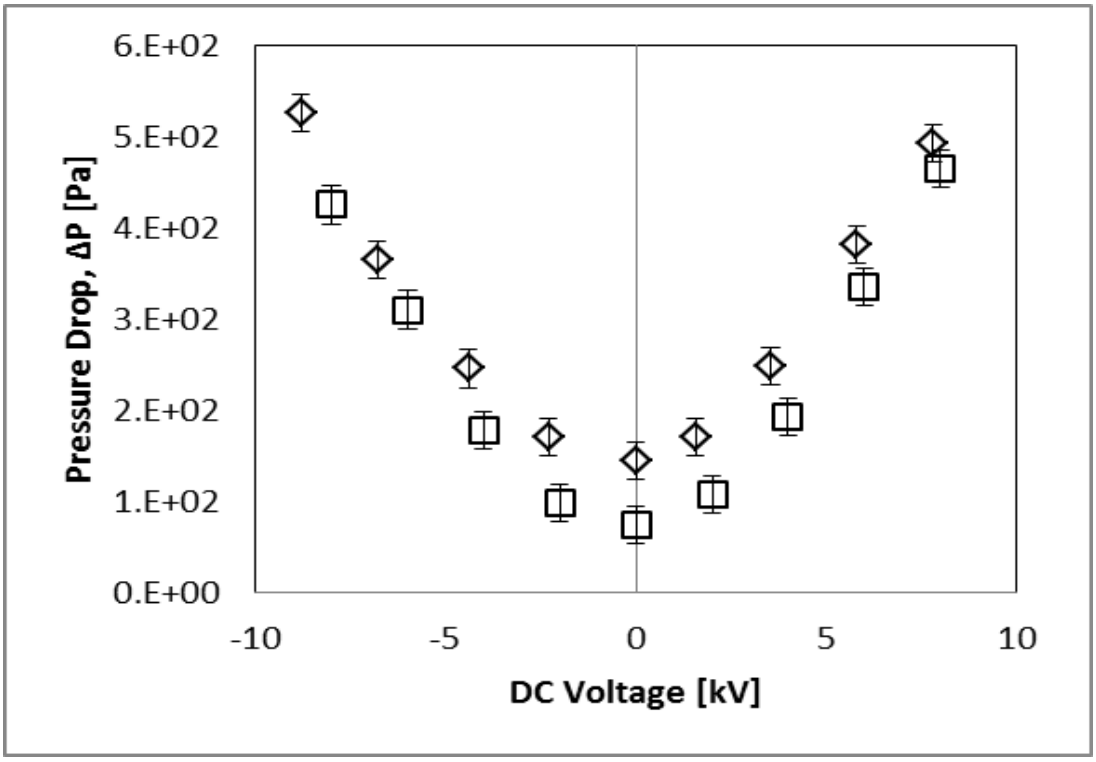

Figure E.9: Pressure Drop Comparison: The Effect of DC Applied Voltage.
G = 60kg/m^{2}s, q" = ±8.5kW/m^2, Xav = 40%. ◊ Evaporation □ Condensation

References

Allen, P. & Cooper, P., 1987. The potential of electrically enhanced evaporators. *Proc. 3rd Int. Symp. on the large scale application of heat pumps, Oxford, UK*, pp. 221-229.

Allen, P. & Karayiannis, T., 1995. Review Paper: Electrohydrodynamic enhancement of heat transfer and fluid flow. *Heat Recovery Systems & CHP*, 15(5), pp. 389-423.

ASTM STP 470, 1970. *Manual on the use of Thermocouples in Temperature Measurement, STP 470.* s.l.:ASTM.

Atten, P., McCluskey, A. & Lahjomri, A., 1987. The electrohydrodynamic origin of turbulence in electrostatic precipitators. *IEEE trans. Ind. Appl. IA-23*, pp. 705-711.

Berghmans, J., 1976. Electrostatic fields and the maximum heat flux. *Int. Journal of Heat and Mass Transfer*, Volume 19, pp. 791-797.

Bergles, A., 2011. Recent Developments in Enhanced Heat Transfer. *Heat Mass Transfer,* Volume 47, pp. 1001-1008.

Bochirol, L., Bonjour, E. & Weil, L., 1960. Exchanges thermiques-etude de l'action de champs electriques sur les transferts de chaleur dans les liquids bouillants. *C.R. Heb. des Seances de l'Acad. des Sciences (Paris)*, Volume 250, pp. 76-78.

Bonjour, E., Verdier, J. & Weil, L., 1962. Electroconvection effects on heat transfer. *Chem. Engng Progr.*, 58(7), pp. 63-66.

Bryan, J. & Seyed-Yagoobi, J., 2000. Electrohydrodynamically Enhanced Convective Boiling: Relationship between Electrohydrodynamic Pressure and Momentum Flux Rate. *Trans. of the ASME,* Volume 122, pp. 266-277.

Bryan, J. & Seyed-Yagoobi, J., 2001. Influence of Flow Regime, Heat Flux, and Mass Flux on Electrohydrodynamically Enhanced Convective Boiling. *Journal of Heat Transfer,* Volume 123, pp. 355-367.

Carey, V., 1992. *Liquid-Vapor Phase-Change Phenomena.* s.l.:Taylor & Francis.

Castellanos, A., 1998. *Electrohydrodynamics.* 1st ed. New York: Springer-Verlag.

Chang, J. & Watson, A., 1994. Electromagnetic Hydrodynamics. *IEEE Transactions on Dielectrics and Electrical Insulation,* 1(4), pp. 871-895.

Cheung, K., Ohadi, M. & Dessiatoun, S., 1995. Compound Enhancement of Boiling Heat Transfer of R134a in a tube bundle. *ASHRAE Trans.,* 101(1), pp. 1-11.

Chu, B., 1959. Thermodynamics of Electrically Conducting Fluids. *The Physics of Fluids,* 2(5), pp. 473-484.

Chubb, L., 1916. *Improvements relating to methods and apparatus for heating liquids.* UK.

Coelho, R., 1979. *Physics of Dielectrics for the Engineer.* New York: Elsevier Scientific Publishing Company.

Collier, J., 1973. Convective Boiling and Condensation. In: 2nd ed. s.l.:McGraw-Hill, New York.

Cooper, P., 1986. *Electrically Enhancement heat transfer in the shell/tube heat exchanger, PhD Thesis.* s.l.:University of London.

Cooper, P., 1990. EHD enhancement of nucleate boiling. *Trans. ASME, J. Heat Transfer,* Volume 112, pp. 458-464.

Cooper, P., 1992. *Practical Design Aspects of EHD Heat Transfer Enhancement in Evaporators.* Anaheim,CA, s.n., pp. 445-454.

Cotton, J., 2000. *PhD thesis: Mechanisms of Electrohydrodynamic flow and heat transfer in horizontal convective boiling channels.* s.l.:s.n.

Cotton, J., 2009. Electrohydrodynamic Condensation Heat Transfer Mechanisms under DC and AC applied voltages in a Horizontal Annular Channel. *IEEE Transactions on Dielectrics and Electrical Insulation (EHD Special Issue),* pp. 495-503.

Cotton, J. et al., 1998. Mechanisms of Electrohydrodynamic Flow Boiling Heat Transfer in Coaxial Flow Channels of Dielectric Refrigerant R-134a. *IEEE,* pp. 178-181.

Cotton, J., Robinson, A., Shoukri, M. & Chang, J., 2005. A two-phase flow pattern map for annular channels under a DC applied voltage and the application to electrohydrodynamic convective boiling analysis. *Int. Journal of Heat and Mass Transfer*, 48(25-26), pp. 5563-5579.

Cotton, J., Shoukri, M. & Chang, J., 2001. Oscillatory entrained droplet EHD two-phase flow. *Transactions of the ASME. Journal of Heat Transfer,* 123(4), p. 622.

Darabi, J., Salehi, M., Saeedi, M. & Ohadi , M., 1995. Review of available correlations for prediction of flow boiling heat transfer in smooth and augmented tubes. *ASHRAE transactions n 1*, pp. 965-975.

Di Bari, S. & Robinson, A., 2009. *Experimental Study of Bubble Growth from a Submerged Orifice considering the Dynamic Pressure Field.* Florianopolis-SC-Brazil, s.n.

Drnovsek, J., Pusnik, I. & Bojkovski, J., 1998. Reduction of uncertainties in temperature calibrations by comparison. *Measurement Science and Technology,* 9(11), pp. 1907-1911.

Eames, I. & Sabir, H., 1997. Potential benefits of electrohydrodynamic enhancement of two-phase heat transfer in the design of refrigeration systems. *Applied Thermal Engineering*, 17(1), pp. 79-92.

El Hajal, J., Thome, J. & Cavallini, A., 2003. Condensation in horizontal tubes, part 1 & part 2. *Int. Journal of Heat and Mass Transfer,* Volume 46, pp. 3349-3387.

Faghri, A. & Zhang, Y., 2006. *Transport Phenomena in multiphase systems with phase change.* s.l.:Elsevier.

Feng, Y. & Seyed-Yagoobi, J., 2003. Mechanism of Annular Two Phase Flow Heat Transfer Enhancement and Pressure Drop Penalty in the Presence of a Radial Electric Field - Turbulence Analysis. *Journal of Heat Transfer,* Volume 125, pp. 478-486.

Fernandez, J. & Poulter, R., 1987. Radial Mass Flow in Electrohydrodynamically-Enhanced Forced Heat Transfer in Tubes. *Int. J. Heat Mass Transfer,* 30(10), pp. 2125-2136.

Fujino, T. & Mori, Y., 1987. The Effect of a Transverse Electric Field on Laminar Channel Flow With a Constant Heat Rate. *Flow Visualisation IV,* pp. 643-648.

Fujino, T., Yokoyama, Y. & Mori, Y., 1989. Augmentation of Laminar Forced Convective Heat Transfer by the Application of a Transverse Electric Field. *ASME J. Heat Transfer,* Volume 111, pp. 345-351.

Fukuma, M., Nagao, M., Kosaki, M. & Kohno, Y., 2000. *Measurements of Conduction Current and Electric Field Distribution up to Electrical Breakdown in Two-Layer Polymer Film.* s.l., s.n., pp. 721-724.

Gidwani, A., Molki, M. & Ohadi, M., 2002. EHD-Enhanced Condensation of Alternative Refrigerants in Smooth and Corrugated Tubes. *HVAC&R Research,* 8(3), pp. 219-237.

Groeneveld, D., 1973. *Post dryout heat transfer at reactor operating conditions,* s.l.: s.n.

IEEE-DEIS-EHD, T. C., 2003. *Recommended International Standard for Dimensionless parameters used in Electrohydrodynamics.* s.l.:IEEE Transactions on Dielectrics and Electrical Insulation.

Jayanti, S. & Hewitt, G., 1997. hydrodynamics and heat transfer of wavy thin film flow. *Int. J. of Heat and Mass Transfer,* 40(1), pp. 179-190.

Jones, T., 1978. Electrohydrodynamically enhanced heat transfer in liquid - a review. *Adv. Heat Transfer,* Volume 14, pp. 107-148.

Kakac, S., Bergles, A. & Fernandes, E., 1988. *Two-Phase Flow Heat Exchangers: Thermal-Hydraulic Fundamentals and Design.* s.l.:Kluwer Academic Publishers.

Kattan, N., Thome, J. & Favrat, D., 1998. Flow Boiling in Horizontal Tubes part 1 & part 3. *Journal of Heat Transfer*, Volume 120.

Kedzierski, M. & Kim, M., 1998. Convective Boiling and Condensation Heat Transfer with a Twisted-Tape Insert for R12, R22, R152a, R134a, R290,R32/R134a, R32/R152a, R290/R134a, R134a/R600a.. *Thermal Science and Engineering,* 6(1), pp. 113-1201.

Khanpara, J. & Bergles, A., 1986. Augmentation of R-113 In-Tube Evaporation with micro-fin tubes. *ASHRAE Transactions,* 92(2B), pp. 506-524.

Khanpara, J., Bergles, A. & Pate, M., 1986. Augmentation of R-113 In-Tube Condensation with Micro-Fin Tubes. *ASME, Heat Transfer Div. Publication ,* Volume 65, pp. 21-32.

Kline, S. & McClintock, F., 1953. Describing Uncertainties in single-sample Experiments. *Mechanical Engineering,* 75(1), pp. 3-8.

Kuffel, E., Zaengl, W. & Kuffel, J., 2000. *High Voltage Engineering: Fundamentals.* 2nd ed. Oxford: Butterworth-Heinemann.

Laohalertdecha, S., Kaew-On, J. & Wongwises, S., 2010. The Effect of the Electrohydrodynamic on the Two-Phase Flow Pressure Drop of R-134a during Evaporation inside Horizontal Smooth and Micro-Fin Tubes. *Heat Transfer Engineering,* 31(2), pp. 108-118.

Laohalertdecha, S., Naphon, P. & Wongwises, S., 2007. A review of electrohydrodynamic enhancement of heat transfer. *Renewable and Sustainable Energy reviews*, Volume 11, pp. 858-876.

Liu, Y., Li, R., Wang, F. & Yu, H., 2005. The effect of electrode polarity on EHD enhancement of boiling heat transfer in a vertical tube. *Experimental Thermal and Fluid Science,* Volume 29, pp. 601-608.

Liu, Z. & Winterton, R., 1991. A General Correlation for Saturated and Subcooled Flow Boiling in Tubes and Annuli Based on Nucleate Pool Boiling. *Int. J. Heat and Mass Transfer,* Volume 34, pp. 2759-2765.

Mahmoudi, S. R., 2012. *Electrohydrodynamic Enhancement of Heat Transfer and Mass Transport in Gaseous Media, Bulk Dielectric Liquids and Dielectric Thin Liquid Films.* London: s.n.

Martin, P. & Richardson, A., 1984. Conductivity Models of Electrothermal Convection in a Plane Layer of Dielectric Liquid. *ASME Journal of Heat Transfer,* Volume 106, pp. 131-136.

McGranaghan, G., Cotton, J. & Robinson, A., 2012. *EHD Augmented Heat Transfer of Flow Boiling of HFE7000.* Lausanne, Switzerland, s.n.

Melcher, J., 1976. Electric Fields and forces in semi-insulating liquids. *Journal of Electrostatics*, Volume 2, pp. 121-132.

Neve, R. & Yan, Y., 1996. Enhancement of Heat Exchanger Performance using combined Electrohydrodynamic and Passive Methods. *Int. J. Heat and Fluid Flow,* Volume 17, pp. 403-409.

Ng, K., 2010. M.Sc Thesis: Mechanisms of electrohydrodynamic two-phase flow structures and the influence on heat transfer and pressure drop.

Ng, K., Ching, C. & Cotton, J., 2011. Transient Two-Phase Flow Patterns by Application of a High Voltage Pulse Width Modulated Signal and the Effect on Condensation Heat Transfer. *ASME Journal of Heat Transfer,* Volume 133, pp. 091501-1 to 091501-10.

Norris, C. et al., 1999. Electrohydrodynamic effects on Flow Redistribution and Convective Boiling in Horizontal Concentric Tubes. *ASHRAE Trans.,* 105(1), pp. 222-236.

Ogata, J. & Yabe, A., 1993. Augmentation of Boiling Heat Transfer by Utilising the EHD effect - EHD Behaviour of Boiling Bubbles and Heat Transfer Characteristics. *Int. Journal of Heat and Mass Transfer,* 36(3), pp. 783-791.

Paschkewitz, J. & Pratt, D., 2000. The infuence of fluid properties on electrohydrodynamic heat transfer enhancement in liquids under viscous and electrically dominated flow conditions. *Experimental Thermal and Fluid Science,* Volume 21, pp. 187-197.

Posew, K., Laohalertdecha, S. & Wongwises, S., 2009. Evaporation heat transfer enhancement of R-134a flowing inside smooth and micro-fin tubes using the electrohydrodynamic technique. *Energy Conversion and Management,* Volume 50, pp. 1851-1861.

Sadek, H., 2009. *PhD Thesis: Electrohydrodynamic control of convective condensation heat transfer and pressure drop in a horizontal annular channel, McMaster University, Hamilton, Ontario.* s.l.:s.n.

Sadek, H., Cotton, J. & Ching, C., 2011. Effect of Alternating High-Voltage Electric Fields on In-Tube Convective Condensation. *Journal of Enhanced Heat Transfer,* Volume 18, pp. 137-147.

Salehi, M., Ohadi, M. & Dessiatoun, S., 1996. The Applicability of the EHD Technique for Convective Boiling of Refrigerant Blends--Experiments with R-404A. *ASHRAE Trans.,* 102(1), pp. 839-844.

Salehi, M., Ohadi, M. & Dessiatoun, S., 1997. EHD Enhanced Convective Boiling of R134a in Grooved Channels - Application to Subcompact Heat Exchangers. *Journal of Heat Transfer,* Volume 119, pp. 805-809.

Singh, A., Ohadi, M., Dessiatoun, S. & Chu, W., 1994. In-Tube Boiling Heat Transfer Enhancement or R123 Using the EHD Technique. *ASHRAE Trans.,* 100(2), pp. 818-825.

Singh, A. et al., 1995. In-Tube Boiling Enhancement of R134a Utilizing the Electric Field Effect. *ASME-JSME Papers,* Volume 2, pp. 215-223.

Souza, A., Chato, J., Wattelet, J. & Christoffersen, B., 1993. Pressure Drop During Two-Phase Flow of Pure Refrigerants and Refrigerant-Oil Mixtures in Horizontal Smooth Tubes. *ASME Heat Transfer Div. ,* Volume HTD-243, pp. 35-41.

Stratton, J., 1941. *Electromagnetic Theory.* New York: McGraw-Hill .

Swenson, H., Carver, J. & Szoeke, G., 1962. The Effects of Nucleate Boiling Versus Film Boiling on Heat Transfer in Power Boiling Tubes. *Journal of Engineering Power,* Volume 84, pp. 365-371.

Taitel, Y. & Dukler, A., 1976. A model for predicting flow regime transitions in horizontal and near horizontal gas-liquid flow. *AIChE Journal,* 22(1), pp. 47-55.

Turnbull, R., 1968. Electroconvective Instability With a Stabilizing Temperature Gradient. I. Theory, II. Experimental Results. *The Physics of Fluids,* Volume 11, pp. 2588-2603.

Van, P., 2004. *Wolverine Engineering Data Book III.* [Online]
Available at: http://www.wlv.com/products/databook/db3/DataBookIII.pdf
[Accessed 10 12 2011].

Withers, J. & Habdas, E., 1974. Heat Transfer Characteristics of Helical Corrugated Tubes for Intube Boiling of refrigerant R12. *AIChE Symposium Series,* 70(138), pp. 98-106.

Yabe, A. et al., 1992. *Experimental study of electrohydrodynamically (EHD) enhanced evaporator for nonazeotropic mixtures.* Anaheim, CA, s.n., pp. 455-460.

Yilmaz, S., Hwalck, J. & Westwater, J., 1980. Pool Boiling Heat Transfer Performance for Commercial Enhanced Tube Surfaces. *ASME,* Volume 80-HT-41.